TransformAr

Accelerating and upscaling transformational adaptation in Europe: demonstration of water-related innovation packages

D2.2 Modelling customization and implementation report

- Bio-physical modelling implementation -

This project has received funding from the European Union's Horizon H2020 innovation action programme under grant agreement 101036683.

Author(s)	Fred F. Hattermann, Jisha Joseph, Andrea Rivosecchi, Stelios Karozis et al.
Primary Contact and Email	hattermann@pik-potsdam.de
Date	30.09.2024 (submission)
Status	Final after with minor review comments addressed
Deadline	September 30
Reviewed by	Antonio Trabucco
Suggested citation	Fred F. Hattermann, Jisha Joseph, Andrea Rivosecchi, Stelios Kazonis et al. (2014) Modelling customization and implementation report of the EU H2020 TransformAr project

TABLE OF CONTENTS

ABBREVIATIONS

Abbreviations	Description
CMIP	Coupled Model Intercomparison Project
GCM	General Circulation Model
IPCC	Intergovernmental Panel on Climate Change
ISIMIP	Inter-Sectoral Impact Model Intercomparison Project
RCP	Representative Concentration Pathway
SSP	Shared Socioeconomic Pathways
WP	Work Package
NBS	Nature Based Solutions
EU	European Union
EEA	European Environment Agency
E-OBS	European Gridded Observation Dataset
GRACE-FO	Gravity Recovery and Climate Experiment - Follow-On
UN	United Nations
ESD	Empirical Statistical Downscaling
SWIM	Soil and Water Integrated Model
GIS	Geographic Information System
WBGT	Wet Bulb Globe Temperature
NCSRD	National Center for Scientific Research Demokritos
WRF	Weather Research and Forecasting
GRDC	Global Runoff Data Centre
MODIS	Moderate Resolution Imaging Spectroradiometer
LAI	Leaf Area Index
GEV	Generalized Extreme Value
DEM	Digital Elevation Model
SPI	Standardized Precipitation Index
SPEI	Standardized Precipitation-Evapotranspiration Index
FWI	Fire Weather Index
CORDEX	COordinated Regional climate Downscaling EXperiment

Participant acronym	Description
UA	University of Antwerp
CMCC	Euro-Mediterranean Center on Climate Change
ACTERRA	Acterra
E3M	E3-Modelling
PIK	Potsdam Institute for Climate Impact Research
VERHAERT	Verhaert
FEUGA	Fundación Empresa-Universidad Gallega
NCSRD	National Center for Scientific Research “Demokritos”
CZU	Czech University of Life Sciences Prague
LUT	LUT University
NTNU	Norwegian University of Science and Technology
UVIGO	University of Vigo
EPSILON	EPSILON
ADEME	ADEME Guadeloupe
WRT	Westcountry Rivers Trust
MEDSEA	Mediterranean Sea and Coast Foundation
CETMAR	Fundación CETMAR: Centro Tecnológico del Mar
LAPP	Lappeenranta Municipality
MOE	Egaleo Municipality
WE	Water Europe
EQY	Euroquality
MOG	Municipality of Gjøvik

1 Executive summary

The objectives of this deliverable are a) to provide information on climate change and climate change impacts on bio-physical indicators streamlined to demonstrators of TransformAr and b) to upscale impacts and possible adaptation measures to the EU scale with high-resolution. Because of the demonstrators had a demand for climate scenario and climate impact information from the start, PIK and CMCC with the help of other partners created and consolidated fast-track data using their capacities and resources (see also Deliverable 2.1 “Consolidated data framework”). After finalizing the bio-physical modelling implementation, the results were consequently streamlined to the demand of the project and demonstrator partners and presented and discussed in the respective workshops. The data were also used to support the economical and climate risk analysis in Deliverables 2.4 and 2.6.

In addition, to understand the nature, underlying assumptions and amount of data available for the partners, PIK volunteered to compile a web portal to visualize and describe the data and methods in maps and graphs and to make the available data downloadable in common formats.

Summarizing, the results illustrate that climate change is ongoing and the impacts on water resources and on vegetation are already visible and will increase with further global warming. Extremes show the same pattern of stronger trends with higher temperature. This is so relevant, because critical infrastructure is normally adjusted to protect against events of a certain intensity (or return level), and precautionary measures are challenged by the increasing hazards.

However, the results also illustrate what we gain if we invest consequently into avoiding greenhouse gases: significantly lower consequences for natural resources and the extremes, and as a result, the environment and the people living in specific regions of Europe will benefit accordingly.

2 Introduction

2.1 The EU project TransformAR and the role of modelling customization and implementation

Climate change impacts are here and now. The impacts on people, prosperity and planet are already pervasive but unevenly distributed. To reduce climate-related risks, transformational adaptation is essential. TranformAr is an EU-funded project that aims to develop and demonstrate products and services to launch and accelerate large-scale and disruptive adaptive process for transformational adaptation in vulnerable regions and communities across Europe.

Region-specific portfolios including Nature-Based Solutions (NBS), innovative technologies, financing, insurance and governance models, awareness and behavioral change are co-developed and demonstrated. However, in order to adapt successfully, it is necessary to assess and understand the possible consequences of climate change under different scenario conditions. These must be quantified and prepared in such a way that they are transparent and easy to understand for those affected. This applies not only to the people in the demonstrators, but also to regional and national decision-makers. For this reason, it is important to work on different scales: on the one hand on the local to regional level as input for the demonstrators, but the results must also be scaled up for national decision-makers. This deliverable describes how modelling customization and implementation supports the process.

2.2 Research aims and questions of this deliverable

1. To provide information on climate change and climate change impacts on bio-physical indicators streamlined to demonstrators of TransformAr
2. To upscale impacts and possible adaptation measures to the EU scale with high-resolution

2.3 Target audiences

The target audience are experts, decision makers and actors in general interested in or responsible for implementation of climate change adaptations measures to counteract natural disasters, from local demonstrator level to national and EU scale.

2.4 Updated and precised objectives of the deliverable

In the course of the project, it turned out that the demonstrators had a demand for climate scenario and climate impact information from the start, while the deliverable D2.2 is due in month 36. To provide the necessary information at the beginning of the project, partners PIK and CMCC with the help of other partners created and consolidated fast-track data into deliverable 2.1 (Consolidated data framework) using their capacities and resources, for example collected and processed results of ongoing projects such as ISIMIP (The Inter-Sectoral Impact Model Intercomparison Project[1]), which is coordinated at PIK. Additional data were afterwards streamlined to the demand of the demonstrator project partners and presented and discussed in the respective workshops.

Also, it became obvious that the partners and end users had problems to understand the nature, underlying assumptions and amount of data available for them, although support was granted by PIK, CMCC and other involved partners. The data availability and description were also a demand from the

[1] https://www.isimip.org/

midterm review. Therefore, PIK volunteered to compile a web portal to visualize and describe the data and methods in maps and graphs and make the available data downloadable in common formats.

The updated objectives of Deliverable 2.2 are therefore:

1) To provide climate and climate change impacts on bio-physical quantities streamlined to demonstrators throughout the project from its early phases (see also D2.1)
2) To support demonstrators in their workshops and products with information and presentations on climate change risks and related impacts in their region
3) To upscale impacts and to support design of possible adaptation measures to the EU scale with high resolution
4) To visualize and make available the data and information via an easy to use web portal

2.5 Approach

The work in WP2 was done in close coordination with the demonstrators and, in particular, WP3 with the lead partner ACTERRA. Long before the first kick-off workshops took place in the individual demonstrators, climate impact assessments were carried out in WP2, visualized, summarized in presentations and sent to the partners in WP3 and the demonstrators. They were checked in particular for their comprehensibility and transparency. In addition, key messages from the results were formulated, which were important to stimulate the subsequent discussions on possible climate impacts and plausible adaptation options to cope with them. Colleagues from WP2 took part in each of the related demonstrator workshops, presented the results and were active in the follow-up discussions. The data and information were taken from different sources and amended by additional modelling and assessments, where necessary and possible. The specific presentations are available at the TransformAr data and information hub.

The work in phase 1 described above is outlined in Chapter 4 (“Results part 1: fast-track information on climate change and impacts streamlined to the demonstrators”). It is connected to the work done in D2.1 and ensured fast track data availability streamlined to demonstrators, upon their climate and impact data demand evolving throughout the project development.

In order to map the climate impacts at the national scale and for Europe, the necessary climate scenario data was bias-adjusted and regionalized where necessary and formatted for impact modelling. An ecohydrological model for Europe, but with high spatial resolution, was implemented and calibrated for all larger river basins. Climate change impacts on water availability and hydroclimatic extremes were simulated and evaluated. These results were then made available for work in the demonstrators and also prepared for presentation in a web portal. This was supplemented by further demonstrator-specific modelling and evaluations, which were afterwards presented and discussed in various demonstrator workshops.

The related work is outlined in Chapter 5 (“Results part 2: development of advanced climate scenario data and bio-physical modelling implementation”).

Results of WP2 were also made available to other WPs, where needed, for example for economic assessments in WPs 2&4, and shown in inter-project workshops and webinars, for example three time

in the ARSINOE webinar series[2] with different topics from impacts to adaptation and webinars of the MERLIN project focusing on insurance[3].

Finally, a web portal was created in WP2 to visualize the available data and climate change impacts on different sectors, where also data download is possible. This is described in Chapter 6 ("Web portal for data and information").

[2] https://arsinoe-project.eu/news-events/

[3] https://project-merlin.eu/files/merlin/downloads/sectoral_briefings/MERLIN_Sectoral_Briefing_Insurance.pdf

3 CLIMATE CHANGE IN EUROPE

3.1 Observed climate change

The global mean surface temperature between 2013 and 2022 was 1.13 to 1.17 °C warmer than the pre-industrial level, making it the warmest decade on record. Land temperatures in Europe rose even faster in the same period, by 2.04 to 2.10 °C, as the continents warmed faster than the oceans (Figure 1). The year 2023 was the record year with a global temperature rise of almost 1.5 °C compared to per-industrial levels.

Climate change is ongoing and increases the risk of being affected by natural disasters such as storms, floods, droughts, heatwaves and forest fires. Even if the basic infrastructure is adapted to the new extremes, this will still take years and decades and may lag behind the extremes that then prevail. As a result, dealing with the consequences requires careful and science informed planning and priorization of measures.

The European Environment Agency (EEA) has summarised the expected effects on Europe (EEA 2017). According to the report, climate change will primarily manifest itself in changes to the water cycle and related sectors. One of the main problems is the increase in the number and intensity of hydrometeorological extremes such as heatwaves, storms, floods and droughts. Some of the effects are already recognisable: while observations show that annual precipitation amounts have generally increased in Western and Northern Europe, many regions in Central and Southern Europe are experiencing decreasing annual totals (Figure 1).

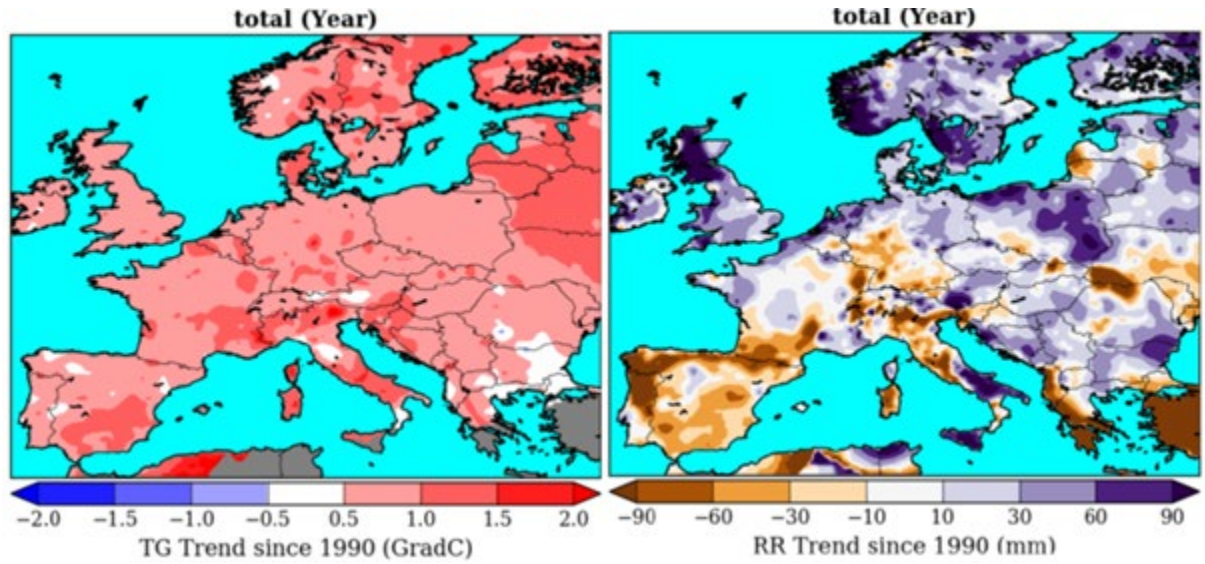

Figure 1: Maps of the cumulative deviations from 1961 to 2018 in relation to 1961 to 1990 of (a) annual mean temperature and (b) annual precipitation (European Gridded Observation Dataset (E-OBS), data processed at PIK).

Central and southern Europe experienced its fifth consecutive summer of drought in 2022. It is the provisional end point of a longer development that began in the 1990s, with a trend towards increased soil dryness, especially towards the end of the summer. While the spring of 2023 was also dry, very heavy rainfall then set in, so that November in Germany, for example, was the second wettest since records began.

Another trend is that the plant growth period is now starting earlier in the year and with it the water requirements of the vegetation. Various studies have shown that the earlier start of the vegetation phase and thus the earlier uptake of water and emptying of the soil by the plants can intensify dry phases and droughts in summer (Lian et al. 2010, Bastos et al. 2020a,b).

In addition, recent data shows that weather patterns are becoming more stable (Hoffmann et al. 2021) and weather patterns are lasting longer. In spring and summer 2018, for example, three prolonged and recurring large-scale meteorological weather patterns were observed, with constant high-pressure weather conditions over northern Europe lasting for several weeks, resulting in summer heatwaves and droughts in central and northern Europe, while the Mediterranean was hit by several catastrophic flood events. Similar weather conditions also occurred in the following years and were particularly severe again in 2022.

The reason for the longer weather persistence are blocking weather conditions, such as the above-mentioned persistent high over northern Europe in June 2018, which remained in place over north-eastern Europe (Scandinavia and northern Russia) until July. In parts of Central and Northern Europe, the seasonal precipitation levels in spring, summer and autumn were below 80 % of the normal level. In southern Europe, instead, there were several heavy rainfall events throughout the year, which caused devastating floods.

Recent work suggests that the occurrence of favourable conditions for blocking weather patterns and the associated extreme weather is increasing, which may be related to increased warming of the Arctic (Scientific American 2019[4]).

On the other hand, a shift of precipitation from summer to winter, which has also been observed, could lead to higher groundwater recharge in the winter months.

[4] https://michaelmann.net/sites/default/files/articles/MannSciAmFeb19.pdf

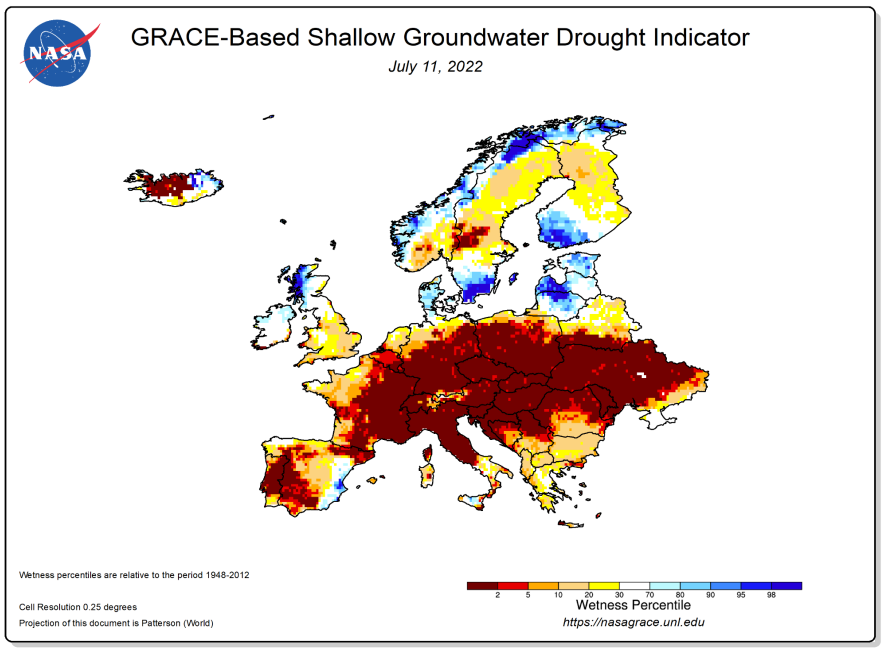

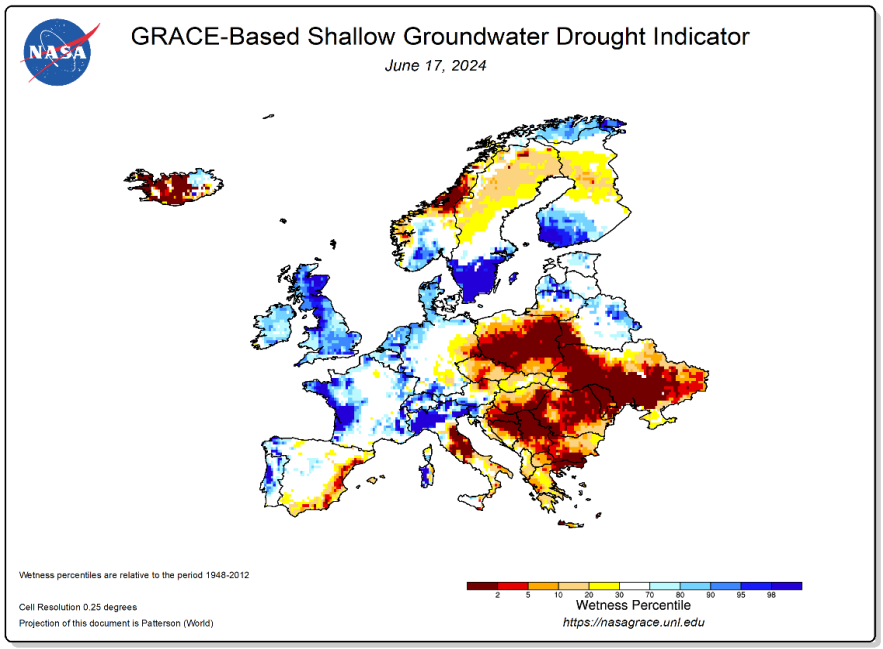

Figure 2: Water content anomaly in the upper aquifer expressed as a percentile indicating the probability of occurrence for dry and wet conditions and the respective location and season, top for July 2022 and bottom for February 2024 (source: Nasa-Grace satellite data[5]).

Every week, scientists at NASA's Goddard Space Flight Centre produce indicators of groundwater and soil moisture during drought. They are based on observations of terrestrial water storage derived from

[5] https://nasagrace.unl.edu/, retrieved on 24/07/2022 and 24/06/2024

GRACE-FO satellite data and integrated with other observations using a sophisticated numerical model of water and energy processes at the land surface. The drought indicators describe the current wet or dry conditions, expressed as a percentile indicating the probability of occurrence for the particular location and time of year, with lower values (reddish colours) meaning drier than normal and higher values (blue colours) meaning wetter than normal (Figure 2). A clear deficit can be seen in the summer of 2022 in particular, while this has been balanced out by the winter of 2024, at least in the northern part of Europe, by the abundant autumn precipitation.

The same hydroclimatic trends that initially lead to a decline in soil moisture also have a subsequent effect on groundwater recharge and thus, in the long term, on groundwater reservoirs. However, groundwater is the most important source of drinking water in Europe, as around 75 % of EU inhabitants depend on groundwater for their water supply. In most parts of Europe, groundwater recharge mainly takes place in winter, as the water demand of vegetation is low during this period. Due to climate change, the growing season lasts longer each year and the winter period without vegetation cover is shrinking (Lian et al. 2020). As a result, groundwater recharge is decreasing in regions where this trend is not offset by a sharp increase in (winter) precipitation. Additional overexploitation of groundwater resources, for example in parts of southern Europe, has led to a sharp decline in groundwater levels and water conflicts (Custodio et al. 2021).

3.2 Projections into the future

While Figure 2 shows the observed effects of climate change in Europe for the groundwater body, the strength and regional characteristics of future climate impacts depend heavily on the extent of further global temperature increases. The sixth Assessment Report (AR6) of the Intergovernmental Panel on Climate Change (IPCC) uses the term "Shared Socioeconomic Pathways" (SSPs) to describe scenarios for the course of future climate change (IPCC 2021).

A distinction is made between different scenarios, ranging from SSP1-2.6 to SSP5-8.5 according to the assumed range of radiative forcing in 2100 (e.g. 2.6 W/m2) and socioeconomic storyline. SSP1-2.6 corresponds to a scenario with significant investment in climate protection, which also includes efforts in the area of negative emissions. SSP5-8.5 corresponds to a "high emissions" scenario, while other SSPs are defined as medium scenarios depending on the extent to which emissions are avoided (for more information about the storylines, see Chapter 2.3). Current emissions tend to follow the latter extreme scenario (Schwalm et al. 2020). The numerical values of the scenarios are therefore not the values of the expected temperature rise, rather a temperature rise is the result of the radiative forcing expressed by the values due to increased greenhouse gas concentrations (cumulative total amount up to the year 2100 or the resulting radiative forcing).

The corresponding climate simulations for the sixth UN Assessment Report, on which the statements on future climate change in the AR6 are largely based, were largely carried out in the Coupled Model Intercomparison Project Phase 6 (CMIP6), an international collaboration of the climate modelling community. The projected trends are shown in Figure 3 as an average over the CMIP6 ensemble, which also illustrates how strongly different scenarios work (SSP1-2.6 versus SSP5-8.5).

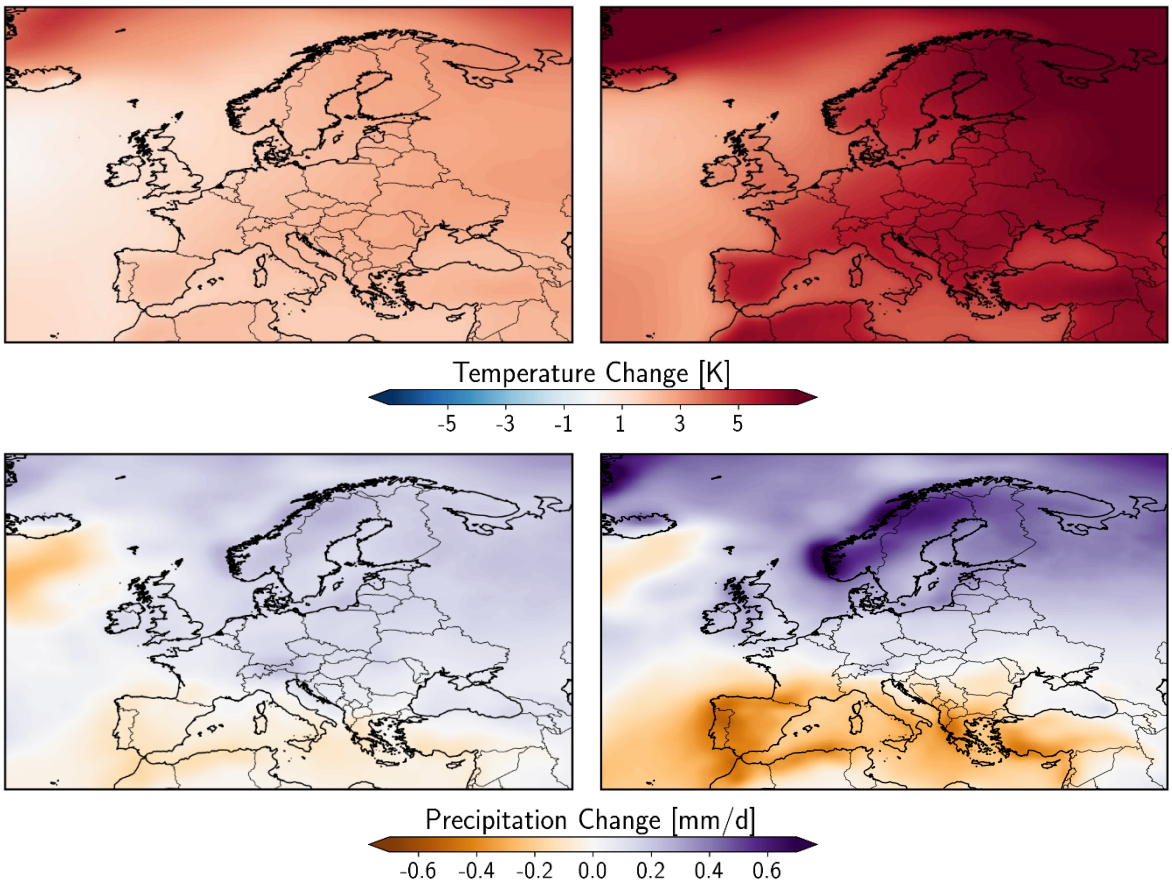

Figure 3: Changes in temperature (top) and precipitation (bottom) by the end of the century (2071-2100 compared to 1971-2000) for SSP1-2.6(left) and SSP5-8.5 (right (34 global model simulations CMIP6 climate data, processed at PIK)).

According to IPCC (2021), projections from the CMIP6 initiative suggest that temperatures across European land areas will continue to increase throughout this century at a higher rate than the global average. Land temperatures in Europe are projected to increase further by 1.2 to 3.4° under the SSP1-2.6 scenario and by 4.1 to 8.5°C under the SSP5-8.5 scenario (by 2071-2100, compared to 1981-2010). The highest level of warming is projected across north-eastern Europe, northern Scandinavia and inland areas of Mediterranean countries. The lowest warming is expected in western Europe, especially in the United Kingdom, Ireland, western France, Benelux countries and Denmark.

More uncertain are the trends in precipitation, but it is projected to increase in larger parts of western and northern Europe, while decreasing in southern and eastern Europe. However, comparison with observations reveals that in some regions of Europe, observed trends and trends in the historical period of GCMs simulations (1951-2020) do not agree.

3.3 Climate scenario storylines: Narratives of a possible Future

A new set of climate scenarios has been developed for the sixth IPCC report (IPCC AR6). They are referred to as the "Shared Socio-economic Pathways" (SSPs) and represent narratives for different socio-economic scenarios. Each pathway results in a different increase of atmospheric greenhouse gas concentrations and therefore leads to a different level of global warming.

Five basic SSP scenarios were defined:

SSP1: The sustainable and "green" pathway describes an increasingly sustainable world. Global commons are being preserved as the limits of nature are being respected. The focus is more on human well-being than on economic growth. Income inequalities between states and within states are being reduced. Consumption is oriented towards minimizing material resource and energy usage.

SSP2: The "Middle of the road" or medium pathway extrapolates the past and current global development into the future. Income trends in different countries are diverging significantly. There is a certain cooperation between states, but it is barely expanded. Global population growth is moderate and levelling off in the second half of the century. Environmental systems are facing a certain degradation.

SSP3: Regional rivalry. A revival of nationalism and regional conflicts pushes global issues into the background. Policies increasingly focus on questions of national and regional security. Investments in education and technological development are decreasing. Inequality is rising. Some regions suffer drastic environmental damage.

SSP4: Inequality. The chasm between globally cooperating developed societies and those stalling at a lower developmental stage with low income and a low level of education is widening. Environmental policies are successful in tackling local problems in some regions, but not in others.

SSP5: Fossil-fuelled Development. Global markets are increasingly integrated, leading to innovations and technological progress. The social and economic development, however, is based on an intensified exploitation of fossil fuel resources with a high percentage of coal and an energy-intensive lifestyle worldwide. The world economy is growing and local environmental problems such as air pollution are being tackled successfully.

Figure 4 presents the 5 pathways in a scenario space defined by two axes: 1) challenges for adaptation, and 2) challenges for mitigation. In general, global warming increases from SSP1 to SSP5.

Figure 4: The SSPs of the IPCC guided scenario set (O'Neill et al., 2016)

The SSPs presented above roughly collide with the RCP (Representative Concentration Pathways) scenarios RCP2.6, RCP4.5, RCP6.0 and RCP8.5 of the previous IPPC report (AR5). It allows for a direct

comparison between CMIP5 and CMIP6 simulations. Compared to the RCP scenarios, the new SSP-based scenarios provide economic and social reasons for the assumed emission pathways and changes in land use.

In the current study, the scenarios SSP1-2.6, SSP3-7.0 and SSP5-8.5 of CMIP6 have been used. They represent a low, medium, and severe climate change scenario.

4 Methodology and data applied in TransformAr

4.1 From global climate model output to regional biophysical impacts

Models help us to work through complicated problems and understand complex systems (NOAA, 2023), like the global climate system or the hydrological cycle of a river basin. A chain of models from global climate models to regional climate models to (eco-)hydrological catchment models is applied in TransformAr to determine the impacts of global climate change on regional water resources, vegetation and hydrological extremes (Figure 5). The first model layer concerns the Global Climate Model (GCM). It is a complex mathematical representation of the major climate system components (atmosphere, land surface, ocean, and sea ice) that divides the global atmosphere into a three-dimensional gridded space. The GCM simulates the fluxes of heat, water, and momentum of the global climate at a fairly course spatial resolution. GCMs are used to model the implications of several greenhouse gas emission scenarios at global scale. In our case, we apply models of the Coupled Model Intercomparison Project Phase 6 (CMIP6).

Figure 5: Chain of models for simulating climate impacts on the water cycle.

GCM results generally are too coarse to serve directly as input for a regional impact assessment. This is so because landscapes are typically diverse and can range from steep mountains to flat coastal plains. Each landscape type impacts differently on the respective climate parameters, such as rainfall, temperature, evaporation, floods, droughts, and other extreme events. Hence, a regionalisation or downscaling of the global climate data is necessary.

The downscaling task is achieved by a combination of Regional Climate Models (RCM) and Empirical Statistical Downscaling (ESD). It is applied over a limited area and driven by GCM data. RCMs apply basically the same methodology as the GCMs, but at a finer spatial resolution. The resulting regional climate data tend to be biased and must be corrected before use by an eco-hydrological impact model.

This step is called bias correction or bias adjustment. The resulting bias-controlled meteorological data sets—which include precipitation, temperature, radiation, humidity, and wind speed— are used to drive hydrological model systems of varying complexity. The data used at the European scale are bias-adjusted applying the methodology described in Lange et al. 2019. In the case of the Greek demonstrator, data from a specific dynamic regional climate model was used in order to be able to map temperature and precipitation extremes at a very high resolution.

The main impact model applied in TransformAr is the eco-hydrological model SWIM (Soil and Water Integrated Model, Hattermann et al. 2011, Krysnaova et al. 2015), which integrates the relevant water and vegetation processes and management of water and land in one model framework.

In order to obtain a better statistical basis for the investigation of the development of flood extremes in Europe, a weather generator was applied to generate long weather patterns with many extreme events for the historical period and the future. These were transformed into runoff components by SWIM and into flood waves by the hydrodynamic model CamaFlood (Chapter 3.4.2).

In order to provide climate change and related impact data from the start of the project, additional data and information was collected from other projects and initiatives, where the projects partners are engaged in, as well as from literature.

4.2 The climate data applied in TransformAr

The basis for the evaluation of the current climate in Europe, to calibrate the eco-hydrological model and bias-adjust the climate data is the observation-corrected re-analysis climate dataset W5E5 version 2.0 (WFDE5 over land merged with ERA5 over the ocean, Lange et al. 2021). W5E5 version 2.0 is available for the time period 1979-2019 for the entire globe with a 0.5° spatial resolution (approximately 50km x 50km at the equator) and with a daily time step. The W5E5 dataset was compiled within the international Inter-Sectoral Impact Model Inter-comparison Project (ISIMIP3b) to support the bias adjustment of climate input data for diverse impact assessments. The W5E5 data include all necessary climate inputs to drive the eco-hydrological model, namely precipitation, radiation, mean temperature, maximum temperature, minimum temperature, and wind speed.

Regional dynamic climate modelling (RCM) and empirical statistical downscaling (ESD) applied to a limited area and driven by GCM data can provide information at much smaller scales to support more detailed impact assessment and adaptation planning, which is critical in many vulnerable regions of the world. The Coordinated Regional Climate Downscaling Experiment (CORDEX) serves to achieve this goal by coordinating the production of consistent sets of regionalised projections worldwide and by analysing and advancing the quality of regional climate models through a series of experiments to produce regional climate projections. However, due to the vast computation time for regional climate modelling, CORDEX RCM results are currently not available for CMIP6. This is why they were replaced by ESD results of the project ISIMIP, which is coordinated at PIK, using the methodology described in Lange et al. 2019. The results are referred to as the ISIMIP3b scenarios.

However, since regional climate models are better at depicting short-term or more local extremes, results from regional climate models were used for modeling of weather events with the weather generator and for urban conditions in the Athens metropolitan area.

4.3 The eco-hydrological model SWIM

The SWIM (Soil and Water Integrated Model) eco-hydrological model was developed to investigate the impacts of climate and land-use change at regional level. The regional scale is where climate impacts manifest and where most adaptation and mitigation measures are implemented. Further, the regional scale represents the main landscape features that shape and accentuate the impacts of climate change (Figure 6) (Krysanova et al 2015, Hattermann et al 2005 and 2011).

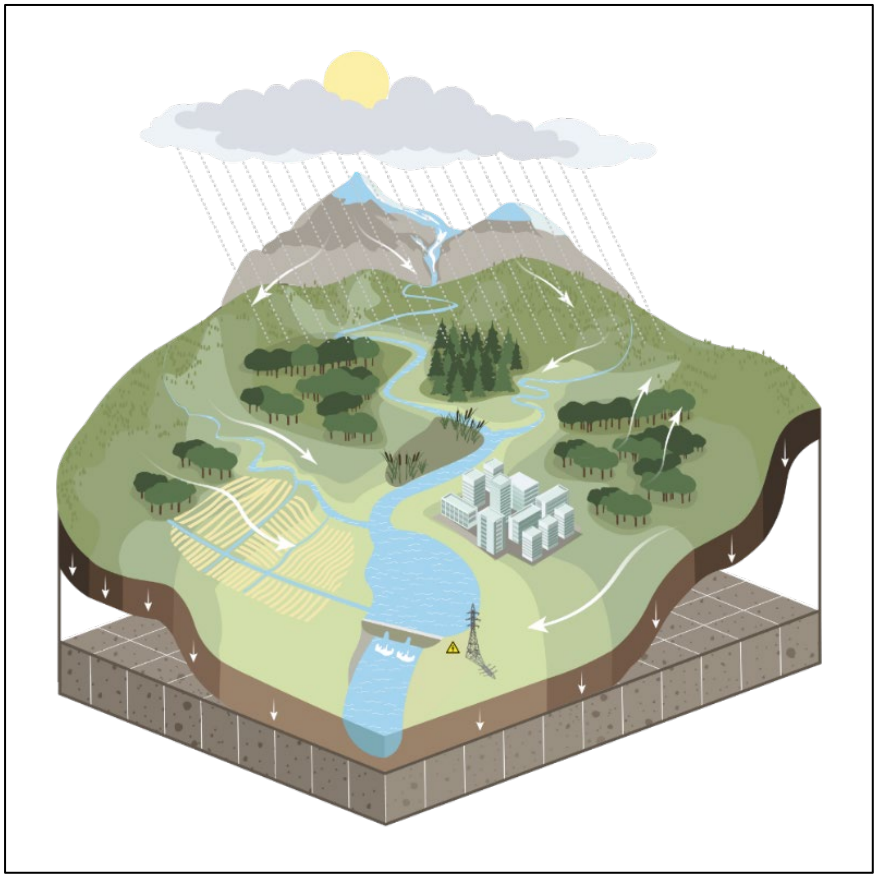

Figure 6: The eco-hydrological model SWIM integrates the main landscape features that shape and accentuate the impacts of climate change on water and vegetation.

SWIM integrates all the relevant and interconnected hydrological, vegetation and management processes at the regional scale. This comprises runoff generation, plant growth, nutrient and carbon cycling, erosion, and other related processes. The model also considers water management practices and agricultural cropping patterns and yields. Hence, SWIM simulates all interrelated eco-hydrological processes in a single model framework with daily time steps using regionally available data (climate, land use, and soil) while considering feedback between the respective modules (Figure 6). For example, wetlands are considered through flooding and higher water availability for plants, among other things.

The water management module can simulate reservoirs for flood protection, water supply, and low-flow control. Irrigation, hydropower production, and transmission lines are also included. The agricultural module includes the simulation of cropping sequences, fertilisation and harvesting, and the associated nutrient cycles. The vegetation module simulates the dynamic growth of different forest types as well as grassland and shrubland.

SWIM is a spatially semi-distributed model that applies a three-level disaggregation scheme from catchment to sub-catchment to hydrotope. Model setup and post-processing are supported by a GIS interface. Results are presented as time series and as maps for a range of variables.

The SWIM model has been implemented and applied in various projects worldwide to investigate the consequences of climate and land-use change on the water-energy-food nexus and on hydroclimatic extremes (see e.g. in Hattermann et al. 2011, 2014, and for an overview Krysanova et al. 2015). SWIM has also participated in various model intercomparison studies (see e.g. 2017). SWIM is maintained and further developed by the regional hydrological modelling group of PIK's Research Division II[6]. For more information see Chapter 9.1 of the Annex, where also the description of the spatial input data to set-up the model can be found (Table A1).

4.4 Additional tools to model floods at European scale

4.4.1 The weather generator

IMAGE-PIK is as massively multi-site, multivariate daily stochastic weather generator. It builds upon the IMAGE model developed by Sparks et al. (2018) at Imperial College London. IMAGE-PIK simulates multiple correlated variables as latent Gaussian variables using an autoregressive process. The spatial structure is encoded in the parameter matrices of the autoregressive process, which are determined using a principal component analysis (von Storch and Zwiers, 1999). These parameter matrices are estimated using appropriate gridded climate data time series, derived either from observations or climate model simulations. As a result, IMPAGE-PIK can simulate arbitrary long time series with realistic cross-variable correlations and spatio-temporal patterns.

Using the weather generator IMAGE-PIK, we produced synthetic time series based on observations from E-OBS v27.0e and regional climate model projections from IMPACT2C. These synthetic time series preserve the same spatio-temporal and inter-variable correlations as the original datasets, making them suitable for studying statistically rare events, such as extreme precipitation, flooding, or high temperature events. A key innovation of these synthetic time series is their coverage of the entire European continent. For more information see Chapter 10.2 of the Annex.

4.4.2 CaMa-Flood hydrodynamic model

State-of-the-art (eco-)hydrological models such as SWIM are designed to model hydrological processes and the water balance of landscapes and river basins. This mostly concerns water quantities stored in soils and groundwater, plant uptake, evapotranspiration and flow of a water volume via the river network to the basin outlet. It simulates on a daily timestep. For the sub-daily modelling of water levels and flood waves in rivers, they are mostly coupled to a hydrodynamic model. The CaMa-Flood (Catchment-based Macro-scale Floodplain, Yamazaki et al. 2014) model, selected in WP2, is designed to simulate the hydrodynamics in regional to continental-scale rivers.

The entire river network is discretized to the hydrological units named unit-catchments for achieving efficient flow computation at the global scale. The water level and flooded area are diagnosed from the water storage at each unit-catchment using the sub-grid topographic parameters of the river channel and floodplains. By adapting a grid-vector hybrid river network map which corresponds one irregular-shaped unit-catchment to one grid-box, both realistic parameterization of sub-grid

[6] https://www.pik-potsdam.de/en/institute/departments/climate-resilience/models/swim

topography and easy analysis of simulation results are achieved. The river discharge and flow velocity are calculated with the local inertial equation along the river network map which prescribes the upstream-downstream relationship of unit-catchments. The time evolution of the water storage, the only one prognostic variable, is solved by the water balance equation which considers inflow from the upstream cells, outflow to the downstream cell and input from runoff forcing at each unit-catchment. Bifurcation of river channels can be also represented by analyzing high-resolution topography. The detailed description of the CaMa-Flood model is found in the description papers (Yamazaki et al. 2014).

5 Results part 1: Fast-track information on climate change and impacts streamlined to the demonstrators

Starting with the city and region of Lappeenranta and then for all demonstrators, experts from WP2 were invited to participate in the kick-off workshops with local stakeholders from science and authorities to present the results, answer questions and discuss possible adaptation measures.

5.1 Climate change projections at demonstrator scale

In collaboration with the demonstrator leads and WP3 (ACTERRA), the information required on climate change and its consequences was defined right at the start of the project. In several iterations, care was also taken to ensure that the information provided was presented and communicated in a way that was understandable for educated layman. Such a graphic illustrating the change in temperature under different scenario conditions with the range of uncertainty, is shown in Figure 7, and for precipitation in Figure 8 (for the example of the Gjovic demonstrator site).

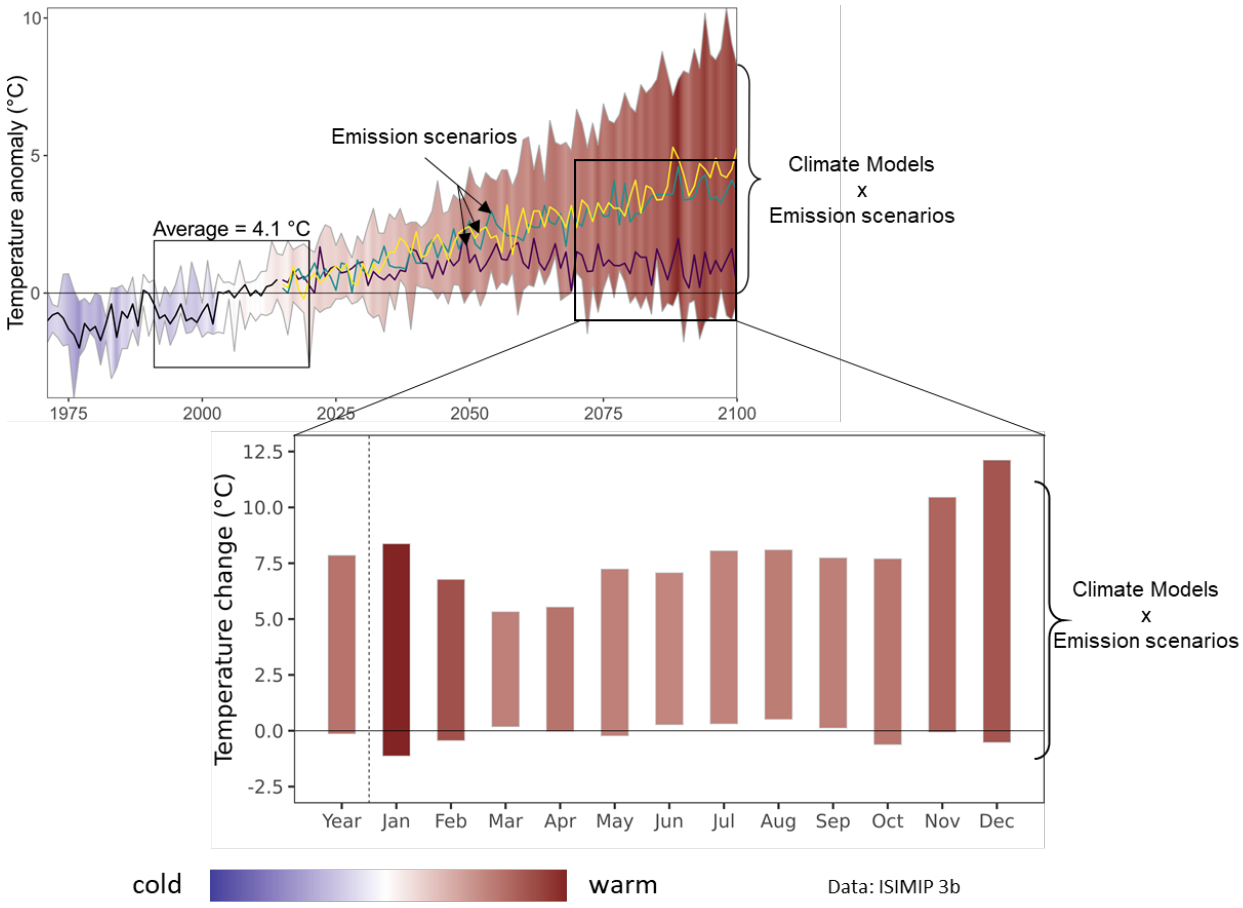

Figure 7: Change in temperature under different scenario conditions for the example of the Gjovic demonstrator site with the range of uncertainty (top: annual development, bottom: seasonal change).

For the City of Gjovic and the surrounding area, the results give as a mean of the different scenarios a temperature increase of + 2.7 °C (Figure 7), but for the high-end scenarios (yellow line) up to +5°C,

with a higher increase in winter temperature and less increase in summer (Figure 7, bottom). Clearly visible is also that uncertainty is higher at the end of the century. As for precipitation (Figure 8), there is an annual mean increase in rainfall and also in the mean of most seasons (on average +35% in January) except in summer (on average -4.3% in August), albeit again with high uncertainty.

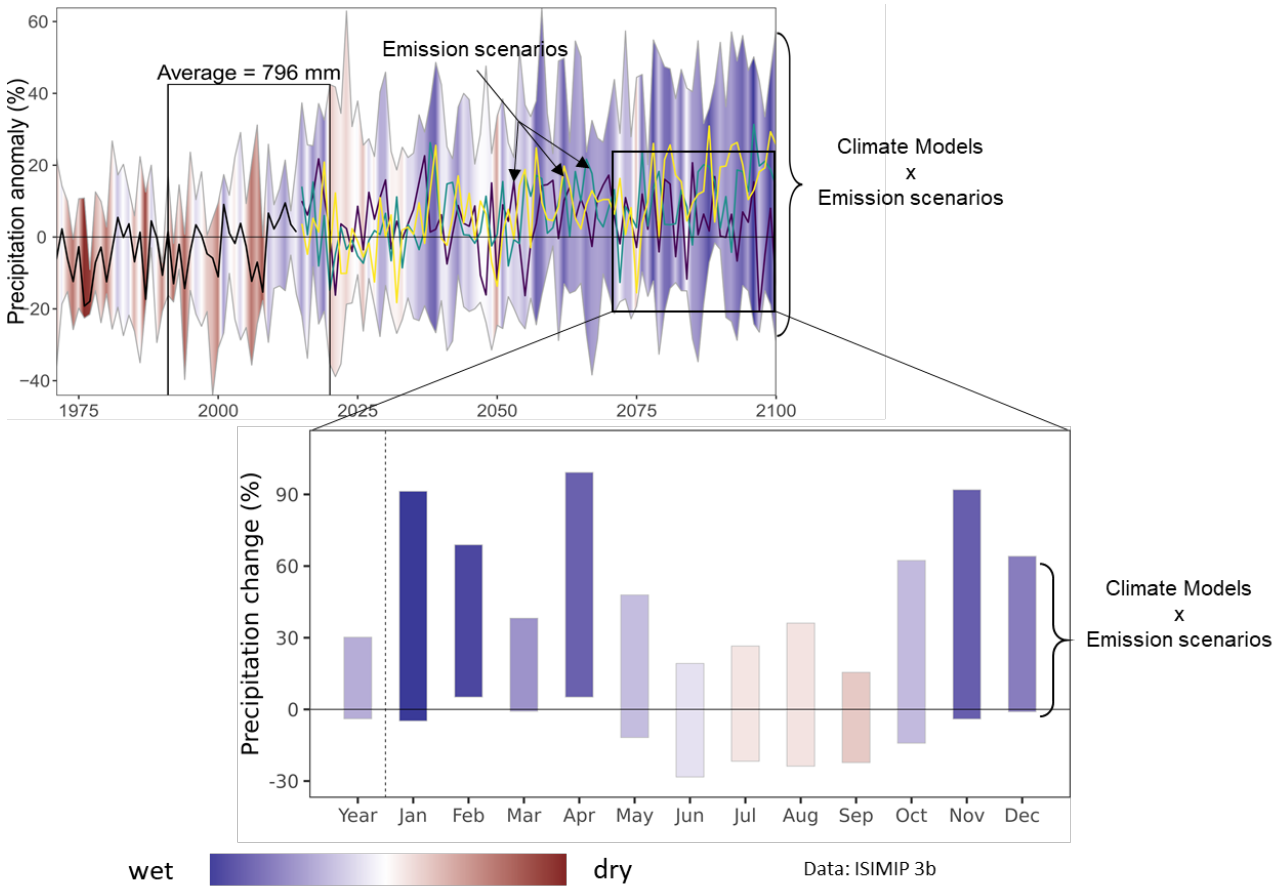

Figure 8: Same as Figure 7, but for precipitation.

Table 1: Selected biophysical indicators for Gjovic demonstrator site (in brackets the range of uncertainty).

	2021-2050	2031-2060	2071-2100
summer days (T_{max} > 25 °C):	+103% (17 – 180%)	+146% (21–300%)	366% (36 –1267%)
frost days (T_{min} < 0 °C)	-12% (-26 – -6%)	-15% (-36 – -4%)	-28% (-70 – 6%)
icing days (T_{max} < 0 °C)	-14% (-29 – -7%)	-19% (-39 – -4%)	-32% (-83 – 8%)
warm spells (at least 6 consecutive days with very high temperatures)	185% (73 – 473%)	231% (116 – 753%)	548% (661 – 1695%)
cold spells (at least 6 consecutive days with very low temperatures)	-62% (-92 – 50%)	-69% (-96 – 0%)	-86% (-100 – -19%)

5.2 Impacts on water and land

Furthermore, the ecohydrological model SWIM was applied to transform the changes in climate shown in Figures 7 and 8 into changes in the water balance and the extremes, for each scenario and climate model run. Such a result, again for the Gjovic demonstrator, is shown in Figure 9, with the change in runoff under different scenario conditions on the left and the change in groundwater recharge on the right. Additional water components were presented, for example snow development, which is relevant in the northern demonstrators, and evapotranspiration.

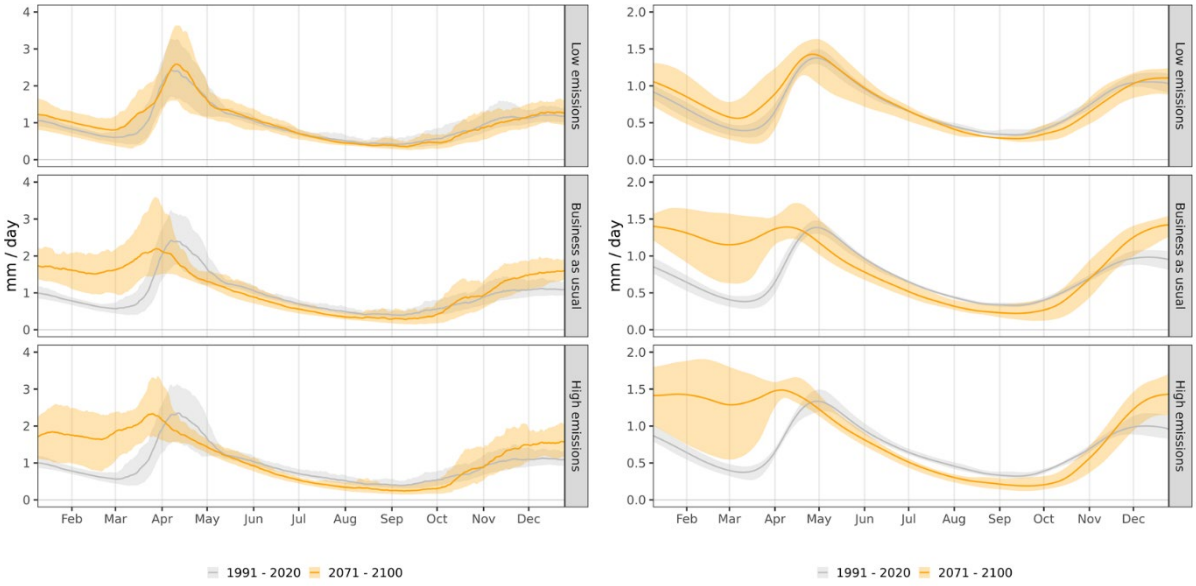

Figure 9: Change in runoff generation (left) and groundwater recharge (right) under different scenario conditions until end of the century, for the example of the Gjovic demonstrator, with the range of uncertainty (top: moderate climate scenario, middle: intermediate climate scenario, bottom: high-end climate scenario).

The results show in the case of Gjovic that, especially under strong global warming, there is a considerable shift in seasonal runoff generation and groundwater recharge, mainly driven by temperature and changes in snow cover and earlier snow melt. In total, there is also more water available, but not relative to the increase in precipitation, because the higher temperatures stimulate evaporation and plant transpiration, the latter because of more heat stress and longer vegetation periods. The decrease in water flows in summer (June to November) points at possibly more summer droughts and water stress.

With climate change, not only average but also intense precipitation increases in most regions of Europe, and also in Norway/ Gjovic. Floods and flash floods are a major concern expressed by the local authorities and experts, and adaptation to counteract, for example unsealing of surfaces and collecting surface runoff, is a measure currently discussed and partly implemented. This is why SWIM was applied to investigate how surface runoff, as an indicator for flash floods, may develop under climate change conditions, and how effective unsealing is. Figure 10 illustrates the impact of climate change on surface runoff, with an increase due to more intense rain events, and the effectiveness of unsealing from a fully sealed surface to medium sealed one to a fully unsealed.

Consequently, more water infiltrates into the soil when unsealed, leading to more soil moisture, groundwater recharge and transpiration by plants, which leads (besides the shading effect of the vegetation) in turn to a cooling of the surface near atmosphere. Additional infiltration into soils, additional groundwater recharge and additional evapotranspiration are typical impacts of unsealing in a so called “sponge city”.

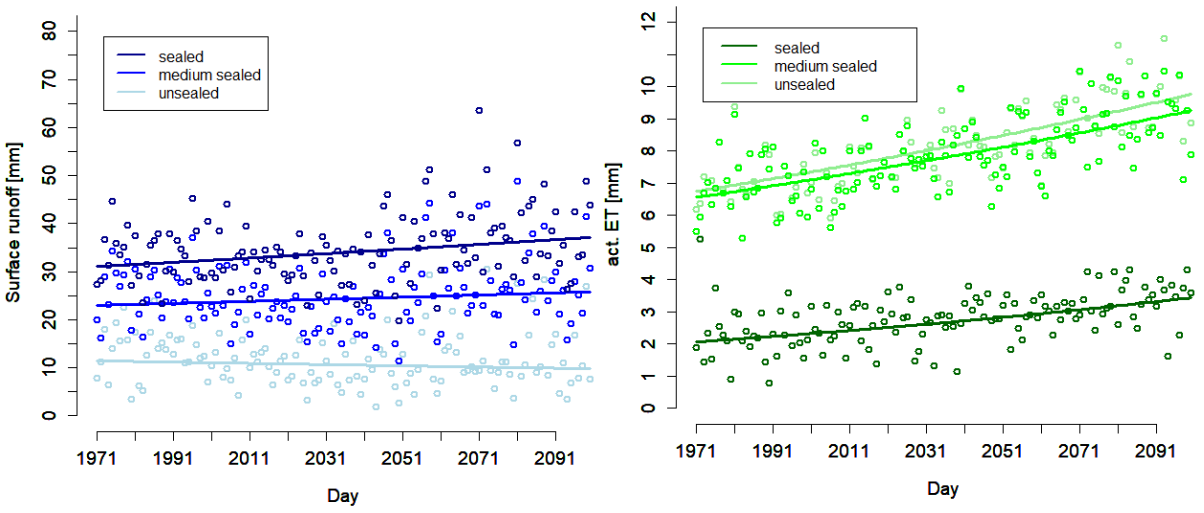

Figure 10: The development of maximal daily surface runoff (left) and maximal daily actual evapotranspiration (right) under climate change conditions, and the effectiveness of unsealing.

In sponge cities, unsealing and additional evapotranspiration may lead to an additional cooling effect of up to 3°C.

5.3 Impacts on health and productivity

Another concern expressed by the actors mainly from the southern demonstrators was the increase in heat stress and related impacts on health and outdoor productivity. In response to this, indicators were sought and defined in WP2 which, on the one hand, quantify how heat and humidity affect the human body and, on the other hand, how much this affects physical performance and productivity when working outdoors.

The indicator chosen for heat impacts on humans is the wet-bulb globe temperature (WBGT), a measure of environmental heat. In addition to a simple temperature measurement, the WBGT accounts for all four major environmental heat factors: air temperature, humidity, radiant heat (from sunlight or sources such as furnaces), and air movement (wind or ventilation). It is widely used and common in the medical sector, and by industrial hygienists, athletes, and the military to determine appropriate exposure levels to high temperatures. Table 2 lists the risk classes of the WBGT, with high to very high risk above values of 25 °C WBGT and extreme risk of thermal injury above 30 °C WBGT. The WBGT was calculated based on the Liljegren et al. (2008) method.

The WBGT was calculated applying the ISIMIP3b climate data for entire Europe and analysed at demonstrator scale. The increase in WBGT until end of this century and for the summer season is given in Figure 11 for the Egaleo region and demonstrator site under high-end scenario conditions (SSP5-

8.5). One of the southern demonstrators has been chosen here to illustrate how strong the increase and risk is, because mean and maximum temperature are much higher there than in the northern demonstrators and so is also the risk for thermal injury. The result is that there is a steep increase in WBGT, leading to high risk of thermal injury when doing outdoor work or exercises.

Table 2: Definition of WBGT risk classes[7].

Category	WBGT (°C)	Risk of thermal injury	Modifying action for vigorous sustained activity
1	≤ 20	Low	Caution over motion
2	21-25	Moderate to high	Increase vigilance. Take more breaks
3	26-29	High to very high	Limit intensity. Limit work to less than 60 minutes
4	30 and above	Extreme	Cancel outdoor activity or postpone

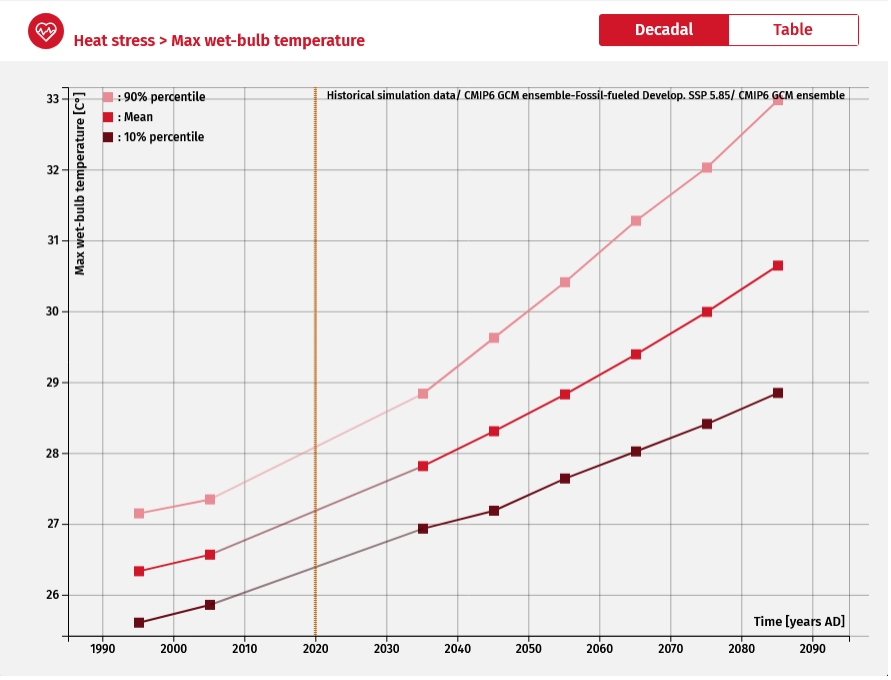

Figure 11: The increase in WBGT until end of this century for the Egaleo region and demonstrator site under high-end scenario conditions (summer season, SSP5-8.5).

There was also concern expressed by the local actors that the higher future temperatures could affect negatively outdoor work and activities, such as in agriculture and in the building sector. As an answer to this demand, the outdoor productivity was calculated based on a regression formula on data from Kjellstrom et al. (2009), which in turn are based on recommendations of the 'The National Institute for Occupational Safety and Health' (NIOSH) and 'International Organization for Standardization' (ISO). Figure 12 explains how a possible increase of the WBGT impacts on working capacity applying levels of job exertion from 200 Watts to 500 Watts. It is visible that above 26 °C WBGT, additional 2 °C WBGT lead to a halving of the working capacity.

[7] https://www.instrumentchoice.com.au/news/everything-you-need-to-know-about-wbgt

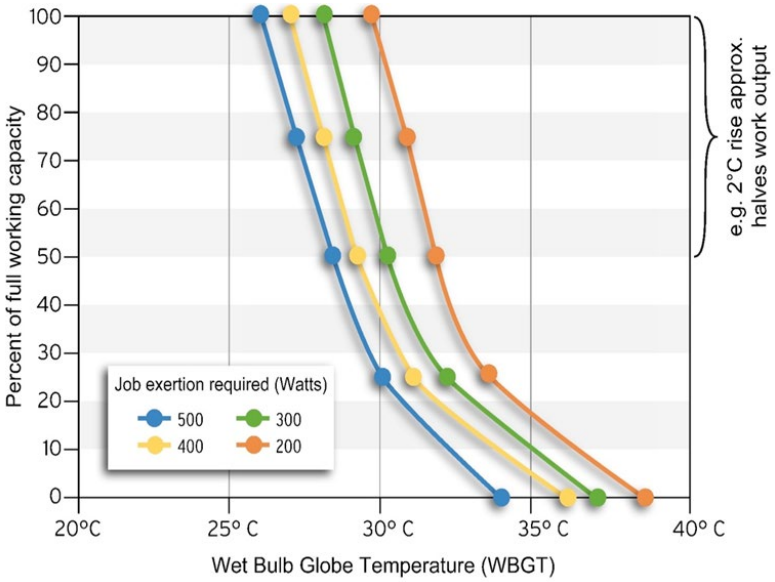

Figure 12: The relationship WBGT to working capacity following Kjellstrom et al. 2009, changed.

Again, for the Egaleo demonstrator site, the relative change in working capacity, as an annual mean and considering the high-end scenario SSP5-8.5, is given in Figure 13. It is visible that under extreme global warming conditions, annual outdoor productivity may decrease by up to 20 %, whereby the decrease is obviously much higher in summer (when most outdoor work is necessary in agriculture and often also in the building sector).

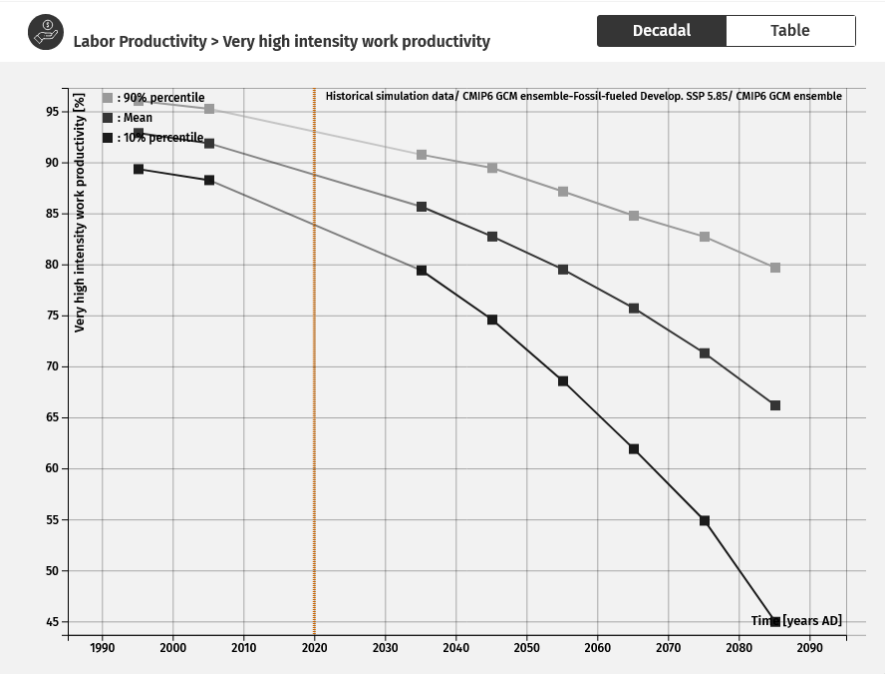

Figure 13: The decrease of outdoor working capacity in summer until end of this century for the EGALO region and demonstrator site under high-end scenario conditions (SSP5-8.5).

6 Results part 2: Advanced climate scenario data and bio-physical modelling implementation

6.1 Climate downscaling

6.1.1 The ISIMIP3b regionalized climate scenario data

The ISIMIP3b ensemble is a model ensemble of global climate models (GCMs) that was developed as part of the third simulation round of the Inter-Sectoral Impact Model Intercomparison Project (ISIMIP, Frieler et al. 2024 and Frieler 2024), which is coordinated at the Potsdam Institute for Climate Impact Research. The global model runs were regionalized to a 50 km x 50 km grid and bias-adjusted using the method described in Lange 2019. The ISIMIP3b ensemble was originally developed for global climate impact research, but is also used for regional studies due to its relatively high resolution (Hattermann et al. 2017, Krysanova et al. 2015). A major advantage of the ensemble is the use of the latest generation of global climate models and SSP greenhouse gas concentration scenarios as part of IPCC AR-6 (IPCC 2021). Table 2 summarizes the simulations of the ISIMIP3b ensemble.

Table 3: The global models of the ISIMIP3b ensemble based on the greenhouse gas concentration pathways (SSP) of the IPCC 6th Assessment Report (IPCC 2021).

GCM	Scenario
CanESM5	SSP1-2.6, SSP3-7.0, SSP5-8.5
CNRM-CM6-1	SSP1-2.6, SSP3-7.0, SSP5-8.5
CNRM-ESM2-1	SSP1-2.6, SSP3-7.0, SSP5-8.5
EC-Earth3	SSP1-2.6, SSP3-7.0, SSP5-8.5
GFDL-ESM4	SSP1-2.6, SSP3-7.0, SSP5-8.5
IPSL-CM6A-LR	SSP1-2.6, SSP3-7.0, SSP5-8.5
MIROC6	SSP1-2.6, SSP3-7.0, SSP5-8.5
MPI-ESM1-2-HR	SSP1-2.6, SSP3-7.0, SSP5-8.5
MRI-ESM2-0	SSP1-2.6, SSP3-7.0, SSP5-8.5
UKESM1-0-LL	SSP1-2.6, SSP3-7.0, SSP5-8.5

6.1.2 High-resolution dataset for Egaleo/ Greece

In case of Greek demonstrator, the Municipality of Egaleo (MOE), a specific high-resolution climate dataset for Greece was utilized (Figure 14), in order to map better the possible climate extremes in and around Athens, where Egaleo is located. The dataset was produced by NCSRD with the dynamic downscaling methodology and it refers to RCP45 and RCP85 climate scenario for three timespans; Historic period (1980-2004), near-future period (2025–2049) and end of century as far-future period (2075–2099). It has a resolution of (5km x 5km) for Greece and it consist of a set of climate variables and post processed indicator:

- Surface Temperature
- Wind Speed

- Relative Humidity
- Precipitation
- Drought: SPI, SPEI
- Wildfire: FWI
- Number of Tropical nights,
- Windchill
- Heatwaves
- Dynamic downscaling

NCSRD employed the Weather Research and Forecasting (WRF) Model, a state-of-the-art atmospheric mesoscale modeling system designed for both meteorological research and numerical weather prediction, to produce the high-resolution dataset.

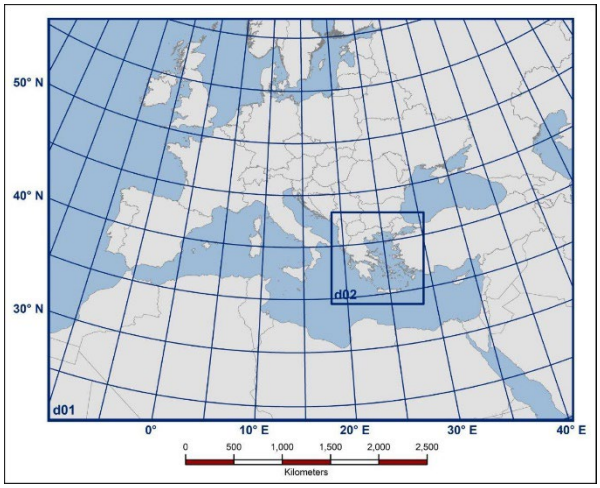

Figure 14: Modelling Domains: d01 refers to the outermost domain and d02 to the nested domain of 5 km (region of Greece).

Greece as a region is influenced by many mesoscale and synoptic weather systems. The latter is essential for the definition of the area of interest and the modeling domain. The domain has to be large enough to cover the large-scale dynamical patterns that affect the region of the study. After a series of testing of domain sizes, a 20 km horizontal resolution outer (parent) domain (d01-Europe) with 265 × 200 grid points centered in the Mediterranean basin at 42.5 N and 16.00E was used. The high-resolution inner domain was set up at 5 km (d02-Greece) of horizontal grid spacing 185 × 185 grid points (see Fig 1). The set-up has used 40 vertical layers arranged according to the terrain-following hydrostatic pressure vertical coordinates, and one-way nesting has been applied to avoid possible noise during feedback from the inner domain to the coarse domain.

The physical parameterization is described in detail in (Politi et al., 2021). The initial and boundary conditions for the climate change assessment were derived from EC-Earth global model climate simulations for RCP4.5 and RCP8.5 scenarios and encompassed time slices representative of the historical or reference period (1980–2004), near-future period (2025–2049) and end of century as far-future period (2075–2099). For the future projections, the equivalent-CO2 concentration was updated every year in the WRF simulations according to the emission scenario.

The model used to initialize the dynamic downscaling process was EC-Earth simulations and projections that have been widely used for climate studies in the framework of CMIP5 and CORDEX (Jacob et al. 2014), (Prein et al. 2016), (Soares et al. 2017) and more recently in CMIP6 (Coppola et al. 2021). The validation of the results was done for the referenced period (historic) by comparing the

WRF historical simulations with available meteorological data from the Hellenic National Meteorological Service (HNMS). Below is a series of climate variable projections extracted for the target region (Figure 15).

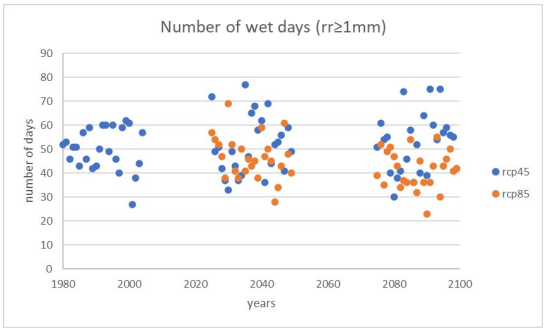

Number of wet days for daily percipitation ≥ 1mm per year for the historic period (1980-2004) and the future projections (2025-2045, 2075-2099) for two climate scenarios RCP4.5 and RCP8.5.

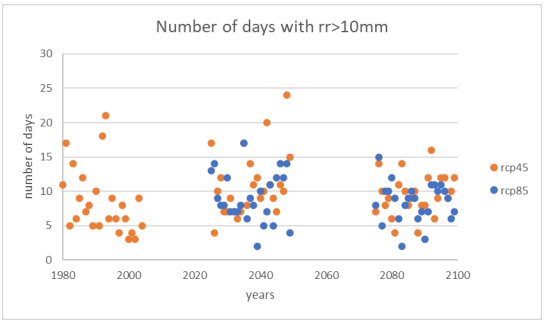

Number of days for daily percipitation>10mm for the historic period (1980-2004) and the future projections (2025-2045, 2075-2099) for two climate scenarios RCP4.5 and RCP8.5.

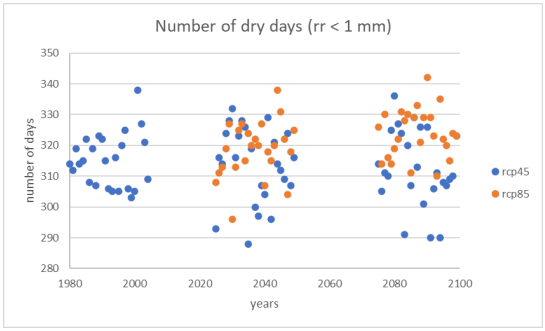

Number of dry days (precipitation< 1mm) for the historic period (1980-2004) and the future projections (2025-2045, 2075-2099) for two climate scenarios RCP4.5 and RCP8.5.

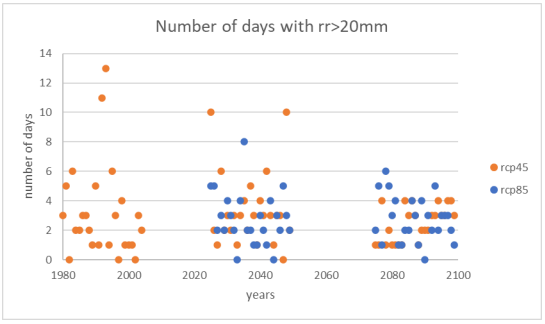

Number of days for daily percipitation>20mm for the historic period (1980-2004) and the future projections (2025-2045, 2075-2099) for two climate scenarios RCP4.5 and RCP8.5.

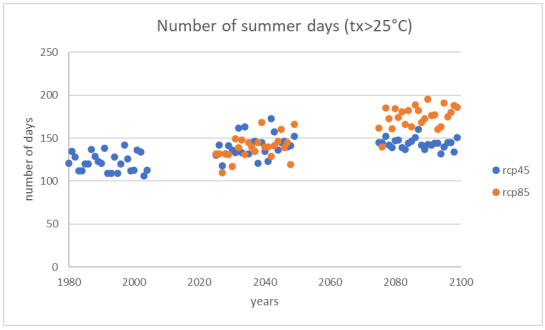

Number of summer days (max daily temperature >25°C) for the historic period (1980-2004) and the future projections (2025-2045, 2075-2099) for two climate scenarios RCP4.5 and RCP8.5.

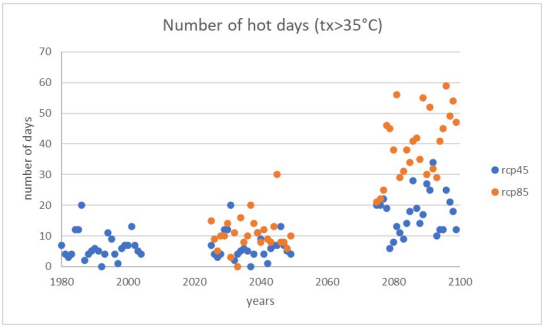

Number of hot days (max daily temperature >35°C) for the historic period (1980-2004) and the future projections (2025-2045, 2075-2099) for two climate scenarios RCP4.5 and RCP8.5.

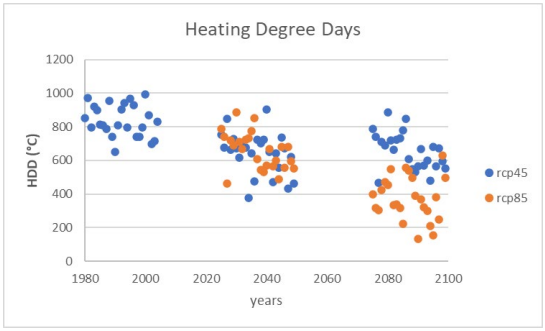	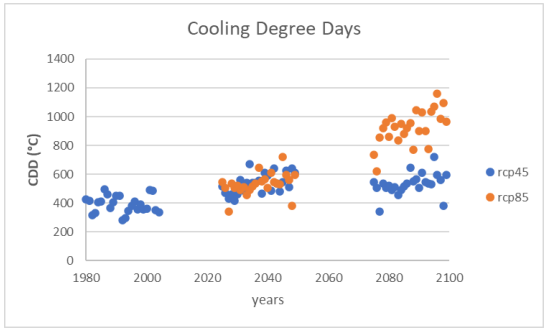
Heatinf Degree Days (HDD) for the historic period (1980-2004) and the future projections (2025-2045, 2075-2099) for two climate scenarios RCP4.5 and RCP8.5.	Cooling Degree Days (CDD) for the historic period (1980-2004) and the future projections (2025-2045, 2075-2099) for two climate scenarios RCP4.5 and RCP8.5.
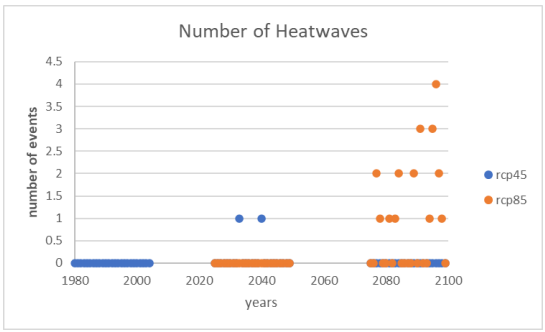	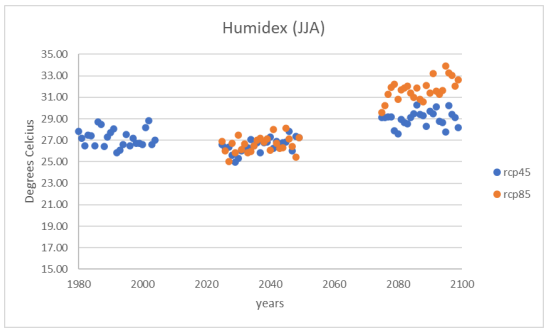
Number of heatwave events (3 concecutive days with max temperature >39°C) for the historic period (1980-2004) and the future projections (2025-2045, 2075-2099) for two climate scenarios RCP4.5 and RCP8.5.	Humidex indicator for the historic period (1980-2004) and the future projections (2025-2045, 2075-2099) for two climate scenarios RCP4.5 and RCP8.5.

Figure 15: Projections of different climate variables extracted for the target region.

6.2 Eco-hydrological model implementation

6.2.1 Model set-up and implementation

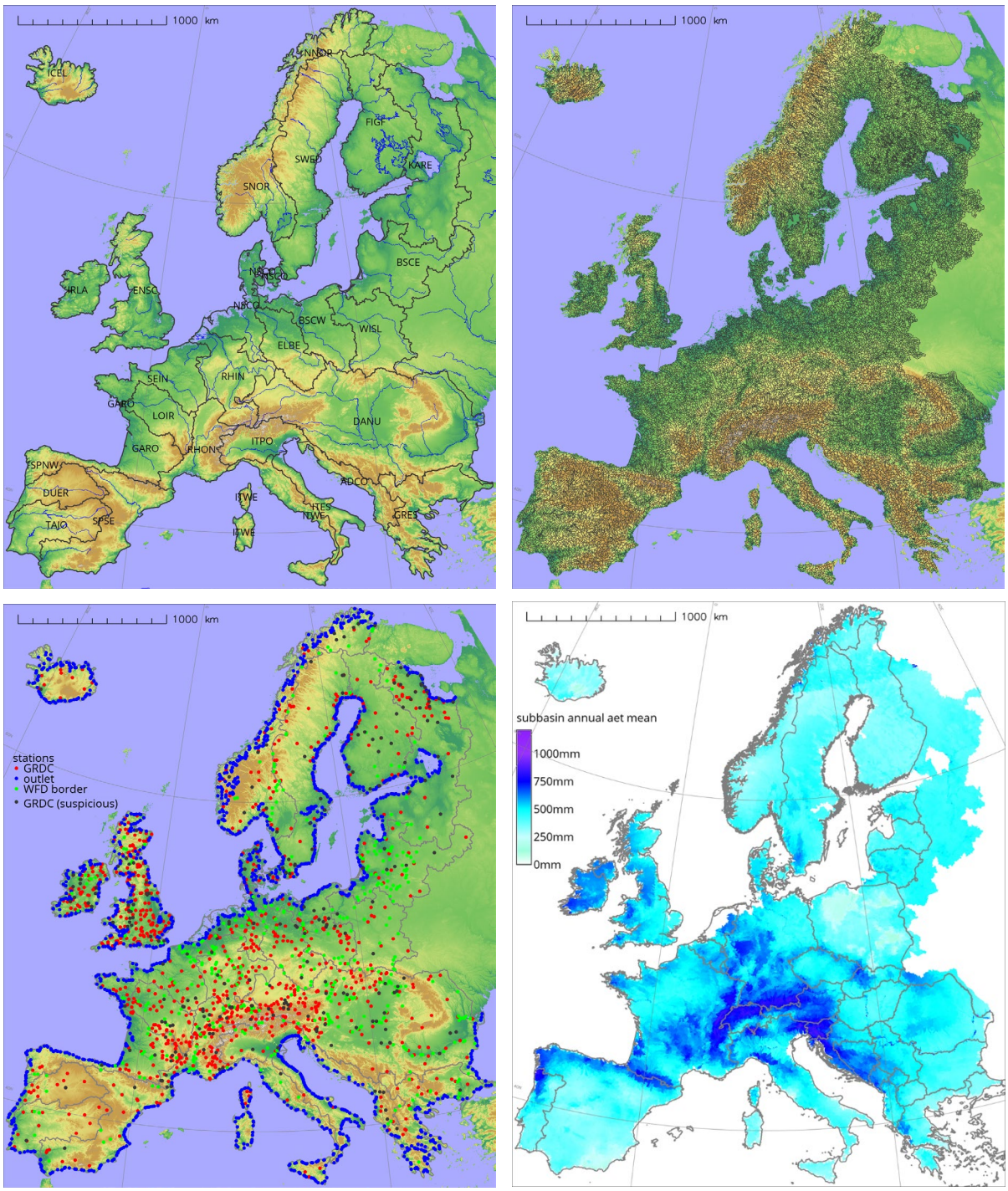

Figure 16: The 28 river regions (top left), the 31000 subbasins therein (top right), the 994 river gauge stations of the Global Runoff Data Centre (GRDC) and river outlets (bottom left), and the potential evapotranspiration as one hydroclimatic component simulated by the model SWIM (bottom right).

For the implementation of the model SWIM at European scale, 28 main river regions have been defined, for example for larger rivers (such as the Rhine, the Rhone, the Tagus etc.). The biggest basin considered is the Danube, where 18 countries are part of. Smaller river basins, as in Norway, have been combined into one river region.

The 28 river regions are further disaggregated into catchments representing main rivers, and within them, into ~31000 subbasins being tributaries of these rivers. The finest disaggregation level is the so called hydrotope, landscape elements with specific soils, land use/ vegetation pattern and elevation. Figure 16 shows the river regions and subbasins of the model set-up. The figure further gives the river discharge monitoring stations of the Global Runoff Data Centre (GRDC) used to calibrate and validate the model[8], and the river outlets and the river cross-sections of the river districts of the European Water Framework Directive[9]. The lower right map of Figure 16 illustrates how the output of model looks like, here in terms of potential evapotranspiration.

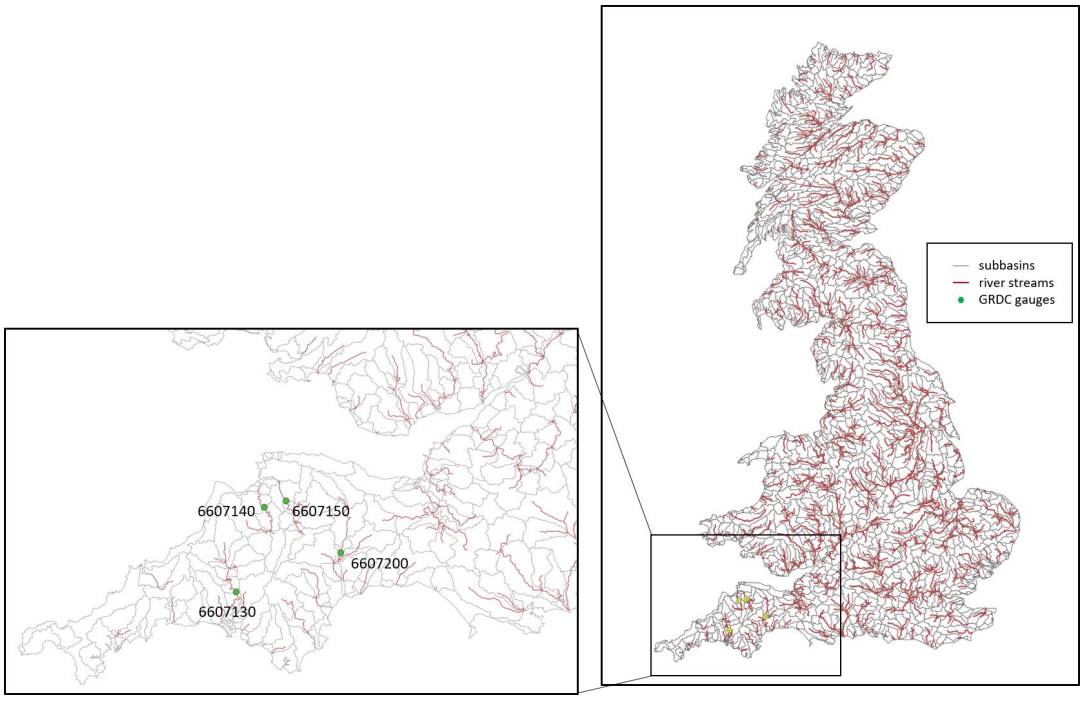

Figure 17: The river region Great Britain with the its 344 river catchments, 1630 tributaries/ subbasins and the river gauge stations of GRDC included. The zoom is into the West Country region, where the numbers indicate the gauge stations of the rivers Tamar, Torridge, Taw and Exe.

To illustrate the spatial aggregation in more detail, Figure 17 zooms into one of the river regions (Great Britain), and further into the location of one of the project demonstrators (West Country). The river region is subdivided into 344 river catchments with in total 1630 tributaries and 47,948 hydrotopes, the latter representing the specific environmental characteristics of the landscapes in Britain with its

[8] https://grdc.bafg.de/GRDC/EN/Home/homepage_node.html

[9] https://environment.ec.europa.eu/topics/water/water-framework-directive_en

composition of soils, land cover and relief. The green points illustrate the location of river gauge stations, where the model was validated.

The model SWIM was calibrated for the 28 river regions, but applying a global calibration, where each river gauge station in the region contributed to the goal function with its spatial share to the entire river region. The calibration was done multi-objective with satellite evapotranspiration (MODIS data[10]) as second variable in addition to river discharge. Figure 18 provides the calibration results, with the Nash and Sutcliffe coefficient as indicator for flow variability (left) and the pbias as indicator for the long-term annual water balance (right). Values above 0.5 for the flow variability and 25 % around 0 for the bias in water balance are considered as being good results (Moriasi et al. 2015).

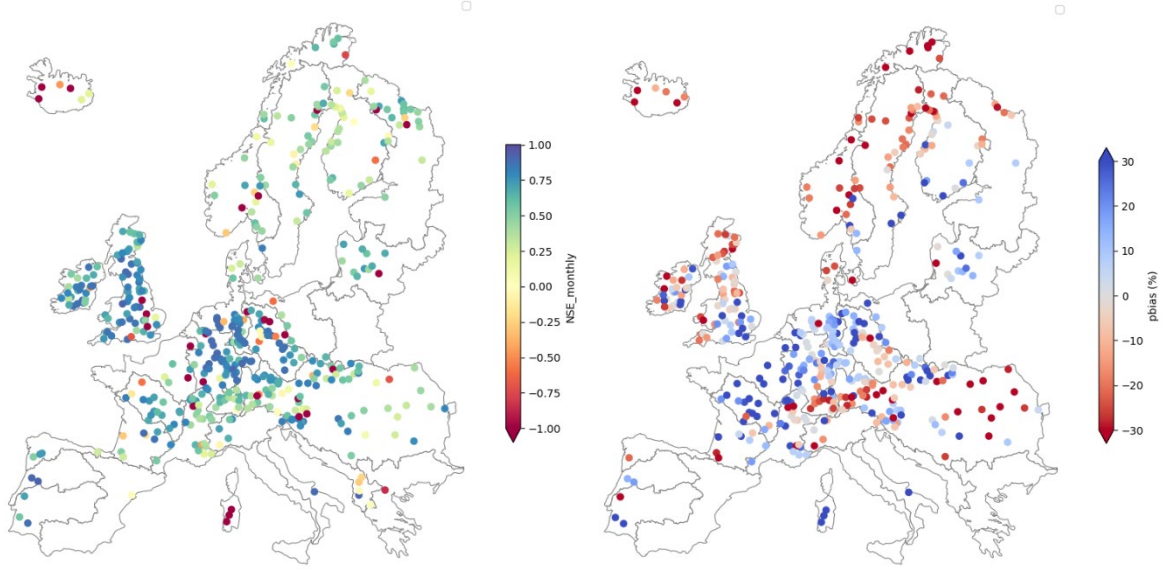

Figure 18: Calibration results for the flow dynamics (Nash and Sutcliffe value, left) and bias in long-term annual water balance (pbias, right) and the time period 1971-2000.

Visible is that the model simulates satisfying results in most regions of Europe. Larger problems occur, where local water management (for example reservoirs and water abstractions), not considered in the model set-up, have a strong impact on the observed values, and sometimes in very small basins having particular landscapes needing a more specific model adjustment.

This calibrated model setup is further used for future hydroclimatic projections by forcing it with the ISIMIP climate data. The outcomes of the model runs are different water balance terms like surface runoff, baseflow, subsurface runoff, groundwater recharge, actual evapotranspiration, potential evapotranspiration at each levels of spatial disaggregation, i.e., catchment, subbasin and hydrotope level. In Figure 19, we see the example case for change in mean annual groundwater recharge for Great Britain in near future i.e. between the period 2031-2060 and 1971-2000 and far future i.e. between the period 2071-2100 and 1971-2000. We see that groundwater recharge is generally increasing across all scenarios except for the north stretches of Scotland. The increase is more pronounced in far future.

[10] https://modis.gsfc.nasa.gov/data/dataprod/mod16.php

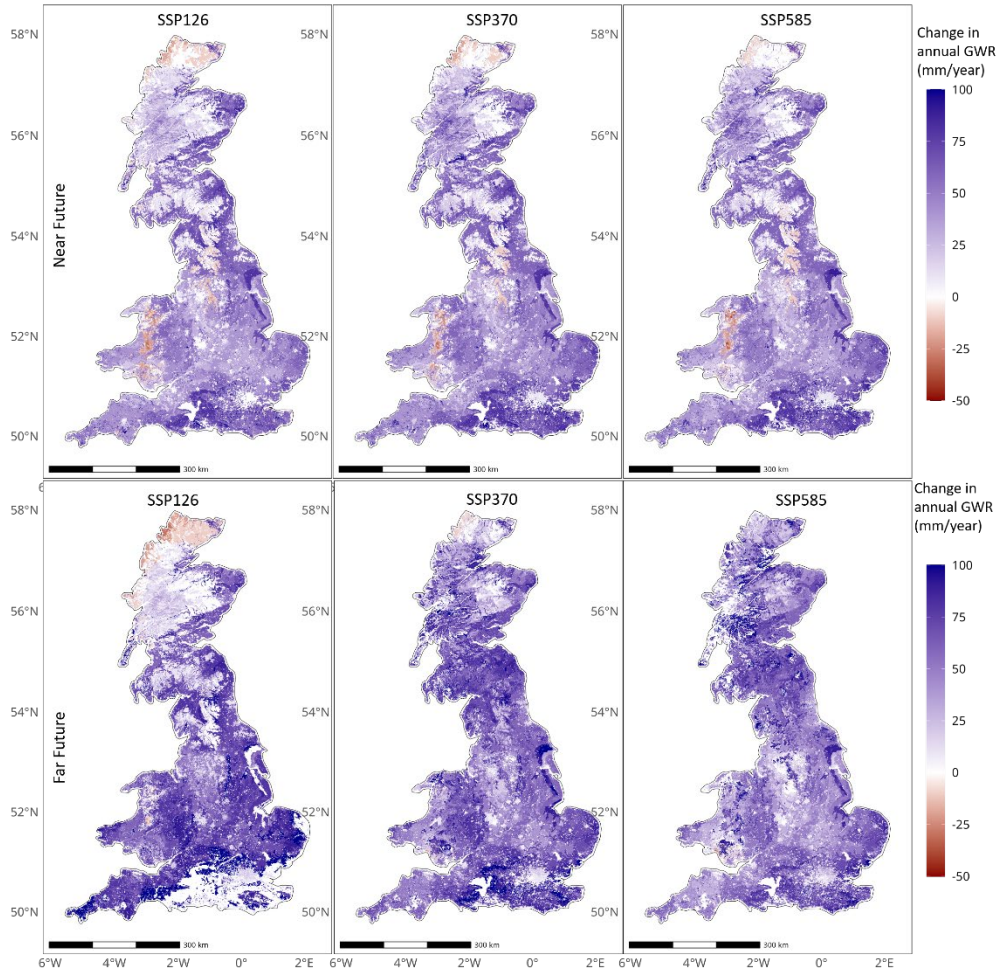

Figure 19: Simulated change in groundwater recharge for Great Britain between the period 2031-2060 and 1971-2000 (Near Future) in the top row and the period 2071-2100 and 1971-2000 (Far Future) in the bottom row for SSPs 126, 370 and 585.

6.2.2 Additional results at demonstrator level

The output data of the continental model set-up have in most cases a sufficient high resolution and quality to extract and analyse them at demonstrator level with the aim to further support the project partners in workshops and subsequent tasks. This is examplified here using the example of the West Country demonstrator of TransformAr[11].

Figure 20 provides a validation of the SWIM model comparing observed and simulated daily river discharge of the river Exe, which is a typical river located in West Country and drains into the Bristol channel at Exmouth. The river is approcimately 95 km long and has a catchment area of approximaltly 1500-km^2.

[11] https://transformar.eu/demonstrator-2-west-country-region-uk/

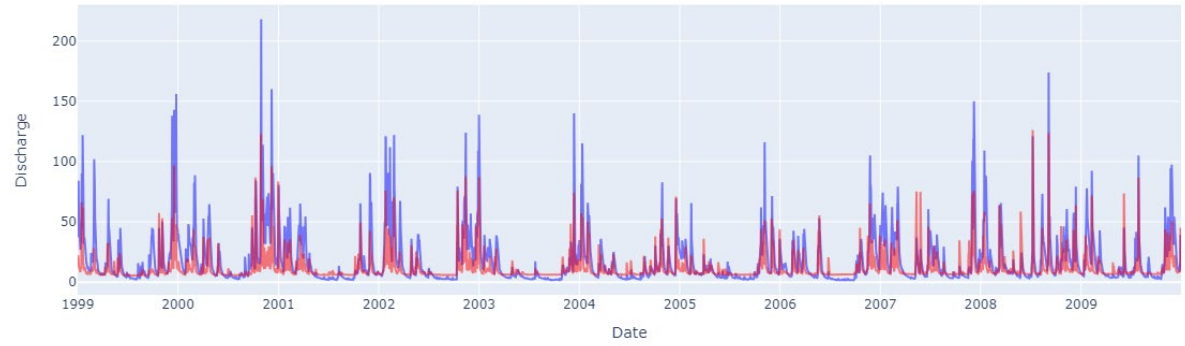

Figure 20: Observed and simulated discharge at gauge 6607200 (River Exe), a typical river in West Country.

The gauge station, where the data were collected from, has the number 6607200 (for the location see Figure 17). As said before, the model was not explicitly calibrated for the gauge, the results are the outcome of the global calibration for Great Britain. However, visible is that the model is able to reproduce the daily flow dynamics and the annual water balance, allowing to apply the model outcome for additional scenario analyses.

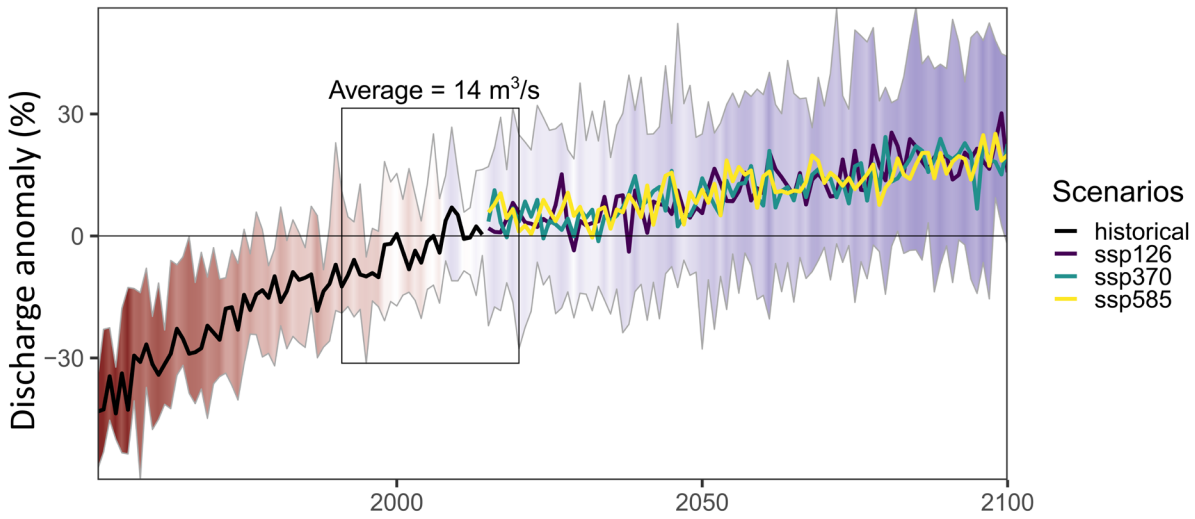

Figure 21: Change in annual river discharge of the Exe River considering three SSP scenarios and 10 GCM runs each as input for the model SWIM.

The impact of climate change on annual river discharge under different scenario conditions is shown in Figure 21. The results are that there is high agreement that annual river discharge and hence overall water availability in the basin will increase regardless which scenario is applied. This agrees with the observed trend in river discharge. The overall reason for this is that with the warmer temperatures, the water holding capacity of the atmosphere increases, and the prevailing westerly winds transport it from the Atlantic into the region. However, while precipitation increases with temperature and is higher in the high-end scenario, also evapotranspiration increases with temperature and this can compensate to a larger extent for the higher increase in precipitation in the “hot” scenario SSP5-8.5.

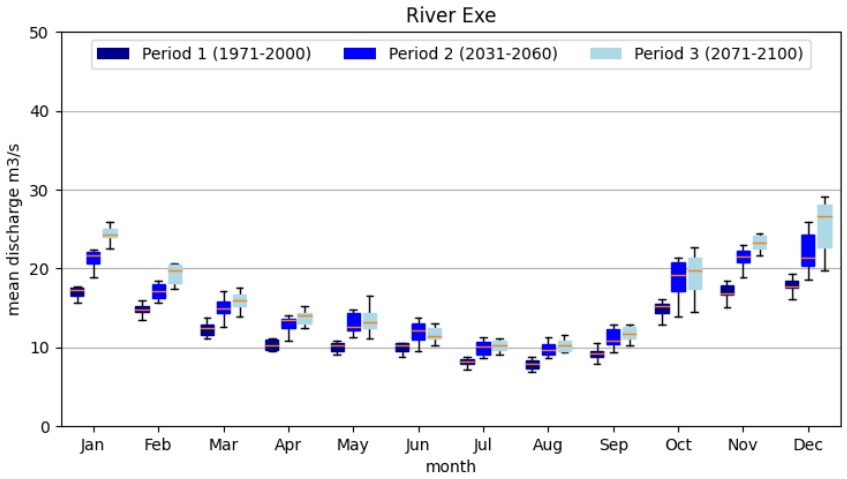

Figure 22: The monthly discharge of the river Exe for the historical and two future time periods considering high-end SSP5-8.5 scenario conditions.

The monthly changes of river discharge under high-end scenario conditions (SSP5-8.5) are given in Figure 22. Visible is that the discharge increases in all months, but more strongly in the winter season. While summer precipitation may decrease, larger precipitation in winter leads to more groundwater recharge, and the groundwater aquifer releases the water with some delay caused by the low flow velocity of groundwater so that the additional groundwater storage in winter can compensate for the decrease in precipitation in summer.

This is further elaborated in Figure 23, which shows the simulated long-term mean daily water flows and vegetation development at plot scale for a typical soil in West Country (a Cambisol) and under agricultural cultivation. The top left figure gives the results for the historical period 1971-2000 and the top right figure for the end of the century (2071-2100, scenario SSP5-8.5). The lower left graph gives the differences, and the lower right one the change in soil water and plant water stress.

The vegetation development is given by the growth of the Leaf Area Index (LAI, the number of leaf layers above ground), and the hydrological flows are in mm/m^2.

The results show that precipitation increases in winter and decreases in summer (blue lines). The increase in winter precipitation leads also to more surface runoff (black) and groundwater recharge (light blue) in winter, while the latter may decrease in summer. The crops (green, winter wheat followed by grass in the historical period, and followed by summer barley at the end of the century) extends and the faster growth of winter wheat in autumn may lead to a fully developed vegetation cover in winter. Also visible is that in summer, a second crop may fully develop, in this case summer barley. While precipitation increases in winter, it may decrease in summer, and this together with the increase of plant water demand in a warmer and in summer hotter climate leads to less water availability in the soils and higher water stress of plants (Figure 23, bottom right).

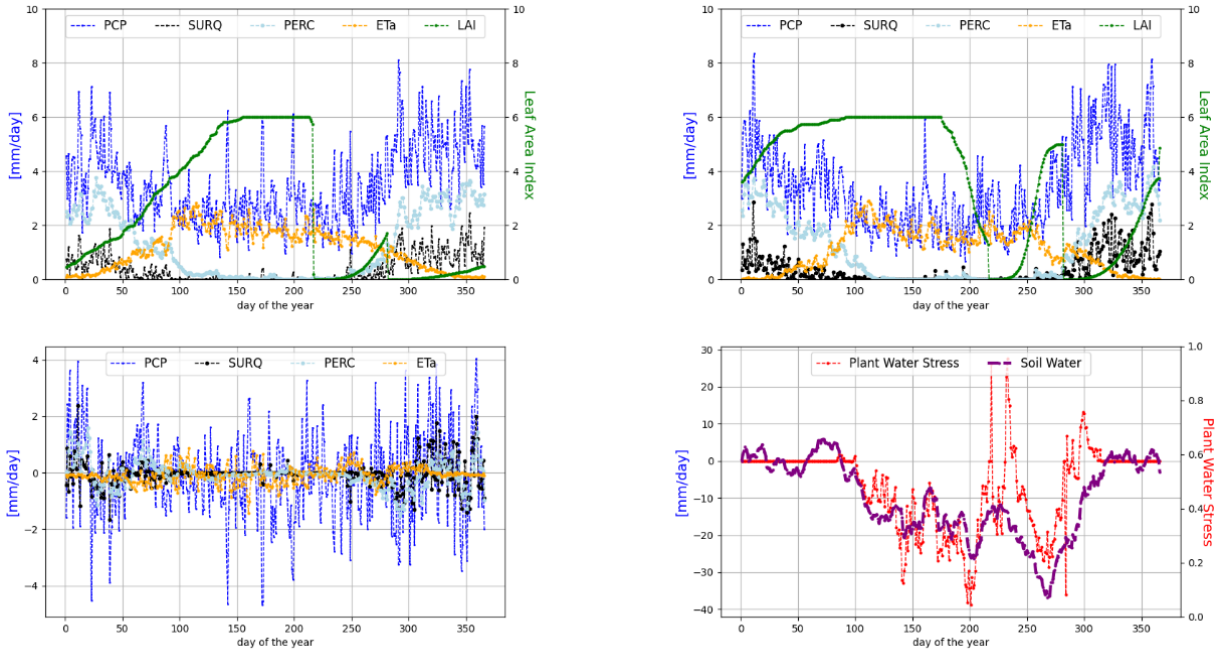

Figure 23: The simulated long-term mean daily water flows and vegetation development at plot scale for a typical soil in West Country (a Cambisol) and under agricultural cultivation (scenario SSP5-8.5). Top left: the historical period 1971-2000; top right: the end of the century (2071-2100). Lower left: the differences; lower right: change in soil water and plant water stress (PCP: precipitation, Surf: surface runoff, Perc: percolation, Eta: actual Evapotranspiration, LAI: Leaf Area Index).

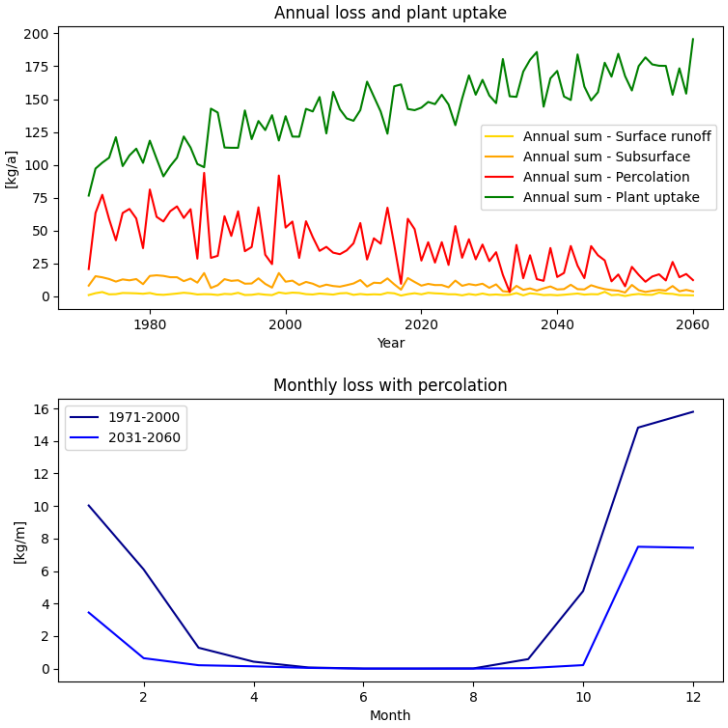

Figure 24: Simulated development of total annual nitrate loss with surface runoff, interflow and percolation and plant uptake (top), and development of monthly percolation losses (bottom).

The modelled development of total annual nitrate loss with surface runoff, interflow and percolation and plant uptake and the development of monthly percolation losses are shown in Figure 24. With the

increase in temperature, the vegetation period extends and, as illustrated in Figure 23, winter crops may fully develop before winter. This may lead to more uptake of nitrogen by plants (Figure 24 top) and to a strong decrease of percolation losses in winter (Figure 24 bottom). Important to know is that the fertilizer regime didn't change over the modelling period.

The development of flood extremes in West Country/ the Exe River was also provided and is shown and discussed in the next section.

6.3 Modelling of extremes

6.3.1 Weather generator implementation

Rare extreme events like floods or heat waves often have strong socio-economic impacts. However, due to the limited length of observational or model simulation time series, estimating the statistical properties of such rare events can be challenging. Typically, determining the return period of an extreme event requires fitting the empirical event distribution to a generalized extreme value (GEV) distribution. The accuracy of this fit heavily depends on the number of available events, and consequently, the length of the time series. Climate time series, whether derived from observations or model simulations, usually span around 100 years. This relatively short duration restricts their usefulness for extreme value analysis. To address this limitation, stochastic weather generators are often employed to produce synthetic time series of arbitrary length while preserving the statistical characteristics of the original data. In our project, we have extended, refined, and applied a stochastic weather generator known as IMAGE-PIK, which is based on the Imperial College London weather generator IMAGE (Imperial College Weather Generator). In the following sections, we will present the IMAGE-PIK simulations and conduct a brief evaluation.

To demonstrate the advantages of IMAGE-PIK in estimating GEV distributions, Figure 25 presents the return periods of extreme temperature and precipitation events, along with a GEV distribution fit for both an IMAGE-PIK simulation and the original data. IMAGE-PIK not only allows for the estimation of much longer return periods but also provides a better fit to the GEV distribution. More validation results are presented in Chapter 10.2.7 (Annex).

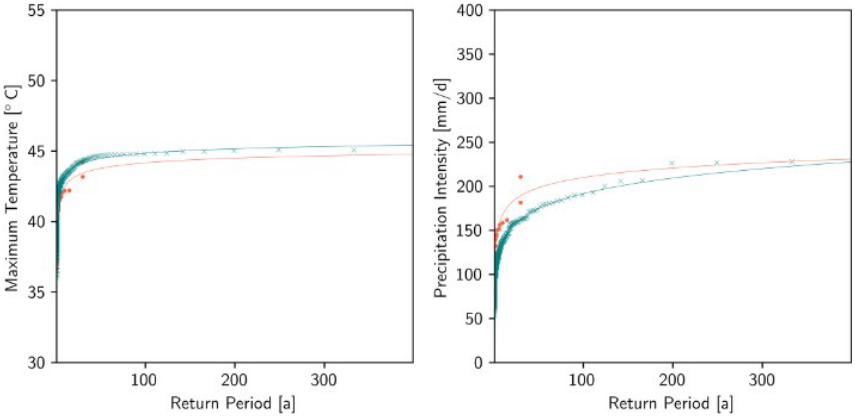

Figure 25: Return period of extreme temperature and precipitation events. The plot represents the results of a single model simulation (KNMI-RACMO22E driven by EC-EARTH for the period 2071-2100 under RCP 8.5 greenhouse gas concentration scenario). Original model data is shown with orange color, while the ISIMIP-PIK simulation is shown in green. Extreme temperature events are the maximum daily maximum temperatures each year. Precipitation events are the highest precipitation events each year. The lines represent a GEV-fit of the different events.

Future projections

Using the IMAGE-PIK weather generator, we simulated 1,000 years of the IMPACT2C regional climate model ensemble. These simulations were based on three greenhouse gas concentration scenarios and covered three distinct time periods: 2011-2040 (early), 2041-2070 (mid), and 2071-2100 (late). Table A1 of the Annex summarizes the regional climate models and their corresponding global climate models used for each scenario. Each 30-year model period was extended to 1,000 years using IMAGE-PIK.

Figure 26 presents the annual mean temperature changes from the 1,000-year IMAGE-PIK simulations for each greenhouse gas concentration scenario and time period, compared to the 1,000-year simulation of the historical period (1971-2005). Consistent with previous studies (Christensen and Christensen, 2007; Jacob et al., 2014; IPCC, 2021), temperature is projected to increase for all scenarios and periods. The most significant temperature rise, up to 6 °C, is simulated for the late period 2071-2100 under the RCP 8.5 scenario. The smallest changes, between 1 °C and 2 °C, are projected under the low-emission RCP 2.6 scenario. The RCP 2.6 scenario also exhibits the lowest overall temperature increase across the three periods, while the RCP 8.5 scenario shows the most substantial increases over time. For all scenarios and periods, the temperature rise is relatively uniform across Europe, with slightly higher increases in northeastern, Mediterranean, and mountainous regions, particularly in later periods and under higher greenhouse gas concentration scenarios.

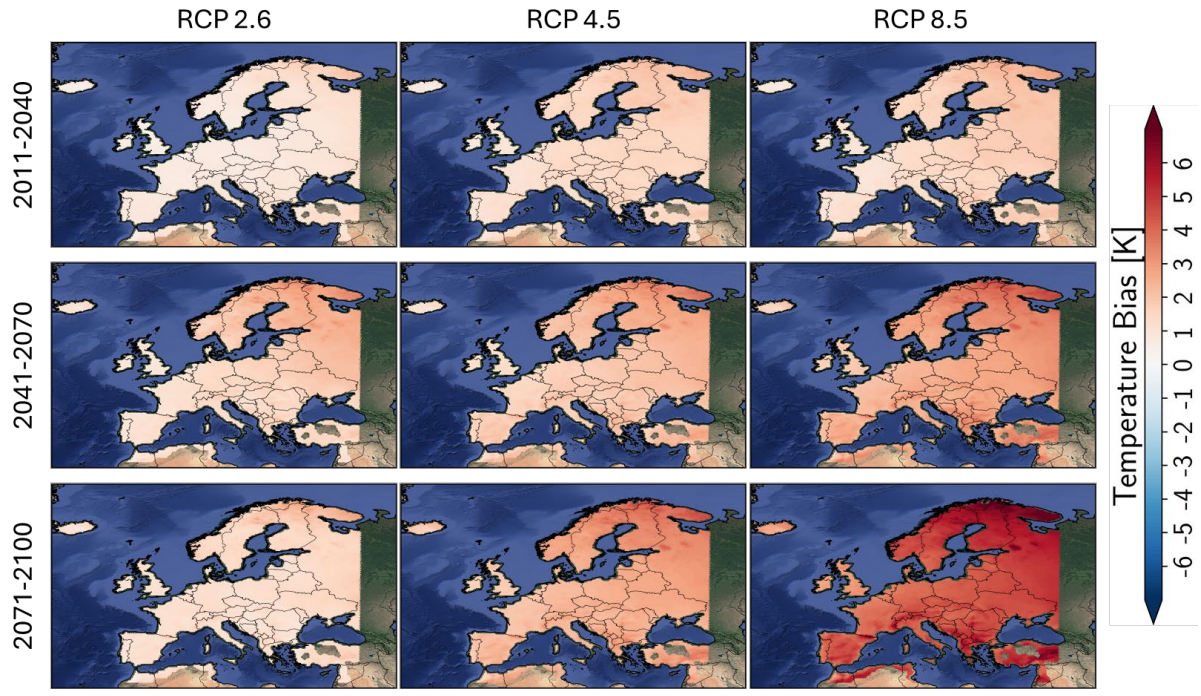

Figure 26: Annual mean temperature changes as simulated by the bias-adjusted IMAGE-PIK simulations based on the IMPACT2C ensemble for three different greenhouse gas concentration scenarios (RCP 2.6, RCP 4.5, and RCP 8.5) and future periods. Each period represents a 1000-year simulation of IMAGE-PIK based on IMPACT2C simulations of that period. Hence, each 30-year period of a IMPACT2C model is extended to 1000 years by IMAGE-PIK. The changes are calculated with respect to another 1000-year simulation based on the historical IMPACT2C simulation for the period 1971-2005.

Projected precipitation changes, shown in Figure 27, display more variability across Europe. Under the higher greenhouse gas concentration scenarios RCP 4.5 and RCP 8.5, particularly in the mid and late time periods, a significant decrease in precipitation is expected over the Mediterranean region. Conversely, most other regions are projected to experience increased precipitation across all scenarios and periods. This increase is most pronounced over European mountain ranges and the Scandinavian Peninsula, with changes ranging from -0.4 mm/day in southern Europe to +0.7 mm/day in northern Europe.

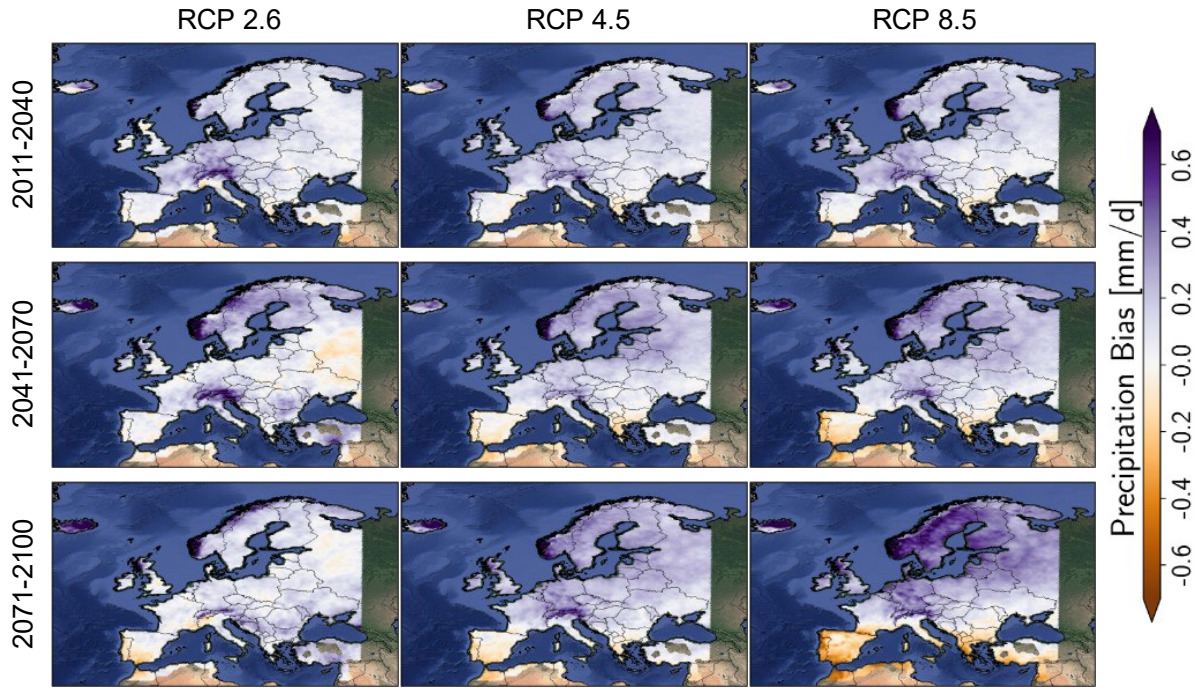

Figure 27: Same as 28 for precipitation.

The main advantage of IMAGE-PIK lies in its enhanced representation of rare events. As an example, Figure 28 illustrates the return periods of high-temperature events simulated by IMAGE-PIK for Germany, based on individual IMPACT2C simulations. The simulations reveal a wide range of temperature intensities across different models and return periods. Moderate high-temperature events with a 10-year return period range between 40.2°C and 47.6°C, corresponding to an increase of 2.0°C to 9.4°C from the historical period. Similar increases are observed for events with longer return periods. In extreme cases, temperature events with a return period of over 250 years can reach up to 50°C in Germany.

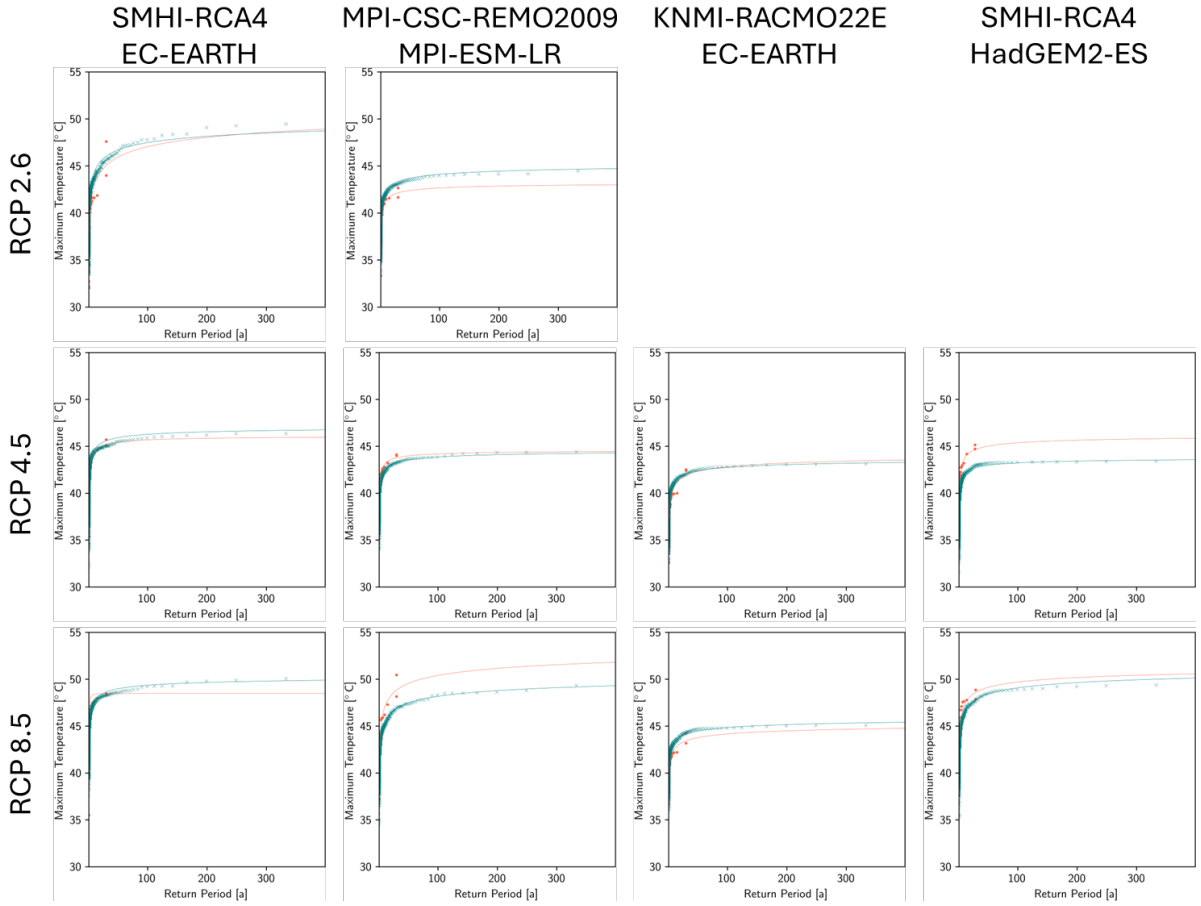

Figure 28: Return period of extreme temperature events as simulated by each IMPACT2C regional model. An extreme temperature event is defined as the highest temperature of each day and grid box over Germany in each year. The events for the original IMPACT2C model simulations are shown in orange, while the IMAGE-PIK simulations are shown in green. The results correspond to the simulations for the time period 2071-2100 under different greenhouse gas concentration scenarios.

6.3.2 Floods under climate change

The simulated weather data are part of the model chain climate model – weather generator – SWIM – CaMa-Flood and have subsequently been applied to all European river regions to simulate flood extremes under climate change conditions.

The simulated changes in max. annual floods for all river regions are shown in Figure 29 and as comparison of the time periods 1971-2000 (historical reference) and 2031-2060 (near future) and 2071-2100 (far future). Visible is that the intensity of flood events increases with the increase of global temperature from the near future to the far future and from moderate climate change (SSP1-2.6) to strong climate change (SSP5-8.5). The scenarios hardly differ in the near future, and are stronger until end of the century, when also the differences in warming are the strongest. Also visible is that the increase in flood intensity is more pronounced in central Europe and Great Britain, while northern basins in Scandinavia may have a decrease in all scenarios and in the near as well as in the far future.

The greatest difference between scenarios is in the far future, where with increasing temperatures and especially in SSP3-7.0 and SSP5-58.5 the Iberian Peninsula and also parts of eastern Europe show a decrease in maximum annual flows.

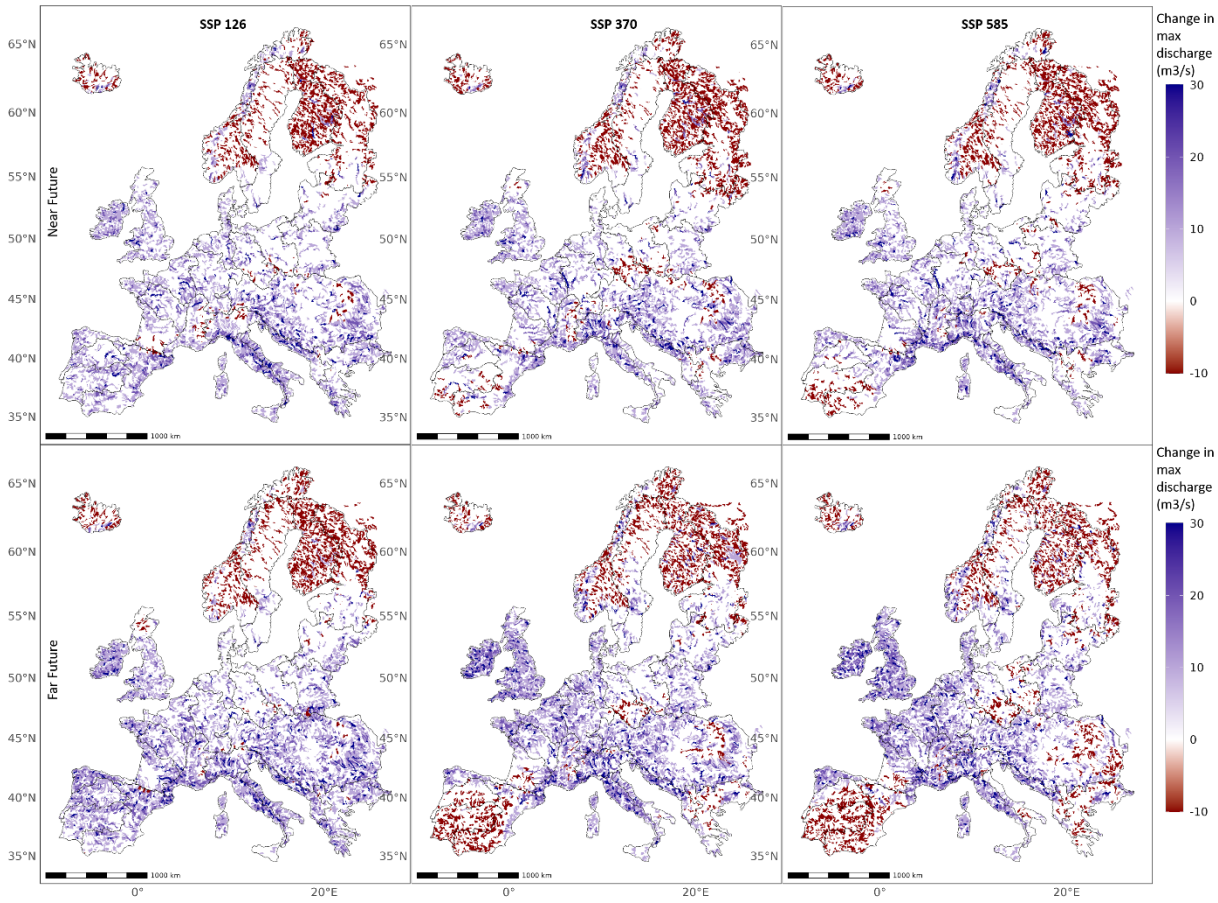

Figure 29: The simulated changes in maximum annual flood events exemplarily shown for the subbasins of all river regions in Europe and as comparison of the time periods 1971-2000 (historical reference) and 2031-2060 and 2071-2100 (far future).

As part of the validation of the simulated floods, Figure 30 provides a comparison of the inundated areas simulated by CaMa-Flood and the observed ones in a river section located in Europe's largest river basin (near Ingolstadt) during the well documented 1999 spring flood. Visible is that the model reproduces the areas inundated with smaller exceptions. Also given are photos of buildings and other infrastructure illustrating the extent and damaging potential of the flood.

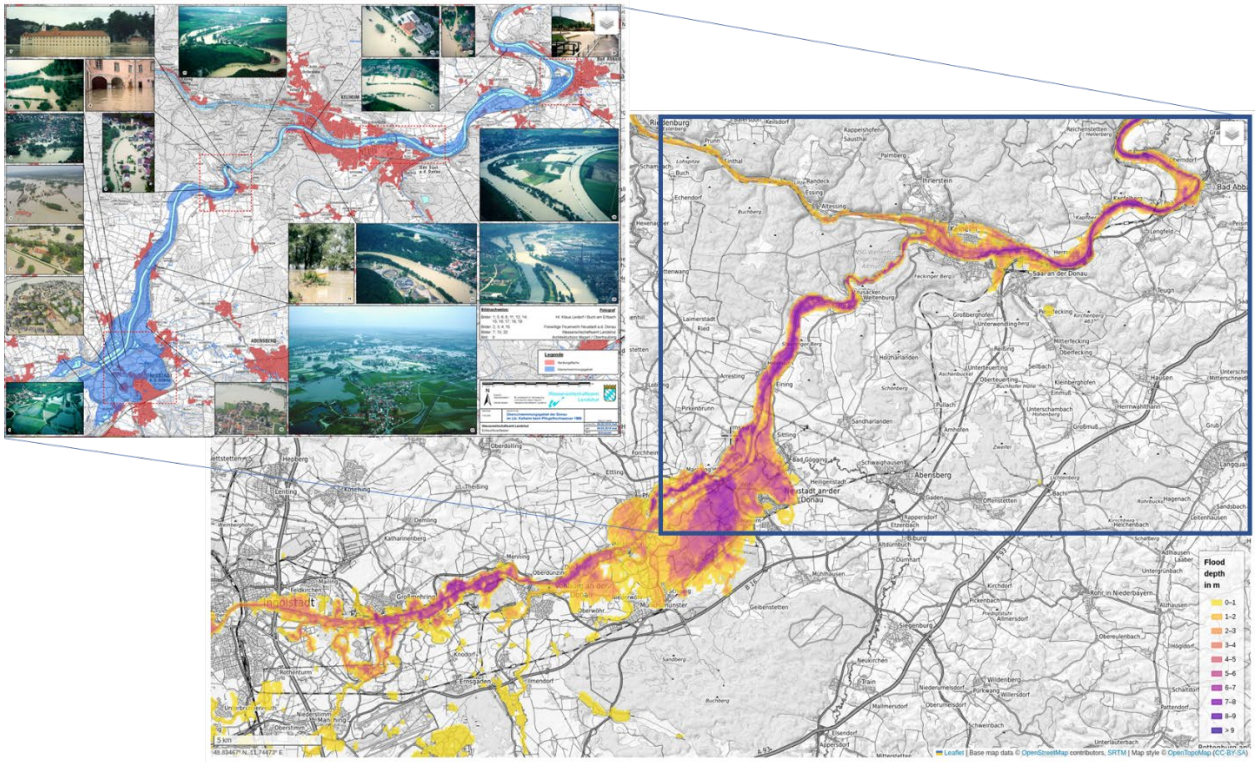

Figure 30: The simulated inundation depth (reddish colors) during the spring flood 1999 in the Danube basin around Ingolstadt (base map) and the official map of the observed (bluish colors) event (top left)[12].

The simulated mean annual financial losses in the Danube basin simulated by the model chain are given in Figure 31 for the reference period 1971-2000 and the change until now (2006-2035) and in the near (2031-2060) and far (2071-2100) future and for the high-end scenario SSP5-8.5. The related damage functions transferring inundation depth and flow velocity into river section specific flood losses were derived in the EU project H2020_Insurance (Hattermann et al. 2018) and are applied currently to calculate the losses in Europe in cooperation with the EU project Directed[13]. The results indicate that flood losses increased already since the end of the last century and will further increase under climate change conditions.

[12] https://www.wwa-la.bayern.de/hochwasser/hochwasserereignisse/pfingsthochwasser99/doc/uebersichtskarte_bilder_hw99.pdf

[13] https://directedproject.eu/about/

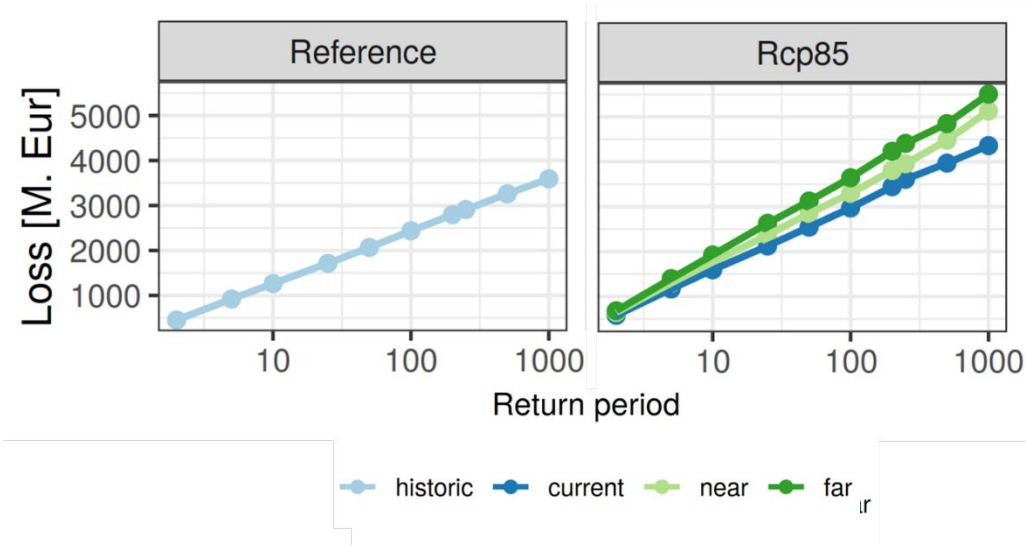

Figure 31: The simulated mean annual flood losses in the reference period 1971-2000 (left) and the change until now (2006-2035) and in the near (2031-2060) and far (2071-2100) future (right) and for the high-end scenario SSP5-8.5.

Finally, development of flood extremes for the Exe River with SSP5-8.5 (top) and SSP1-2-6 (bottom) data simulated by SWIM as input is shown in Figure 32. There is a clear increase in the number of floods and in their intensity in SSP5-8.5, where a former 100year flood may appear ~10 times more often until end of the century, and the water volume of a "new" 100year flood increases by ~50 %. This is relevant, because critical infrastructure is mostly adjusted to protect against events of a certain intensity (or return level), and settlements and industry, for example protected by a dyke designed for a 100year flood, have a much higher risk to be flooded in a warmer climate.

In contrast to this, development of floods under SSP1-2.6 scenario conditions shows a different pattern: the increase of volumes until mid of the century is comparable to the one of the high-end SSP5-8.5 scenario, but may decrease afterwards. This is in line with the temperature development under SSP1-2.6 scenario conditions, where a peak is reached around mid of the century, and a slow decrease afterwards.

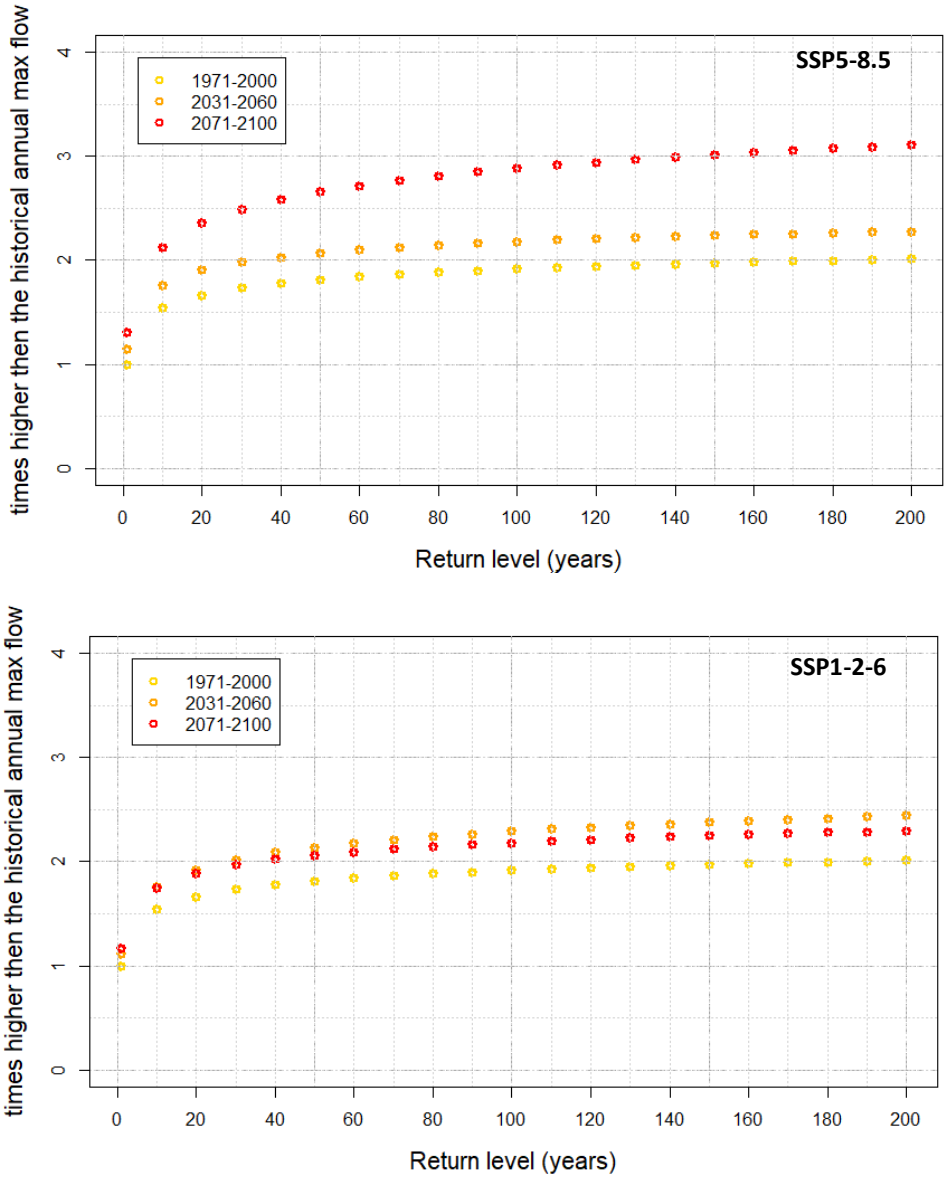

Figure 32: Development of flood extremes for the Exe River with SSP5-8.5 (top) and SSP1-2-6 (bottom) data simulated by SWIM as input.

6.4 Crop modelling

6.4.1 Aggregating climate impact projections on crop productivity for EU at NUTS2 level

Crop modelling results in TransformAr are based on the newly released projections produced by the third simulation round of the Inter-Sectoral Impact Model Intercomparison Project (ISIMIP3B). The ISIMIP database provides modeling output of agricultural production in terms of crops cultivated for both food and energy purposes at a global scale. Data from eight different impact models have been used for crop modelling purposes in TransformAr: CROVER (Okada et al., 2018), CYGMA1p74 (Iizumi et al., 2017), EPIC-IIASA (Balkovic et al., 2014), LDNDC (Haas et al., 2013), LPJmL (von Bloh et al., 2018), LPJ-GUESS (Lindeskog et al., 2013), PEPIC (Liu et al., 2016), PROMET (Mauser et al., 2015) and SIMPLACE-LINTUL5 (Webber et al., 2015). The crop modelling simulations are driven by five bias-corrected global climate models of the latest generation (CMIP6): UKESM-01 LL, GFDL-ESM4, IPSL-CM6A LR, MPI-ESM1-2-HR and MRI ESM2-0. Within ISIMIP3B, the impact models mentioned above generate quantitative information on yield for nine crops, of which seven were used in TransformAr analyses: Maize, Potato, Rice, Sorghum, Soy and Wheat (spring and winter) managed in both rainfed and fully irrigated conditions.

The selected agricultural model simulations consider the future CO2 fertilization effect to account for the effect on crop physiology of changing CO2 concentration, according to SSP scenarios. Changes in management up to 2015 are also considered for the chosen socio-economic scenarios (i.e., human influence and land-use scenarios in terms of variation of land use, water abstraction, nitrogen deposition and fertilizer input). Data are delivered yearly per growing season with a resolution of 0.5°. The crop model simulations have a global spatial coverage under the assumption that all crops are cultivated everywhere. The data are available for the historical (1850-2014) and future (2015-2100) climate. The scenarios SSP126, SSP370, and SSP585 are used to represent future climate change and socio-economic conditions.

Within TransformAr, the global crop modelling data were aggregated at NUTS2 level by taking the average of the 0.5° pixels falling within each region boundaries. To relate the projected change in crop yields to the economic dimension, the contribution of each studied crop to the total crop basket was quantified for each NUTS2 in terms of harvested area (ha), using data from EUROSTAT and MAPSPAM (You et al., 2019). Thus, the cumulative yield change of all studied crops in each region was calculated as the weighted average of the individual yield changes, with the individual harvested areas used as weights as shown in equation 1:

$$Weighted\ Cumulative\ Yield\ Change\ (\%) = \frac{\sum Y_i * HA_i}{Total\ HA} \quad (1)$$

where *Yi* is the yield of any of the considered crop (i) and *HAi* is the harvested area of that same crop. The cumulative yield change is expressed as the percentage difference in the yield of all studied crops with respect to the 1985-2015 average, weighted by their current (2010-2020) average harvest area. This quantity allows us to relate the changes in crop yields projected by the ISIMIP impact models to the current production practices at NUTS2 level, hence representing a fundamental component of an

integrated risk assessment for the European agricultural sector. Figure 33 shows the weighted cumulative yield change in 2030 (2015-2045 average) and 2050 (2035-2065 average) under the SSP1.26 and SSP5.85 greenhouse-gas emission scenarios at NUTS2 level.

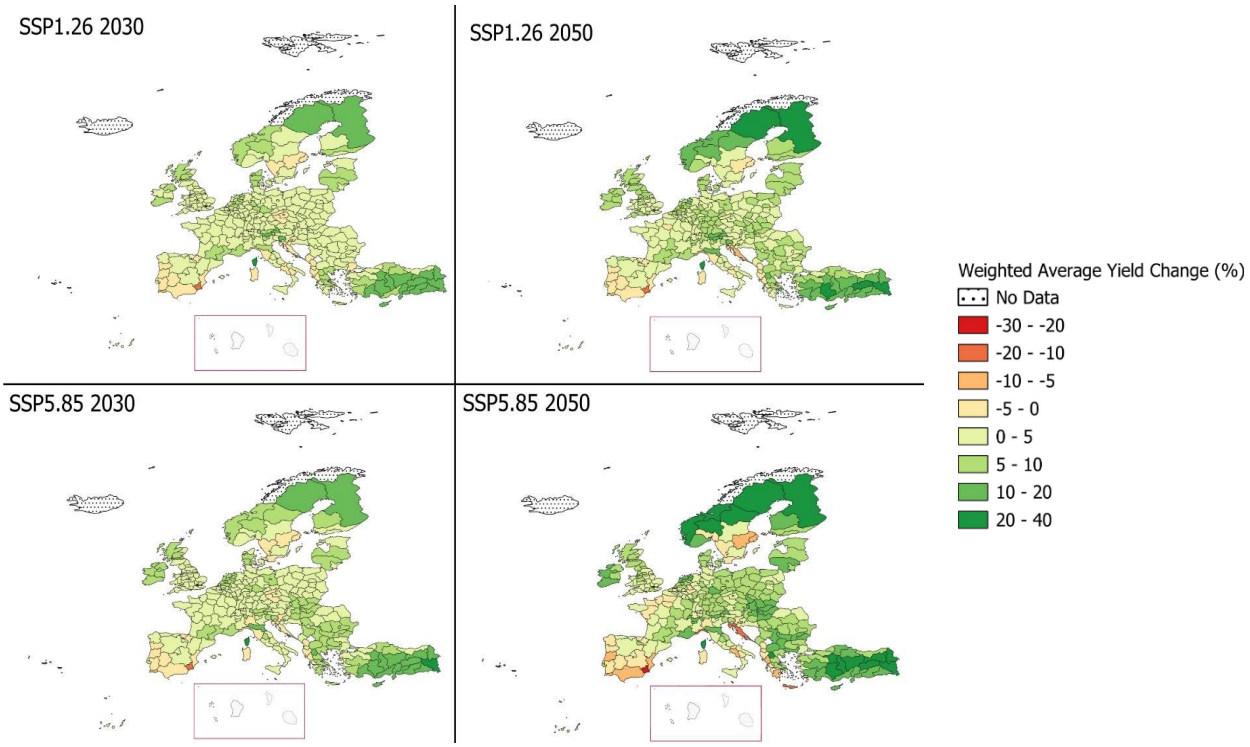

Figure 33: Cumulative yield change (%) at NUTS2 level in 2030 and 2050 following ssp1.26 and ssp5.85 emission scenarios. The yield change refers to the weighted sum of maize, potato, rice, sorghum, soy and winter wheat yields and is expressed as the percentage difference from the same quantity averaged over 1985-2014.

6.4.2 Climate impact on agriculture sector of the Caribbean and Guadeloupe

Guadeloupe is a French overseas department located in the intertropical zone of the northern hemisphere (Figure 34). With a population of 395,000 inhabitants over a relatively small island, it has quite a large population density (395 persons per square km). This insular department is highly vulnerable to several climate changes risks, such as wider hot seasons, hurricanes, droughts, sea level rise, increasing flash floods (Orec, 2016; OECS, 2021).

Guadeloupe is considered to be the 5th worldwide hotspot of biodiversity, and in the meanwhile also vulnerable to several global changes. Similar to other islands in the Caribbean Community, agriculture is an important sector that must mitigate the effects and adapt to the changing climate. Both these can be achieved by building resilience to natural disasters, and by committing to the agro-ecological transition from mainly large commercial-scale monoculture to a better balance with more diverse and sustainable farming for local use.

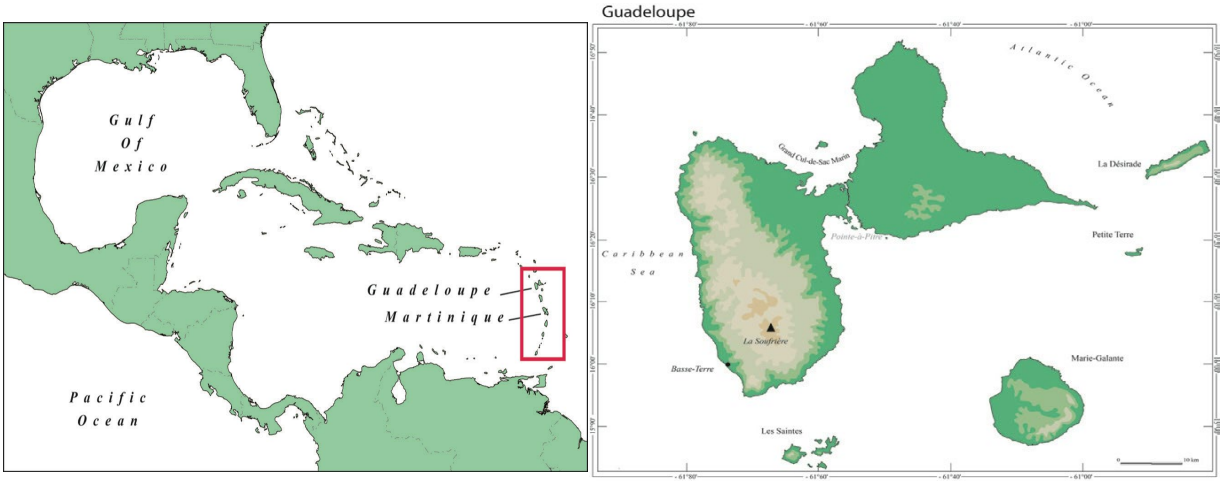

Figure 34: Geographical position of Guadeloupe Island in the Caribbean.

The main economic sector of this island is business services, followed by agriculture. Moreover, farming remains historically, socially and culturally important to the identity of the islands. Farm sizes range from less than one hectare to more than 100 hectares. Agriculture production in Guadeloupe is dominated by sugar cane and bananas plantations, which are occupying more than 50% of the usable agricultural land of the island. Most of the sugar cane products (60%) and bananas as fruit (95%) are exported to France (4th INNOVA e-zine, 2019). The total cropping area is 35,000 ha, which represents 18.2% of the area of the island. Sugarcane and bananas are the two major crops, mainly dedicated to the export market. The sugarcane area is 12,310 ha, mainly located in Grande-Terre. Banana production is located in Basse-Terre on approximately 2400 ha (Agreste, 2019). Almost 7000 ha of land in the south of Basse-Terre are polluted by chlordecone, making these lands unsuitable for the cultivation of certain foodstuffs such as tubers for several centuries (DAAF Guadeloupe).

Export agriculture in the Caribbean (e.g., Guadeloupe Island) consists of traditional crops including bananas, sugarcane, coffee, citrus, cocoa and rice. Historically, banana and sugarcane have been the major agricultural exports and have benefitted from specialized market conditions, which have generally been removed within the last decade. Many of these economies are monocrop exporters, serving one major market, which results in a high degree of vulnerability. The European Union and the United States of America markets alone account for more than two-thirds of Caribbean agricultural exports, with less than 15 % of exports going to other destinations. Within the Caribbean subregion, the Organization of Eastern Caribbean States (OECS) is probably more vulnerable to climate change than other CARICOM Member States, due primarily to their disproportional dependence on agriculture (FAO, 2007). On the other hand, Guadeloupean agriculture is undergoing a shift in production towards domestic markets, which includes a transition towards cropping systems based on annual crops (e.g., annual vegetables, tuber crops, and root crops), because of declining demand on global markets for the major agricultural exports from the region (e.g., sugar, bananas, cocoa) (Saint Ville et al. 2015).

Impact of climate change on the agricultural sector of Guadeloupe

A key factor influencing the subregion's vulnerability to the impact of extreme weather events is the fragility of agriculture-based economies which are heavily dependent on their natural environment to

sustain livelihoods. Large-scale losses are not unusual, as more than half of the countries in the subregion depend on one or two commodities for export revenues. In 2007, Hurricane Dean destroyed major export crops, Haiti lost large portions of its banana, bean, and yam crops to high winds and salt water intrusion on its southern coast, and there was extensive damage to Caribbean agricultural sectors. Many Islands have discontinued the production of bananas for export, partly due to frequent crop devastation from intense hurricanes (and partly due to loss of preferential access to European markets). Some Caribbean islands ceased other agricultural operations due to diseconomies caused by severe weather conditions including extreme droughts, floods and storms as well as variations in temperature (UN, 2011). The investigations suggest that changing climatic conditions associated with temperature, precipitation and extreme events may be of major importance to the survival of Caribbean agriculture. Most Caribbean agriculture (e.g., Sugarcane and Banana cultivations) is and will be likely prone to flooding, hurricane, droughts and erosion.

(a) Sugarcane

Projected temperature changes show no significant impact on sugarcane yield in most of Caribbean region when annual data were used. In the Jamaica case study, where monthly data were used, the research found that any deviation or increase above the optimal temperature of 29° C has a negative impact on sugarcane yield. The results further suggested that sugarcane yield is more sensitive to changes in rainfall than temperature in this geographic region. For instance, in Guyana, a 5% increase in rainfall above the optimum level causes sugarcane production to decline by 8%. In Jamaica, sugarcane production is concentrated during a growing season between April to July, when rainfall does not fall below the optimal level of about 190 mm per month, and when it is less than, or equal to, 196 mm per month during the ripening season (August to November). During the reaping season (December to March), the optimal rainfall requirement is at least 102 mm per month on average. Following climate projections, yields from 2020 to 2050 may be lower than those under the historical period (UN, 2011). ISIMIP agriculture projections after CMIP5 climate drivers predict by 2050 a drop of productivity between 5% and 15% compared to historical conditions.

A study developed by Chopin and Sierra 2019, using A1B IPCC scenario showed that climate change increased soil organic carbon losses at Guadeloupean territory scale by 29-fold, and up to 30% of these losses were linked to pluriannual sugarcane monoculture, due to the negative impact of climate change on plant growth.

(b) Bananas

Banana production is more susceptible to the effects of tropical cyclones and high intensity hurricane events, than to absolute changes in temperature or rainfall. The results showed that a 1% decrease in rainfall is expected to cause an approximate 0.27 % decrease in the growth of banana exports; while a 1% increase in temperature is expected to result in a 5.1 % decrease in the growth of banana exports. Banana production is therefore affected by projected declines in rainfall over time alongside projected increases in temperatures in the next four decades. By 2050, the value of cumulative yield losses (2008 in Dollars) for bananas is expected to be about US$ 61 million, regardless of the scenario (UN, 2011) in the Caribbean.

A study conducted in 2018 (Blake et al., 2018) shows climatic events between 2000 and 2015, such as heavy rainfall, can have a reinforcing effect on an endogenous event such as an outbreak of disease and result in a decrease in banana supply in French west indies (e.g., Guadeloupe). Meanwhile, some events, e.g., droughts, and hurricanes may affect directly the banana plantations (Table 4).

Table 4: Inventory of weather events, which affected banana production and supply in French West Indies (Martinique and Guadeloupe), 2001-2015 (Source: the authors based on FruiTrop, ReeferTrends, Sopisco News, FAO reports).

Region	year	Climate events
French West Indies (Martinique and Guadeloupe)	2001	Drought in Guadeloupe (first half of year, -50% rainfall)
	2004	Hurricane Jean in Guadeloupe (Sep)
	2007	Hurricane Dean in Guadeloupe (Aug, destroys 80% plantations)
	2010	Storm Agatha in Guadeloupe (June 18,000ha). Hurricane Tomas in Guadeloupe (Oct)
	2014	Hurricane Gonzalo in Guadeloupe (Oct, destroys 20% plantations)
	2015	Storm Erika in Guadeloupe (Aug)

Simulating the climate change impact on socio-economic dimensions and needs for adaptation

Despite impact on productivity levels, projections of climate change impact on socio-economic dimensions for 2056–2080 do not highlight significant changes in farming area of sugarcane and pasture. Moreover, farming area for banana exports may almost disappear, while some of the area of bananas cultivated for the local market may slightly rise. However, a potential increase in agricultural land area may occur for market gardening (+9%), pineapple (+15%), orchards (+16%), and yams (+130%).

The overall potential impact of climate change on the current farming systems in the island indicates the chance of inducing significant impact, with detrimental impacts on food security in Guadeloupe if no changes are made to the farming systems (Selbonne et al., 2022). Currently, Guadeloupe is more than 80% dependent on food imports. In line with the objectives of climate smart agriculture (CSA), which are based on agroecology and bioeconomy principles, the best designed scenario shows the potential impact of climate change on production could be reduced by 12.5%.

The climate and agricultural challenges of the French west-indies islands (e.g., Guadeloupe) are associated with adaptation and mitigation, i.e. a reduction of food imports and the resulting carbon footprint. The replacement of imported synthetic fertilizer and pesticides with locally produced biofertilizers and biopesticides, coupled with climate anticipation and adaptation, can increase the resilience of the current farming systems. Thus, the challenges faced by agriculture in the small island states of the Caribbean (e.g., Guadeloupe) could be as follows:

- Adapting agricultural systems to climate change and mitigating its causes and effects.
- An improved combination of economic, social, and environmental performances.
- Increasing the degree of food autonomy of the regions.

These objectives in line with the emerging concept of climate smart agriculture (CSA), which aims to propose an integrated approach to agriculture to meet the challenges of food security, adaptation, and mitigation of climate change (Selbonne et al., 2022). Thus, new ambitious policies targeting farmers' constraints (e.g., CC effects) are required to upscale CSA in the island, developing stakeholder programs to discuss existing issues and corresponding levers for a successful transition of agricultural systems. The co-identification, with policy-makers and stakeholders, of pathways for better-decision-making is an important part of the transition. The agro-ecological transition can be facilitated through several actions such as:

- Teaching and advising farmers to adhere to and pursue the new agricultural policies.
- Setting up networks of farmers to enable them to share their experiences.
- Reducing the use of pesticides and fertilizers.
- Design of a prototype climate-smart agricultural system.
- Developing permaculture, organic agriculture and agroforestry.

7 Web portal for data and information

Over the project runtime, it became obvious that the partners and end users had problems to understand the nature and amount of data available for them, although support was granted by PIK, CMCC and other involved partners. The data availability and description were also a demand from a midterm review. Therefore, PIK volunteered to compile a web portal to visualize and describe the data and methods in maps and graphs and make the available data downloadable in common formats. The following section introduces the portal, explains the main functionality, illustrates some of the outputs and discusses further steps.

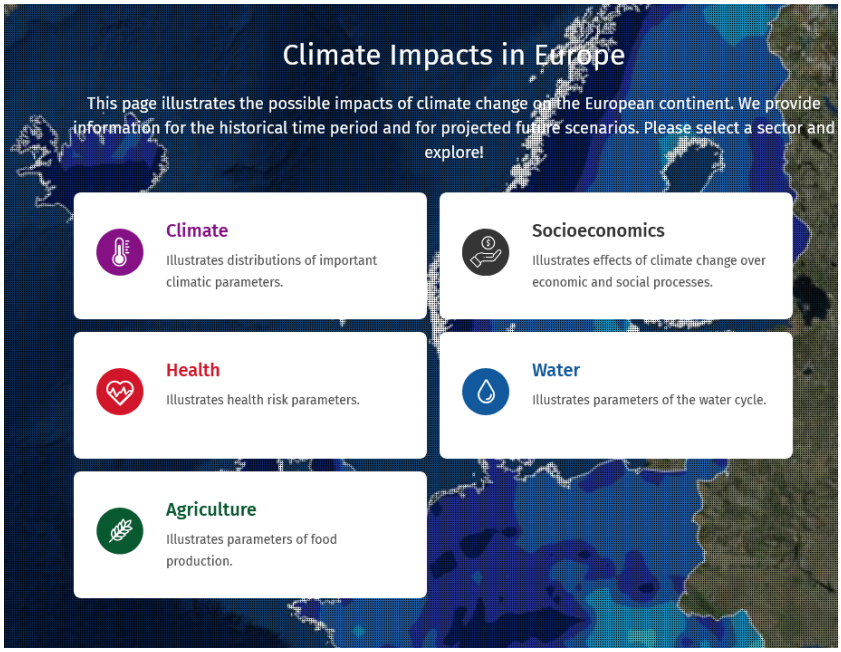

Figure 35: Five sectors are currently considered in the web portal[14].

Currently, data of five sectors are considered in the web portal (Figure 35): Climate, Water, Health, Agriculture and Socio-economics. When choosing one of the sectors, sector specific variables can be selected and analysed. Figure 35 shows the selection box for the different sectors (see also https://kfo.pik-potsdam.de/eur/index_en.html?language_id=en).

Figure 36 gives the window which appears when selecting the climate sector. On the left and when choosing “parameters”, climate variables such as mean, min and max temperature, precipitation and derived variables such as continuous hot days, ice days etc. can be selected. On the left under “settings”, selection of scenarios, seasons and aggregation of the results can be chosen. The scale at the bottom is to select the time period to be shown or the time period chosen for difference maps. It can also be used to provide the results in a movie like feature starting in the historical period and running until end of the century. Help and more information on the specific variable can be found under “more”.

[14] https://kfo.pik-potsdam.de/eur/index_en.html?language_id=en

The tabs on top provide general information about the project and data, explain the usage and data basis, a glossary, provide educational material, one can select different languages and download the selected data. Languages considered up until now are:

- English, German, French, Spanish and Italian.

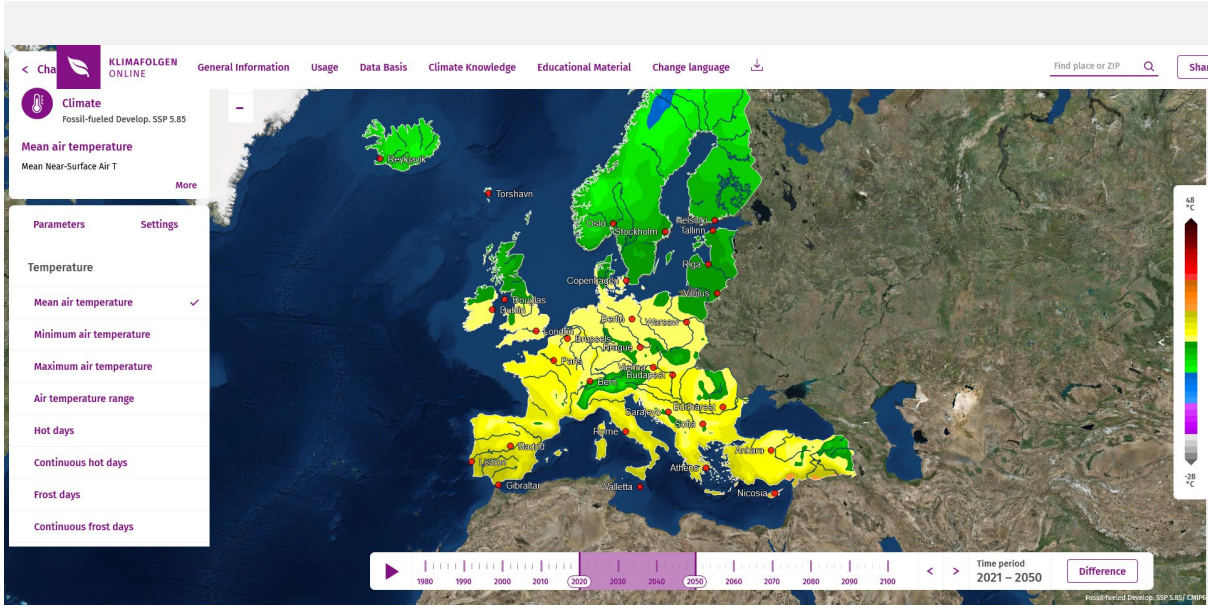

Figure 36: The entry page when selecting the sector climate.

Figure 37 provides a typical result when choosing, in this case, mean temperature development for a specific region, here for entire Europe, and scenario, here SSP5-8.5. The lowest aggregation level for climate is Nuts2.

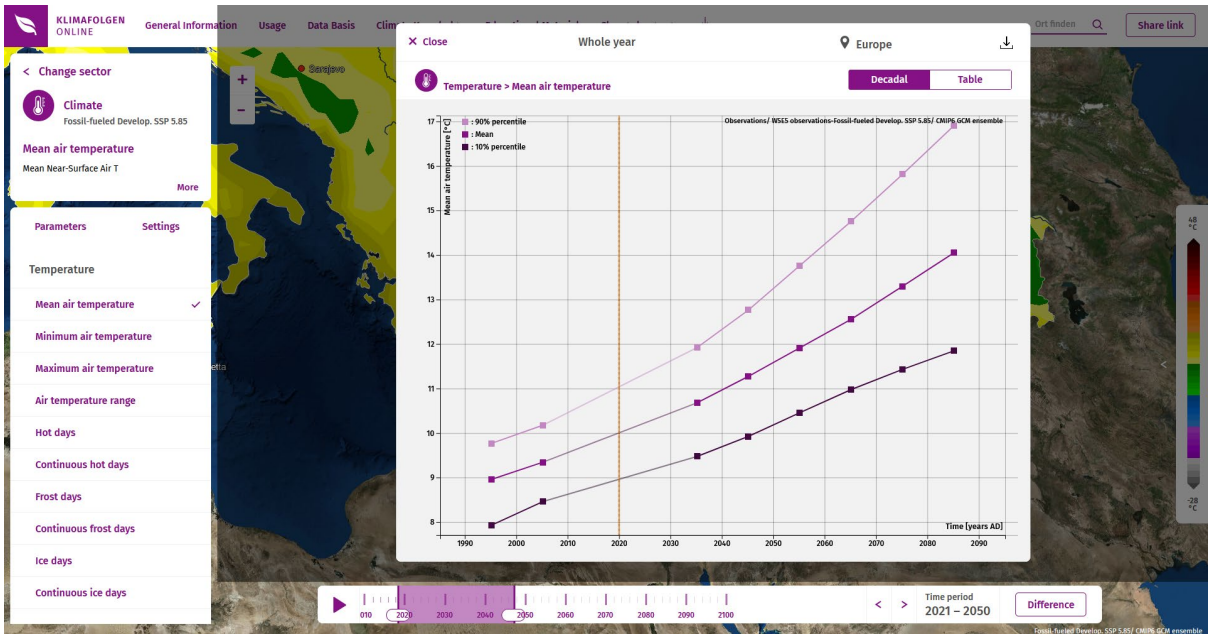

Figure 37: Temperature development for a specific region and SSP scenario.

Download of the selected data can be done in different ways, for example by choosing the “table” button on top of the graph. This way, a summary of the available data for the selected time period is provided (see Figure 38). Another possibility is to download entire time series for a specific region. The data are stored in csv (comma-separated values) format, easily loadable into all popular programming, text and table calculation software.

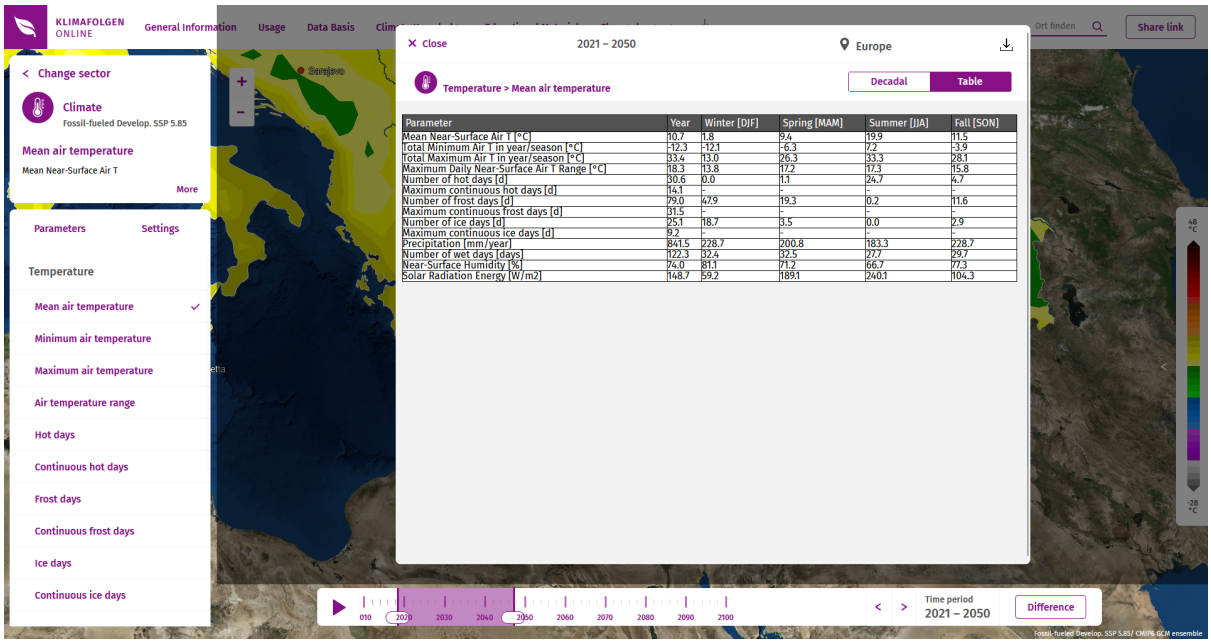

Figure 38: Data summary.

Next steps

The functionality of the portal is already advanced, but it is meant to be a “living portal”, saying that new information and data from the project partners and beyond will be integrated as soon as they are validated. One of the next steps is to include tourism as another sector. Improvement of the functionality upon feedback and correction of coding problems is a constant task.

The coding and maintenance are done at PIK, ensuring uptake of new information and integration into the portal as well as preservation of the portal.

8 Discussion, conclusions and outlook

8.1 Sources of Uncertainty in the Model Results

Water resources management and planning of future water security is subject to multiple uncertainties. As discussed above, some of these are associated with the socio-economic pathways (SSP) that the world can take and the resulting global climate change, modelling the impacts at local scales, the local adaptation and mitigation programs, and many other factors.

Effective use of climate models to support planning and decision-making requires a solid understanding of their limitations and the potential uncertainties in the model outputs. It has been observed that these uncertainties can be considerable (Hattermann et al. 2015 and 2017, Blöschl et al. 2010). This is partly attributed to the inherent limitations of the climate and impact models, as well as to the absence of feedback mechanisms between the hierarchically arranged models, as presented in Figure 3. Additional uncertainty in the model outputs is caused by the inevitable averaging of the climate parameters over large grid cells that eliminate local and micro-climate variations—which are prominent in most landscapes.

In general, mathematical models are only an abstraction of the physical environment. Likewise, the input data for the hydrological models (such as weather, soil, vegetation, and elevation data) are typically subject to uncertainties. It has been observed that the highest regional uncertainty related to the climate models is located at the interface between regions where precipitation increases and regions where precipitation decreases with high certainty. More specifically, this transition zone is located at different places in different climate models. This, of course, has a significant impact on the hydrological output (Hattermann et al. 2017).

In addition, it has not been possible to assign objective probabilities to future greenhouse gas emission scenarios. This is because the socio-economic drivers of these scenarios—which include population size, economic development, future prosperity, lifestyle patterns, technological developments, etc.—are largely unpredictable.

Consequently, to consider the unknow uncertainties regarding the climate impacts, an ensemble of scenarios and GCMs was applied rather than a single scenario or climate model. This approach accounts for different (yet unknown) future atmospheric greenhouse gas concentrations. Likewise, a scenario setup accommodates a comparison of results from different impact models and different input data sets (IPCC 2014) that takes into account the inherent uncertainties of the modelling exercise.

8.2 Conclusions

The results illustrate that climate change is ongoing and the impacts on water resources and on vegetation are visible already now and increase with further global warming. Extremes show the same pattern of stronger trends with increasing temperature. This is so relevant, because critical infrastructure is normally adjusted to protect against events of a certain intensity (or return level), and precautionary measures are challenged by the increasing hazards.

However, the results also illustrate what we gain if we invest consequently into avoiding greenhouse gases: significantly lower consequences for natural resources and the extremes, and from this the environment and the people living in specific regions of Europe will benefit accordingly. Nevertheless, climate change will continue for the time being, and this will initially lead to a further increase in the

impacts. This is why it is also so important to invest in prevention and to test and implement possible adaptation strategies.

An important aspect driving the work in WP2 is the close collaboration with project partners and stakeholders in the demonstrators, for examples the WP3, WP4 and WP5. End-user demands have shaped and will influence future development of the model implementation and of the portal design.

8.3 Outlook

So far, the main exchange with end-users was with the ones of the demonstrators (besides presenting the results in workshops of other projects and conferences). The next period will focus more on the upscaling in interaction with national and European decision makers and stakeholders. Design and development of the portal will be ongoing and integrate new information and data as soon as they are validated by the project partners.

Another focus of the second phase will be on adaptation. This already started with examples in the demonstrators of TransformAr, but will be continued in a more consolidated way, again always in communication with the project partners and outside experts.

9 References

Agreste (2019) 'Mémento de la statistique agricole'. Ministère de l'agriculture, de l'agroalimentaire et de la forêt. Available at: https://agreste.agriculture.gouv.fr/agreste-web/download/publication/publie/MemSta2019/V1_MementoFrance%202019_SITE.pdf.

Argüeso, D. et al. (2011) 'Evaluation of WRF Parameterizations for Climate Studies over Southern Spain Using a Multistep Regionalization', Journal of Climate, 24(21), pp. 5633–5651. Available at: https://doi.org/10.1175/JCLI-D-11-00073.1.

Balkovič, J. et al. (2014) 'Global wheat production potentials and management flexibility under the representative concentration pathways', Global and Planetary Change, 122, pp. 107–121. Available at: https://doi.org/10.1016/j.gloplacha.2014.08.010.

Bastos, A., Ciais, P., et al. (2020) 'Direct and seasonal legacy effects of the 2018 heat wave and drought on European ecosystem productivity', Science Advances, 6(24), p. eaba2724. Available at: https://doi.org/10.1126/sciadv.aba2724.

Bastos, A., Fu, Z., et al. (2020) 'Impacts of extreme summers on European ecosystems: a comparative analysis of 2003, 2010 and 2018', Philosophical Transactions of the Royal Society B: Biological Sciences, 375(1810), p. 20190507. Available at: https://doi.org/10.1098/rstb.2019.0507.

Bastos, A. et al. (2021) 'Vulnerability of European ecosystems to two compound dry and hot summers in 2018 and 2019', Earth System Dynamics, 12(4), pp. 1015–1035. Available at: https://doi.org/10.5194/esd-12-1015-2021.

Blake, D. et al. (2018) 'Can Global Climate Change affect Prices in the World Banana Market?' Available at: https://doi.org/10.22004/AG.ECON.309949.

Chopin, P. and Sierra, J. (2019) 'Reduced tillage and organic amendments can offset the negative impact of climate change on soil carbon: A regional modelling study in the Caribbean', Soil and Tillage Research, 192, pp. 113–120. Available at: https://doi.org/10.1016/j.still.2019.05.009.

Christensen, J.H. and Christensen, O.B. (2007) 'A summary of the PRUDENCE model projections of changes in European climate by the end of this century', Climatic Change, 81(S1), pp. 7–30. Available at: https://doi.org/10.1007/s10584-006-9210-7.

Coppola, E. et al. (2021) 'Assessment of the European Climate Projections as Simulated by the Large EURO-CORDEX Regional and Global Climate Model Ensemble', Journal of Geophysical Research: Atmospheres, 126(4), p. e2019JD032356. Available at: https://doi.org/10.1029/2019JD032356.

Cornes, R.C. et al. (2018) 'An Ensemble Version of the E-OBS Temperature and Precipitation Data Sets', Journal of Geophysical Research: Atmospheres, 123(17), pp. 9391–9409. Available at: https://doi.org/10.1029/2017JD028200.

Custodio, E. (2021) 'Ethical and Moral Issues Relative to Groundwater', in M. Abrunhosa et al. (eds) Advances in Geoethics and Groundwater Management : Theory and Practice for a Sustainable Development. Cham: Springer International Publishing (Advances in Science, Technology & Innovation), pp. 9–12. Available at: https://doi.org/10.1007/978-3-030-59320-9_2.

Dai, Y. et al. (2014) 'Regional flood dynamics in a bifurcating mega delta simulated in a global river model', Geophysical Research Letters, 41, pp. 3127–3135.

EEA (2017) Trends and projections in Europe 2017. Available at: https://www.eea.europa.eu/themes/climate/trends-and-projections-in-europe/trends-and-projections-in-europe-2017.

FAO (2007) The State of Food and Agriculture: Paying Farmers for Environmental Services. Agricultural Development Economics Division (ESA). Rome: FAO. Available at: www.fao.org/docrep/010/a1200e/a1200e00.htm.

Frieler, K. et al. (2024) 'Scenario setup and forcing data for impact model evaluation and impact attribution within the third round of the Inter-Sectoral Model Intercomparison Project (ISIMIP3a)', Geoscientific Model Development, 17(1), pp. 1–51. Available at: https://doi.org/10.5194/gmd-17-1-2024.

Gobiet, A., Suklitsch, M. and Heinrich, G. (2015) 'The effect of empirical-statistical correction of intensity-dependent model errors on the temperature climate change signal', Hydrology and Earth System Sciences, 19(10), pp. 4055–4066. Available at: https://doi.org/10.5194/hess-19-4055-2015.

Haas, E. et al. (2013) 'LandscapeDNDC: a process model for simulation of biosphere–atmosphere–hydrosphere exchange processes at site and regional scale', Landscape Ecology, 28(4), pp. 615–636. Available at: https://doi.org/10.1007/s10980-012-9772-x.

Hattermann, F. et al. (2005) 'Runoff simulations on the macroscale with the ecohydrological model SWIM in the Elbe catchment - validation and uncertainty analysis', Hydrological Processes, 19(3), pp. 693–714.

Hattermann, F.F. (2011) 'Expertise 2 "Klimawandel und Hydrologie in der Region Havelland-Fläming"', Klimawandel in der Region Havelland-Fläming. Edited by A. Lüttger et al. Potsdam: Potsdam-Institut für Klimafolgenforschung (PIK-Report ; 121).

Hattermann, F.F. et al. (2014) 'Modelling flood damages under climate change conditions - a case study for Germany', Natural Hazards and Earth System Sciences, 14(12), pp. 3151–3168. Available at: https://doi.org/10.5194/nhess-14-3151-2014.

Hattermann, F.F. et al. (2017) 'Cross-scale intercomparison of climate change impacts simulated by regional and global hydrological models in eleven large river basins', Climatic Change, 141(3), pp. 561–576. Available at: https://doi.org/10.1007/s10584-016-1829-4.

Hattermann, F.F. et al. (2018) 'Simulation of flood hazard and risk in the Danube basin with the Future Danube Model', Climate Services, 12, pp. 14–26. Available at: https://doi.org/10.1016/j.cliser.2018.07.001.

Hattermann, F.F., Huang, S. and Koch, H. (2015) 'Climate change impacts on hydrology and water resources', Meteorologische Zeitschrift, 24(2), pp. 201–211. Available at: https://doi.org/10.1127/metz/2014/0575.

Haylock, M.R. et al. (2008) 'A European daily high-resolution gridded data set of surface temperature and precipitation for 1950–2006', Journal of Geophysical Research: Atmospheres, 113(D20), p. 2008JD010201. Available at: https://doi.org/10.1029/2008JD010201.

Hoffmann, P. and Spekat, A. (2021) 'Identification of possible dynamical drivers for long-term changes in temperature and rainfall patterns over Europe', Theoretical and Applied Climatology, 143(1–2), pp. 177–191. Available at: https://doi.org/10.1007/s00704-020-03373-3.

Iizumi, T. et al. (2017) 'Responses of crop yield growth to global temperature and socioeconomic changes', Scientific Reports, 7(1), p. 7800. Available at: https://doi.org/10.1038/s41598-017-08214-4.

INNOVA (2019) 'Urban Climate Adaptation-Guadeloupe, Martinique, Kiel Bay, and Valencia'. 4th INNOVA e-zine.

IPCC (2021) Climate Change 2021: The Physical Science Basis. Contribution of Working Group I to the SixthAssessment Report of the Intergovernmental Panel on Climate Change. Cambridge University Press.: IPCC. Available at: https://www.ipcc.ch/report/ar6/wg1/#FullReport.

Jacob, D. et al. (2014) 'EURO-CORDEX: new high-resolution climate change projections for European impact research', Regional Environmental Change, 14(2), pp. 563–578. Available at: https://doi.org/10.1007/s10113-013-0499-2.

Kim, K. and Wu, Q. (1999) 'A Comparison Study of EOF Techniques: Analysis of Nonstationary Data with Periodic Statistics', Journal of Climate, 12(1), pp. 185–199. Available at: https://doi.org/10.1175/1520-0442(1999)012<0185:ACSOET>2.0.CO;2.

Kjellstrom, T. et al. (2009) 'The Direct Impact of Climate Change on Regional Labor Productivity', Archives of Environmental & Occupational Health, 64(4), pp. 217–227. Available at: https://doi.org/10.1080/19338240903352776.

Kjellstrom, T., Holmer, I. and Lemke, B. (2009) 'Workplace heat stress, health and productivity – an increasing challenge for low and middle-income countries during climate change', Global Health Action, 2(1), p. 2047. Available at: https://doi.org/10.3402/gha.v2i0.2047.

Krysanova, V. et al. (2015) 'Modelling climate and land-use change impacts with SWIM: lessons learnt from multiple applications', Hydrological Sciences Journal, 60(4), pp. 606–635. Available at: https://doi.org/10.1080/02626667.2014.925560.

Krzysztofowicz, R. (1997) 'Transformation and normalization of variates with specified distributions', Journal of Hydrology, 197(1–4), pp. 286–292. Available at: https://doi.org/10.1016/S0022-1694(96)03276-3.

Lange, S. (2018) 'Bias correction of surface downwelling longwave and shortwave radiation for the EWEMBI dataset', Earth System Dynamics, 9(2), pp. 627–645. Available at: https://doi.org/10.5194/esd-9-627-2018.

Lange, S. (2019) 'Trend-preserving bias adjustment and statistical downscaling with ISIMIP3BASD (v1.0)', Geoscientific Model Development, 12(7), pp. 3055–3070. Available at: https://doi.org/10.5194/gmd-12-3055-2019.

Lange, S. et al. (2021) 'WFDE5 over land merged with ERA5 over the ocean (W5E5 v2.0)'. ISIMIP Repository. Available at: https://doi.org/10.48364/ISIMIP.342217.

Lian, X. et al. (2020) 'Summer soil drying exacerbated by earlier spring greening of northern vegetation', Science Advances, 6(1), p. eaax0255. Available at: https://doi.org/10.1126/sciadv.aax0255.

Liljegren, J.C. et al. (2008) 'Modeling the Wet Bulb Globe Temperature Using Standard Meteorological Measurements', Journal of Occupational and Environmental Hygiene, 5(10), pp. 645–655. Available at: https://doi.org/10.1080/15459620802310770.

Lindeskog, M. et al. (2013) 'Implications of accounting for land use in simulations of ecosystem carbon cycling in Africa', Earth System Dynamics, 4(2), pp. 385–407. Available at: https://doi.org/10.5194/esd-4-385-2013.

Liu, W. et al. (2016) 'Global investigation of impacts of PET methods on simulating crop-water relations for maize', Agricultural and Forest Meteorology, 221, pp. 164–175. Available at: https://doi.org/10.1016/j.agrformet.2016.02.017.

Mauser, W. et al. (2015) 'Global biomass production potentials exceed expected future demand without the need for cropland expansion', Nature Communications, 6(1), p. 8946. Available at: https://doi.org/10.1038/ncomms9946.

Moriasi, D.N. et al. (2015) Hydrologic and Water Quality Models: Performance Measures and Evaluation Criteria. American Society of Agricultural and Biological Engineers (ASABE), St. Joseph, 1763-1785.

https://doi.org/10.13031/trans.58.10715

NOAA (2023) 2022 NOAA Science Report. Silver Spring, Maryland. Available at: https://research.noaa.gov/wp-content/uploads/2023/04/FINAL_2022-NOAA-Science-Report.pdf.

OECS (2021) 'Territorial analysis: Resilience to climate change at a glance: Guadeloupe Region.'

Okada, M. et al. (2018) 'Varying Benefits of Irrigation Expansion for Crop Production Under a Changing Climate and Competitive Water Use Among Crops', Earth's Future, 6(9), pp. 1207–1220. Available at: https://doi.org/10.1029/2017EF000763.

O'Neill, B.C. et al. (2016) 'The Scenario Model Intercomparison Project (ScenarioMIP) for CMIP6', Geoscientific Model Development, 9(9), pp. 3461–3482. Available at: https://doi.org/10.5194/gmd-9-3461-2016.

OREC (2016) 'Profil de vulnérabilité de la guadeloupe au changement climatique'. Observatoire Régional de l'Energie et du Climat.

Pachauri, R.K., Mayer, L., and Intergovernmental Panel on Climate Change (eds) (2015) Climate change 2014: synthesis report. Geneva, Switzerland: Intergovernmental Panel on Climate Change.

Politi, N. et al. (2021) 'High-resolution dynamical downscaling of ERA-Interim temperature and precipitation using WRF model for Greece', Climate Dynamics, 57(3–4), pp. 799–825. Available at: https://doi.org/10.1007/s00382-021-05741-9.

Prein, A.F. et al. (2016) 'Precipitation in the EURO-CORDEX $$0.11^{\circ }$$ 0 . 11 ∘ and $$0.44^{\circ }$$ 0 . 44 ∘ simulations: high resolution, high benefits?', Climate Dynamics, 46(1–2), pp. 383–412. Available at: https://doi.org/10.1007/s00382-015-2589-y.

Saint Ville, A.S., Hickey, G.M. and Phillip, L.E. (2015) 'Addressing food and nutrition insecurity in the Caribbean through domestic smallholder farming system innovation', Regional Environmental Change, 15(7), pp. 1325–1339. Available at: https://doi.org/10.1007/s10113-015-0770-9.

Selbonne, S. et al. (2022) 'Designing scenarios for upscaling climate-smart agriculture on a small tropical island', Agricultural Systems, 199, p. 103408. Available at: https://doi.org/10.1016/j.agsy.2022.103408.

Steinhausen, M. et al. (2022) 'Drivers of future fluvial flood risk change for residential buildings in Europe', Global Environmental Change (76).

Soares, P.M.M. et al. (2017) 'Future precipitation in Portugal: high-resolution projections using WRF model and EURO-CORDEX multi-model ensembles', Climate Dynamics, 49(7–8), pp. 2503–2530. Available at: https://doi.org/10.1007/s00382-016-3455-2.

Sparks, N.J. et al. (2018) 'IMAGE: a multivariate multi-site stochastic weather generator for European weather and climate', Stochastic Environmental Research and Risk Assessment, 32(3), pp. 771–784. Available at: https://doi.org/10.1007/s00477-017-1433-9.

Storch, H. von and Swiers, F.W. (1999) Statistical analysis in climate research. Cambridge: Cambridge university press.

UN (2011) The Economics of Climate Change in the Caribbean-Summary Report. United nations economic commission for latin america and the caribbean. Port-of-Spain, Trinidad and Tobago: Subregional Headquarters for the Caribbean.

Von Bloh, W. et al. (2018) 'Implementing the nitrogen cycle into the dynamic global vegetation, hydrology, and crop growth model LPJmL (version 5.0)', Geoscientific Model Development, 11(7), pp. 2789–2812. Available at: https://doi.org/10.5194/gmd-11-2789-2018.

Webber, H. et al. (2015) 'Climate change impacts on European crop yields: Do we need to consider nitrogen limitation?', European Journal of Agronomy, 71, pp. 123–134. Available at: https://doi.org/10.1016/j.eja.2015.09.002.

Wilcke, R.A.I., Mendlik, T. and Gobiet, A. (2013) 'Multi-variable error correction of regional climate models', Climatic Change, 120(4), pp. 871–887. Available at: https://doi.org/10.1007/s10584-013-0845-x.

Wright, S.J. (2015) 'Coordinate descent algorithms', Mathematical Programming, 151(1), pp. 3–34. Available at: https://doi.org/10.1007/s10107-015-0892-3.

Yamazaki, D. et al. (2014) 'Regional flood dynamics in a bifurcating mega delta simulated in a global river model: SIMULATION OF RIVER MEGA DELTA FLOWS', Geophysical Research Letters, 41(9), pp. 3127–3135. Available at: https://doi.org/10.1002/2014GL059744.

Zou, H. and Hastie, T. (2005) 'Regularization and Variable Selection Via the Elastic Net', Journal of the Royal Statistical Society Series B: Statistical Methodology, 67(2), pp. 301–320. Available at: https://doi.org/10.1111/j.1467-9868.2005.00503.x.

10 Annex

10.1 SWIM: Overview of the Model Components

10.1.1 Input data for the model setup

To set-up the model, various information in form of digital maps is necessary, which, in their combination, reflect the spatial heterogeneity of the landscape in the basin (Figure A1). The sub-catchments can be calculated from a digital elevation model (DEM) or taken from official maps of the federal states. For the model set-up, we applied the MERIT data to delineate the sub-basins and to calculate flow directions and gradients. This resulted in a total of 3303 sub-basins and 794 for the river 28 river regions in Europe considered. The most important turnover zone of the water and material flows is the soil, whereby the HWSD-FAO soil information was used (1000 m resolution, status of data: 2019). The land use data used is based on Copernicus Global Land Service information (resolution 100 m, status of data 2019). The latter have been reclassified to build the 15 land use classes considered in SWIM. Figure A1 illustrates the overlay of different layers of information, and Table A1 lists the climate, hydrological and spatial data applied.

Table A1: Spatial, climate and hydrological input data applied in the study.

Input spatial information	
DEM	EU DEM, v 1.1[15] (~100 m)
Land use	Copernicus Global Land Service[16]: Land cover 100 m (2019)
Soils	European soil data map[17] (1000 m)
Input time series	
Climate	W5E5 (observation) and ISIMIP3b (scenario), resolution: 0.5°
Hydrological	Global Runoff Data Centre

[15] https://sdi.eea.europa.eu/catalogue/srv/api/records/3473589f-0854-4601-919e-2e7dd172ff50

[16] https://land.copernicus.eu/en

[17] https://esdac.jrc.ec.europa.eu/resource-type/european-soil-database-maps

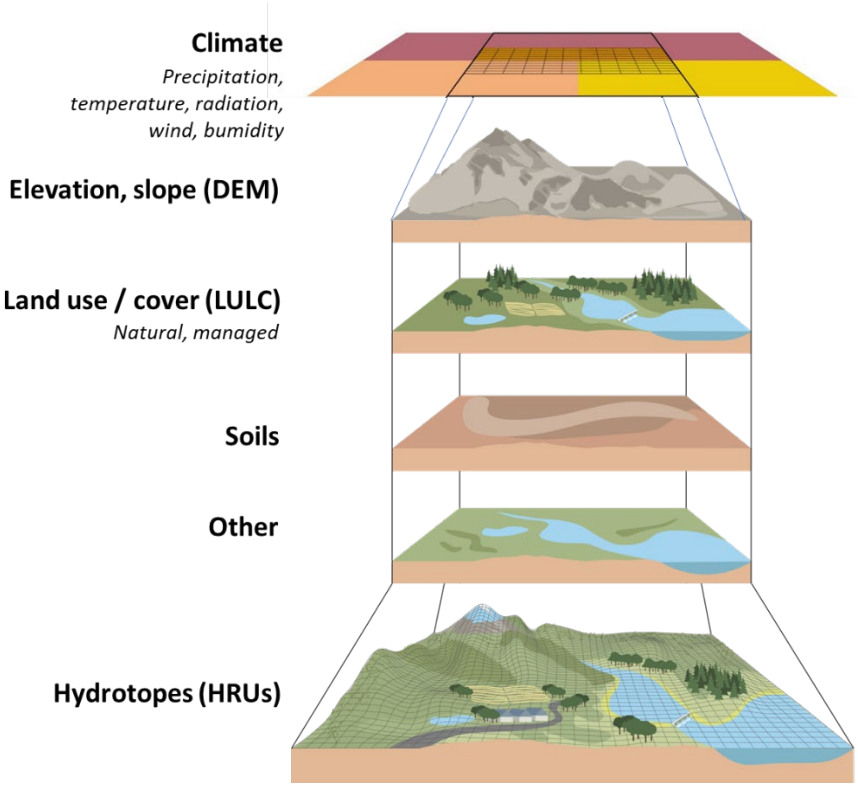

Figure A1: Spatial, climate and hydrological input data applied in the study.

Climate data applied to drive the model are precipitation, minimum, maximum and average temperature, radiation and humidity. They are based on W5E5 re-analysis data in the historical and ISIMIP3b in the scenario period with a resolution of 0.5°.

The maps applied are presented in Figure A2.

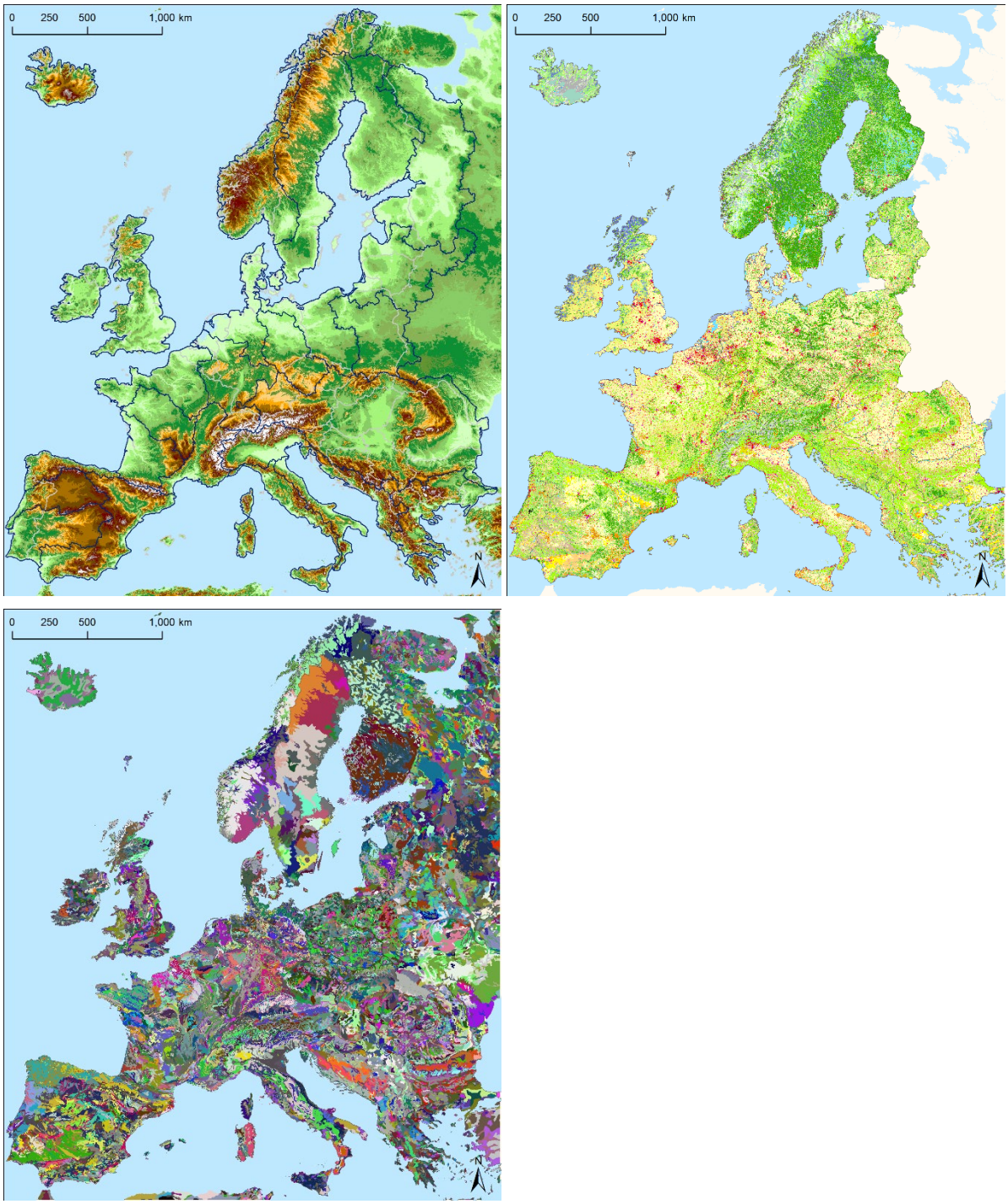

Figure A2: Digital Elevation Map (top left), land use (top right) and European soil map (bottom) applied in the European model set-up (more information in Table A1).

10.1.2 Hydrological Processes

The main water flows and parameters needed to model the hydrological processes are summarized in Figure A3.

Snow melt In the simplest version, the snow melt component is a degree-day equation. This can be done applying to levels of spatial disaggregation: in a lumped version for entire sub-basins or considering the elevation in form of height bands from valley bottom up the slopes to the crest of the catchment. Melted snow is then treated in the same way as rainfall for further estimation of runoff and percolation. In the more complex version, the temperature and snow melt vary with height along the slopes of the subbasins.

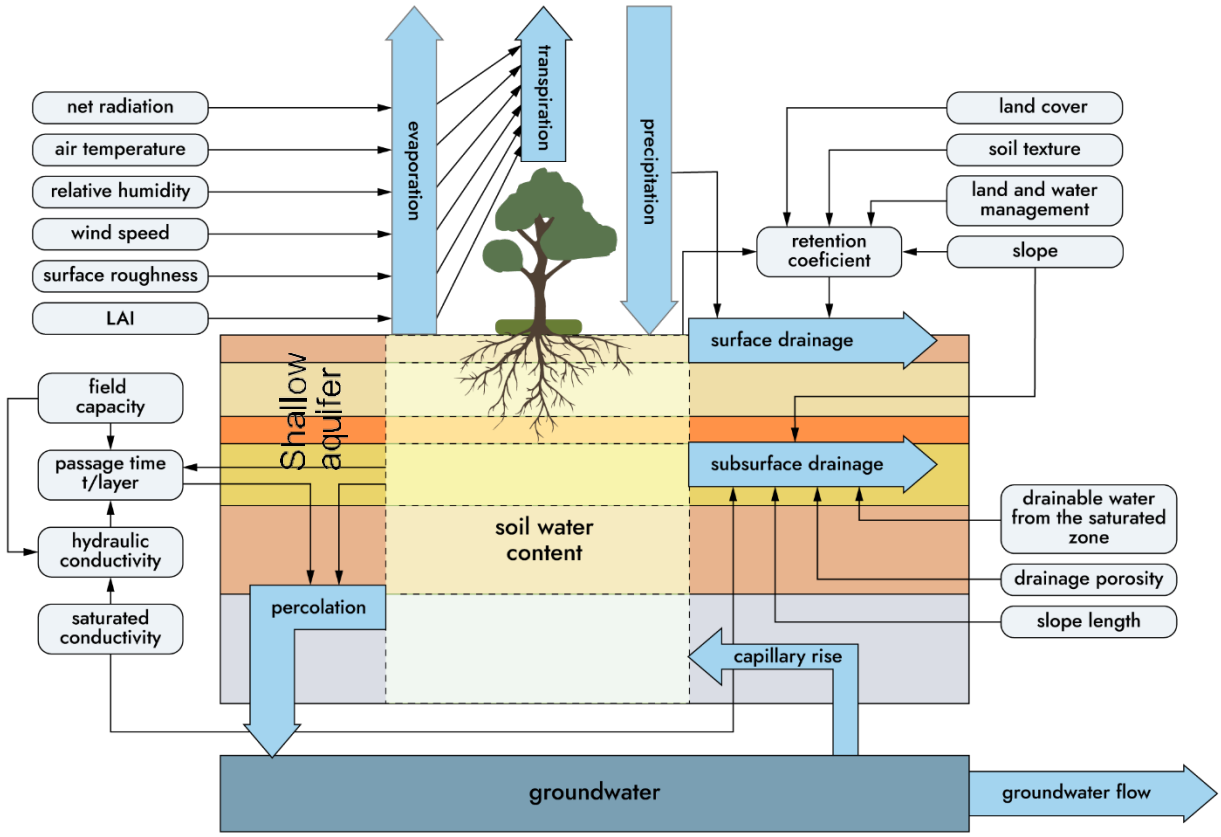

Figure A3: Flow chart of the SWIM model, integrating hydrological processes, crop/vegetation growth, and nutrient dynamics in SWIM.

Surface runoff The runoff volume is estimated using a modification of the SCS curve number method (Arnold et al, 1990a). Surface runoff is predicted as a nonlinear function of precipitation and a retention coefficient. The latter depends on soil water content, land use, soil type, and management. The curve number and the retention coefficient vary non- linearly from dry conditions at wilting point to wet conditions at field capacity and approach 100 and 0 respectively at saturation. The modification essentially reduces the empirism of the original curve number method. The reliability of the method has been proven by multiple validations of SWAT and SWIM in mesoscale basins. Nevertheless, there is a possibility to exclude the dependence of the retention coefficient on land

use and soil, leaving the dependence on soil water content only, and assuming the same interval for all types of land use and soils.

Percolation The same storage routing technique as in SWAT is used to simulate water flow through soil layers in the root zone. Downward flow occurs when field capacity of the soil layer is exceeded, and as long as the layer below is not saturated. The flow rate is governed by the saturated hydraulic conductivity of the soil layer. Once water percolates below the root zone, it becomes groundwater. Since the one-day time interval is relatively large for soil water routing, the inflow is divided into 4 mm slugs in order to take into account the flow rate's dependence on soil water content. If the soil temperature in a layer is below 0°C, no percolation occurs from that layer. The soil temperature is estimated for each soil layer using the air temperature as a driver (Arnold *et al.*, 1990b).

Lateral subsurface flow Lateral subsurface flow is calculated simultaneously with percolation. The kinematic storage model developed by Sloan *et al.* (1983) is used to estimate the subsurface flow. The approach is based on the mass continuity equation in the finite difference form with the entire soil profile as the control volume. To account for multiple layers, the model is applied to each soil layer independently starting at the upper layer to allow for percolation from one soil layer to the next and percolation from the bottom soil layer past the soil profile (as recharge to the shallow aquifer).

Evapotranspiration Different methods can be applied to calculate potential evapotranspiration. In the current study, potential evapotranspiration is estimated using the Priestley-Taylor method (1972) that requires solar radiation and air temperature as input. It is possible to use the Penman-Monteith method (Monteith, 1965) instead if wind speed and relative air humidity data can be provided in addition. The actual evapotranspiration is estimated following the Ritchie (1972) concept, separately for soil and plants. Actual soil evaporation is computed in two stages. It is equal to the potential soil evaporation predicted by means of an exponential function of leaf area index (Richardson and Ritchie, 1973) until the accumulated soil evaporation exceeds the upper limit of 6 mm. After that stage two begins. The actual soil evaporation is reduced and estimated as a function of the number of days since stage two began. Plant transpiration is simulated as a linear function of potential evapotranspiration and leaf area index. When soil water is limited, plant transpiration is reduced, taking into account the root depth.

Groundwater flow The groundwater model component is the same as in SWAT (see Arnold *et al.*, 1993). The percolation from the soil profile is assumed to recharge the shallow aquifer. Return flow from the shallow aquifer contributes directly to the streamflow. The equation for return flow was derived from Smedema and Rycroft (1983), assuming that the variation in return flow is linearly related to the rate of change of the water table height. In a finite difference form, the return flow is a nonlinear function of ground water recharge and the reaction factor RF, the latter being a direct index of the intensity with which the groundwater outflow responds to changes in recharge. The reaction factor can be estimated for gaged sub-basins using the base flow recession curve.

10.1.3 Crop / Vegetation Growth

The crop model in SWIM and SWAT is a simplification of the EPIC crop model (Williams *et al.*, 1984). The SWIM model uses a concept of phenological crop development based on

- daily accumulated heat units;
- Monteith's approach (1977) for potential biomass;
- water, temperature, and nutrients stress factors; and

- harvest index for partitioning grain yield.

However, the more detailed approach implemented in EPIC for the root growth and nutrient cycling is not included in order to maintain a similar level of complexity of all submodels and to keep control on the model performance.

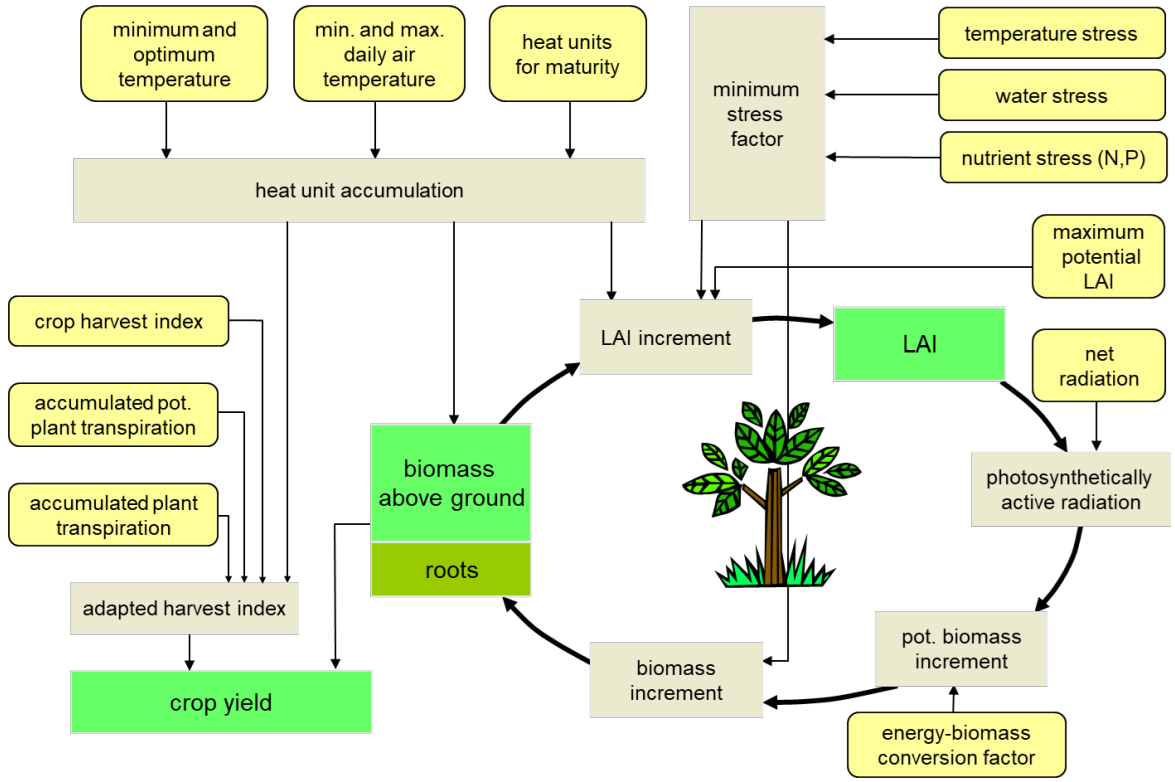

Figure A4: The vegetation module in SWIM

A single model is used for simulating all the crops and natural vegetation included in the crop database attached to the model (Figure 4A). Annual crops grow from planting date to harvest date or until the accumulated heat units reach the potential heat units for the crop. Perennial crops maintain their root systems throughout the year, although the plants may become dormant after frost.

Phenological development of the crop is based on daily heat unit accumulation. Interception of photosynthetic active radiation is estimated with Beer's law equation (Monsi and Saeki, 1953) as a function of solar radiation and leaf area index. The potential increase in biomass is the product of absorbed PAR and a specific plant parameter for converting energy into biomass.

The potential biomass is adjusted daily if one of the four plant stress factors (water, temperature, nitrogen, and phosphorus) is less than 1.0 using the product of a minimum stress factor and the potential biomass. The water stress factor is defined as the ratio of actual to potential plant transpiration. The temperature stress factor is computed as a function of daily average temperature, optimal and base temperatures for plant growth. The N and P stress factors are based on the ratio of accumulated N and P to the optimal values.

The fraction of daily biomass growth partitioned to roots is estimated to range linearly between two fractions specified for each vegetation type - 0.4 at emergence to 0.2 at maturity. Root depth increases as a linear function of heat units and potential root depth. Leaf area index is simulated as a nonlinear function of accumulated heat units and crop development stages. Crop yield is estimated using the harvest index, which increases as a nonlinear function of heat units from zero at planting to the optimal value at maturity. The harvest index is affected by water stress in the second half of the growing period.

10.1.4 Nutrient Dynamics

Nitrogen mineralisation The nitrogen mineralisation model is a modification of the PAPRAN mineralisation model (Seligman and van Keulen, 1981). Organic nitrogen associated with humus is divided into two pools: active or readily mineralisable organic nitrogen and stable organic nitrogen. The model considers two sources of mineralisation: a) fresh organic nitrogen pool, associated with crop residue, and b) the active organic nitrogen pool, associated with the soil humus. Organic N flow between the active and stable organic nitrogen pools is governed by the equilibrium equation. Mineralisation of fresh organic nitrogen is a function of the C:N ratio, C:P ratio, soil temperature, and soil water content. The N mineralisation flow from residue is distributed between the mineral nitrogen (80%) and active organic nitrogen (20%) pools. Mineralisation of the active organic nitrogen pool depends on soil temperature and water content.

Phosphorus mineralization The phosphorus mineralisation model is structurally similar to the nitrogen mineralisation model. To maintain phosphorus balance at the end of a day, humus mineralisation is subtracted from the organic phosphorus pool and added to the mineral phosphorus pool, and residue mineralisation is distributed between the organic phosphorus pool (20%) and the labile phosphorus (80%).

Sorption / adsorption of phosphorus Mineral phosphorus is distributed between three pools: labile phosphorus, active mineral phosphorus, and stabile mineral phosphorus. Mineral phosphorus flow between the active and stable mineral pools is governed by the equilibrium equation, assuming that the stable mineral pool is four times larger. Mineral phosphorus flow between the active and labile mineral pools is governed by the equilibrium equation as well, assuming equal distribution.

Denitrification Denitrification, as one of the microbial processes, is a function of temperature and water content. The denitrification occurs only in the conditions of oxygen deficit, which usually takes place when soil is wet. The denitrification rate is estimated as a function of soil water content, soil temperature, organic matter, a coefficient of soil wetness, and mineral nitrogen content. The soil water factor is an exponential function of soil moisture with an increasing trend when soil becomes wet.

Crop uptake of nutrients Crop uptake of nitrogen and phosphorus is estimated using a supply and demand approach. Six parameters are specified for every crop in the crop database, which describe: BN_1 and BP_1 - normal fraction of nitrogen and phosphorus in plant biomass excluding seed at emergence, BN_2 and BP_2 – at 0.5 maturity, and BN_3 and BP_3 - at maturity. Then the optimal crop N and P concentrations are calculated as functions of growth stage. The daily crop demand of nutrients is estimated as the product of biomass growth and optimal concentration in the plants. Actual nitrogen and phosphorus uptake is the minimum of supply and demand. The crop is allowed to take nutrients from any soil layer that has roots. Uptake starts at the upper layer and proceeds downward until the daily demand is met or until all nutrient content has been depleted.

Soluble nutrient loss in surface water and groundwater The amount of NO_3-N and soluble P in surface runoff is estimated considering the top soil layer only. Amounts of NO_3- N and soluble P in surface runoff, lateral subsurface flow and percolation are estimated as the products of the volume of water and the average concentration. Retention factor is considered through transmission losses. Because phosphorus is mostly associated with the sediment phase, the soluble phosphorus loss is estimated as a function of surface runoff and the concentration of labile phosphorus in the top soil layer.

10.1.5 Erosion

Sediment yield is calculated for each sub-basin with the Modified Universal Soil Loss Equation (MUSLE, Williams and Berndt, 1977), almost the same as in SWAT. The equation for sediment yield includes the runoff factor, the soil erodibility factor, the crop management factor, the erosion control practice factor, and the slope length and steepness factor. The only difference from SWAT is that the surface runoff, the soil erodibility factor and the crop management factor are estimated for every hydrotope, and then averaged for the sub-basin (weighted areal average).

Estimation of the runoff factor requires the characteristics of rainfall intensity as described in Arnold *et al.*, 1990. To estimate the daily rainfall energy in the absence of time- distributed rainfall, the assumption about exponential distribution of the rainfall rate is made. This stochastic element is included to allow more realistic representation of peak runoff rates, given only daily rainfall and monthly rainfall intensity. This allows a simple substitution of rainfall rates into the equation. The fraction of rainfall that occurs during 0.5 hours is simulated stochastically, taking into account average monthly rainfall intensity for the area. Soil erodibility factor can be estimated from the texture of the upper soil layer. The slope length and steepness factor are estimated based on the Digital Elevation Model of a watershed by SWIM/GRASS interface for every sub-basin.

10.1.6 River Routing

The Muskingum flow routing method (Maidment, 1993) is used in SWIM. The Muskingum equation is derived from the finite difference form of the continuity equation and the variable discharge storage equation. The outflow rate for the reach is estimated using a requrrent equation with two parameters. They are the storage time constant for the reach, KST, and a dimensionless weighting factor, X. In physical terms, the parameter KST corresponds to an average reach travel time, and X indicates the relative importance of the inflow and outflow in determining the storage in the reach.

The sediment routing model consists of two components operating simultaneously – deposition and degradation in the streams. The approach is based on the estimation of the stream velocity in the channel as a function of the peak flow rate, the flow depth, and the average channel width. The sediment delivery ratio is estimated using a power function (power 1 to 1.5) of the stream velocity. If the sediment delivery ratio is less than 1, the deposition occurs in the stream, and degradation is zero. Otherwise, degradation is estimated as a function of the sediment delivery ratio, the channel K factor (or the effective hydraulic conductivity of the channel alluvium), and the channel C factor.

Nitrate nitrogen and soluble phosphorus are considered in the model as conservative materials for the duration of an individual runoff event (Williams, 1980). Thus, they are routed by adding contributions from all sub-basins to determine the basin load.

10.1.7 Reservoir module

In order to account for existing or planned large dams and to simulate the impacts of reservoir operation on discharge the reservoir module (Koch et al., 2013) was developed for SWIM. The reservoir module implements three management options (in the following the term discharge is used to describe the quantity of water released by a reservoir, other denominations not used here are release or outflow):

1) variable daily minimum discharge to meet downstream targets, e.g. environmental flow under consideration of maximum and minimum water levels in the reservoir;

2) daily discharge based on electricity to be generated by a hydropower plant at the reservoir (the discharge to generate the required electricity is calculated depending on the water level);

3) daily discharge depending on water level (rising/falling discharge with increased/lowered water level, depending on the objective of reservoir management).

In the present version of the reservoir module the flood protection storage, the life (or active) storage and the dead storage are considered (see Figure A5).

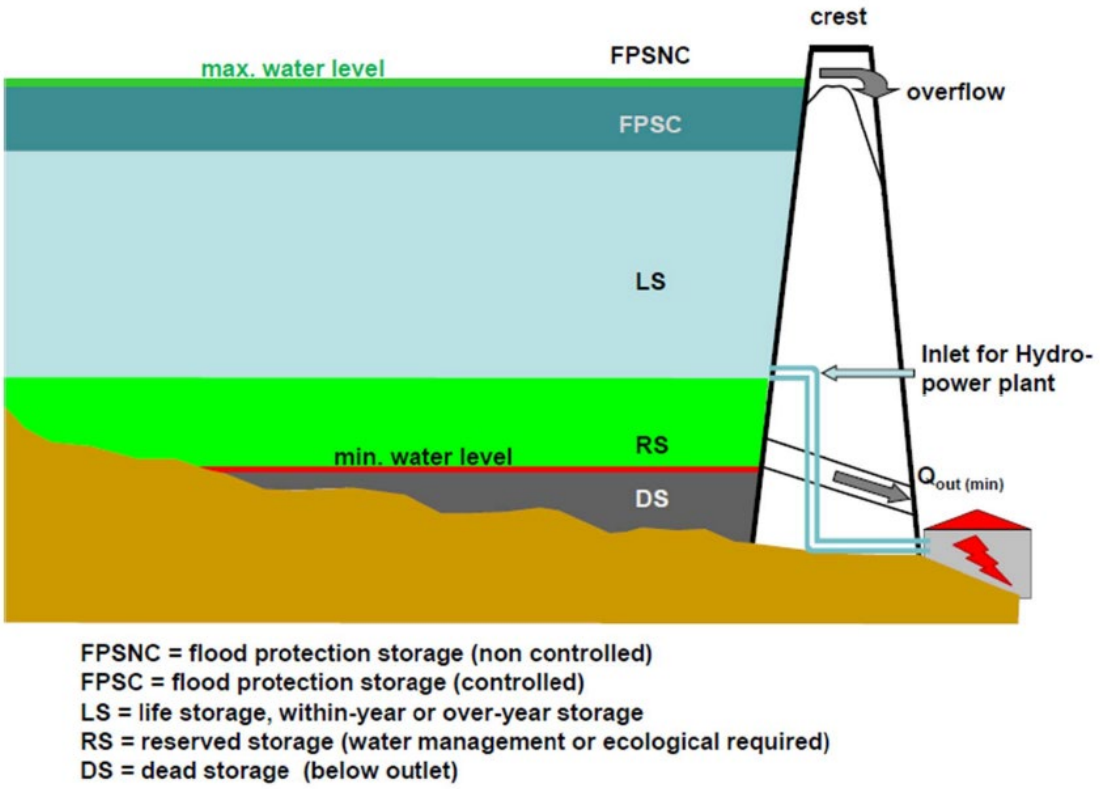

Figure A5: The reservoir module in SWIM.

The reservoir module is called by the SWIM model during the routing procedure. If the routing routine reaches a reservoir-sub-basin, the reservoir routine is called instead of the “normal” sub-basin routine and the simulation is carried out according to the management options set. After the simulation of the reservoir the outflow is routed into the downstream sub-basin.

10.1.8 Management options

1) Variable daily minimum discharge

The simulation considers minimum flows downstream under consideration of maximum and minimum water levels, respectively volumes, in the reservoir. The term 'minimum flows' used here includes ecological and/or human (water withdrawals, navigation etc.) requirements downstream of the dam.

2) Daily release based on electricity yield

The release to generate the required electricity yield is calculated depending on the present water level (=> head).

3) Daily release depending on water level

The simulation considers rising or falling release with increased or lowered water level (volume), depending on the objective of reservoir management.

4) Water demand

In the simplest case the monthly withdrawal data from the "reservoir_monthly.csv"-file and the "Share of reservoir filling available for withdrawal directly from the reservoir" from the "reservoir.ctrl"-file are used, the latter being constant all over the year.

In case the Water Management module is applied data from that module are used in the simulation, overwriting water demand data from the "reservoir_monthly.csv"-file.

5) Flood protection

Many reservoirs are multi-purpose dams and also serve for flood protection. Including flood protection in the simulations makes only sense for management options 1 and 2 (as in option 3 discharge is directly linked to reservoir volume, e.g. with increasing volume also discharge is increasing).

If the reservoir volume applying management option 1 is between Dead storage and Active capacity, the reservoir is under normal operation and discharges water according to the set minimum discharge.

If the reservoir volume applying management option 2 is between Dead storage and Active capacity, the reservoir is under normal operation and discharges water according to the calculated value to generate the required electricity.

If the volume reaches the maximum of the Active capacity, water is discharged up to the maximum capacity for flood discharge. Only if the maximum capacity for flood discharge is reached the volume above the Active capacity, up to the Maximum capacity, is used to store water (cut the flood peak). If the volume between Active capacity and Maximum (life) capacity of the reservoir is filled, water is spilled.

10.2 The weather generator IMAGE

The algorithm is divided into four main components: input data preprocessing, parameter estimation for the autoregressive process, time series generation, and postprocessing. A detailed workflow of the IMAGE-PIK algorithm is illustrated in Figure A6. In the following sections, we will describe each of these components in detail, beginning with the input data used for this study.

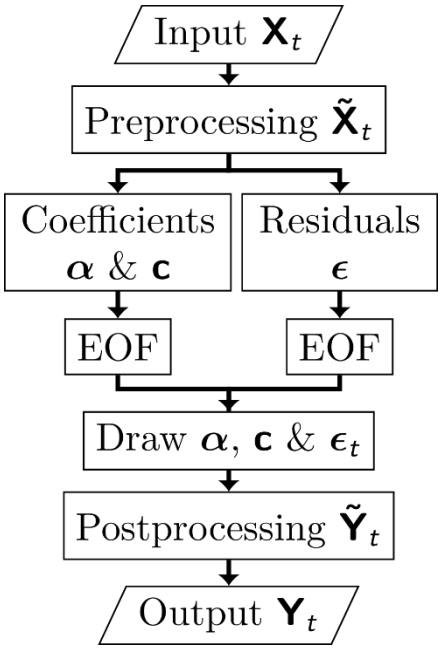

Figure A6: Workflow of the IMAGE-PIK weather generator.

10.2.1 Input Data

The weather generator IMAGE-PIK requires a gridded daily climate dataset to estimate the parameter matrices for the autoregressive process. This dataset can be derived from observations, to analyse historical climate conditions, or from climate model simulations, to assess future conditions under climate change. In this study, we use two distinct datasets: historical observations from E-OBS v27.0e (Cornes et al., 2018) and future projections from the IMPACT2C regional climate model ensemble (Haylock et al., 2008). Both datasets cover the European continent and are provided in netCDF format (www.unidata.ucar.edu/software/netcdf).

E-OBS v27.0e is based on weather station observations interpolated onto a regular geographic grid at a 0.11-degree resolution. It includes daily observations of temperature (minimum, mean, and maximum), precipitation, relative humidity, solar radiation, and sea level pressure. Due to incomplete data coverage in both space and time, an analogue-imputation scheme is applied to fill in missing data. For any grid cell and variable with missing observations on a specific day, neighbouring grid cells and variables with available data are identified to approximate the regional conditions of that day. The day with the most similar conditions, based on the neighbouring grid cells and variables, is then identified, provided that this day has observations for the selected grid cell. If a suitable match is found, the missing data for that specific grid cell and variable is replaced with data from the identified day. If no suitable match is found or predefined similarity criteria are not met, the missing data is replaced using temporal interpolation from surrounding days with non-missing observations. This imputation approach has enabled the completion of grid boxes across most of Europe for the entire time span from 1950 to 2021.

The IMPACT2C dataset consists of an ensemble of regional climate model (RCM) simulations. RCMs simulate the physical climate system for a limited area at high spatial resolution. The IMPACT2C simulations cover the European continent and neighbouring regions. Atmospheric conditions at the lateral boundaries of the domain are provided by global climate model (GCM) simulations. Each RCM-

GCM combination represents a distinct model simulation. Table A2 summarizes the RCMs and driving GCMs used in the IMPACT2C ensemble. Different future socio-economic scenarios are represented by various representative concentration pathways (RCPs). The IMPACT2C ensemble considers three RCP scenarios: RCP2.6 (low concentrations), RCP4.5 (moderate concentrations), and RCP8.5 (high concentrations). Future projections span the period from 2006 to 2100. In addition to future projections, the simulations also include a historical period, under observed greenhouse gas concentrations, covering 1970-2005, which serves as a reference for estimating future changes. Systematic biases present in most climate model simulations were adjusted using a quantile mapping approach (Wilcke et al., 2013; Gobiet et al., 2015).

IMAGE-PIK assumes stable climate conditions within the reference period of the input dataset, meaning it cannot impose any climate change signal on the simulated time series. Therefore, when simulating future climate projections from IMPACT2C, the input time series is divided into three 30-year periods: 2011-2040 (early), 2041-2070 (mid), and 2071-2100 (late). A separate IMAGE-PIK simulation is conducted for each 30-year period, assuming stable climate conditions within each period. This approach captures the climate change signal in the differences between the three periods, while maintaining stable climate conditions within each period.

Table A2: Regional and driving global climate models used in the IMPACT2C ensemble. Each RCM-GCM combination covers different future scenarios.

RCM	GCM	Scenario
KNMI-RACMO22E	EC-EARTH	RCP4.5, RCP8.5
SMHI-RCA4	EC-EARTH	RCP2.6, RCP4.5, RCP8.5
	HadGEM2-ES	RCP4.5, RCP8.5
MPI-CSC-REMO2009	MPI-ESM-LR	RCP2.6, RCP 4.5, RCP 8.5

10.2.2 Preprocessing

IMAGE-PIK simulates any variables as a latent Gaussian variables, meaning that each variable v at every location s follow a Gaussian distribution $\tilde{X}_v(\mathrm{s}) = \mathcal{N}(\mu = 0, \sigma^2 = 1)$. This assumption is crucial for estimating the parameters of the derived autoregressive process. However, many meteorological variables, particularly censored variables such as precipitation and relative humidity, do not inherently meet this Gaussian assumption. Therefore, preprocessing is required to transform these variables into Gaussian distributions. The preprocessing consists of two main steps:

10.2.3 Removing the Seasonal Cycle

Each variable's seasonal cycle is removed. This initial step addresses issues observed in earlier versions of IMAGE-PIK (Sparks et al., 2018), where artificial jumps between consecutive months occurred in the time series. By removing the seasonal cycle, simulations can be conducted on seasonal anomalies. In this study, the average seasonal cycle for calculating these anomalies was estimated using a 5-day sliding average across the entire input period (1950-2021 for observations and 1970-2005, 2011-2040, 2041-2070, and 2071-2100 for the IMPACT2C simulations). The seasonal cycle was treated as multiplicative for precipitation and additive for all other variables.

2.) Normal Quantile Transformation

The seasonal anomalies are then transformed to follow a Gaussian distribution using a normal quantile transformation (Krzysztofowicz, 1997). This introduces a mapping function, $\boldsymbol{Q}_{v,s}$, which maps a given quantile of the empirical distribution of the variable $X_v(s)$ to a Gaussian distribution $\tilde{X}_v(s)$ with mean $\mu = 0$ and standard deviation $\sigma = 1$:

$$\tilde{X}_v(s) \;=\; \boldsymbol{Q}_{v,s}(X_v(s)) \;=\; \mathcal{N}(\mu = 0, \sigma^2 = 1)$$

For censored variables like precipitation and relative humidity, where values are bounded by lower and/or upper thresholds, the second preprocessing step is adjusted slightly. After transformation, all values below or above the threshold (e.g., days with precipitation below 0.0 mm) are mapped to specific values of the Gaussian distribution:

$$\text{Lower threshold } \underline{t}_v(s)\text{: } \boldsymbol{F}^{-1}[0.5 \cdot P(\underline{t}_v(s))]$$

$$\text{Upper threshold } \overline{t}_v(s)\text{: } \boldsymbol{F}^{-1}[0.5 \cdot (1 - P(\overline{t}_v(s))) + P(\overline{t}_v(s))].$$

Here $P(\underline{t}_v(s))$ and $P(\overline{t}_v(s))$ represent the probabilities of the lower and upper thresholds, respectively, and $\boldsymbol{F}^{-1}$ is the invers cumulative distribution function of the normal Gaussian distribution. This ensures that the transformed threshold values are always well below or above the lowest and highest transformed values.

10.2.4 Parameter Estimation

IMAGE-PIK models atmospheric evolution using a first-order autoregressive process. The state of the atmosphere $\tilde{x}_t$ at any given time t is calculated from the previous time step $t - 1$ as follows:

$$\tilde{x}_t = c + \alpha\, \tilde{x}_{t-1} + \varepsilon_t$$

In this equation, α and c represent the deterministic components of the atmospheric evolution, such as large-scale circulation patterns, while ε_t captures smaller, non-deterministic fluctuations. The atmospheric state $\tilde{x}_t$ is assumed to be Gaussian-distributed. For clarity, indices for locations s and variables v are omitted here. A separate autoregressive process is estimated for each month.

The parameters c and α, along with the residuals ε_t, are estimated using an ElasticNet regression (Zou and Hastie, 2005) with a coordinate descent solver (see Wright, 2015) for every variable and location independently. Although the parameters and residuals could theoretically be used to generate a new time series of atmospheric states from an initial condition, further processing is required to produce additional circulation patterns not directly observed.

For generating new residuals, the estimated residuals ε_t for each location and variable are assembled into a matrix $\boldsymbol{E}_{t\times(s,v)}$ for each month, where rows represent different time steps and columns represent various locations and variables combined. This matrix is then decomposed into its principal components time series and empirical orthogonal functions (EOFs) (von Storch and Zwiers, 1999). By decomposing $\boldsymbol{E}_{t\times(s,v)}$ using EOF, spatial and inter-variable correlations are preserved in the EOFs. New residuals can be generated by randomly sampling from the principal component time series and multiplying by the corresponding EOFs, thus maintaining the original statistical properties.

Similarly, the parameters c and α are processed. Instead of estimating these parameters for the entire time series, they are estimated separately for each month and year. These parameters are then organized into a matrix and decomposed into EOFs and principal component time series, following the approach described by Kim and Wu (1999). New parameters can be generated with the same correlation structure as the original parameters using this decomposition method.

The EOFs and principal component time series of both the parameters and the residuals will be used in the subsequent sections to generate new parameters and residuals.

10.2.5 Time Series Generation

As previously described, IMAGE-PIK uses a first-order autoregressive process to generate a new atmospheric state $\tilde{y}_t$ based on the previous state $\tilde{y}_{t-1}$. The parameters and residuals that drive this process are drawn from their respective principal component time series, with different approaches for each due to their representation of different temporal scales in atmospheric processes.

New residuals are drawn at each time step. To do this, new principal components are sampled from the principal component time series and then multiplied by the EOFs of the residuals. The resulting matrix $\boldsymbol{E}_{(s,v)}$ is then decomposed into residuals for each location and variable. In contrast, the parameters α and c are generated in a similar manner but are drawn only once per month, rather than daily. This approach introduces additional persistence into the resulting time series, reflecting the slower temporal changes in atmospheric parameters.

The initial atmospheric state $\tilde{y}_0$ is set to the average conditions for January. Subsequent states are then generated by the autoregressive process using the sampled residuals and parameters. Since the variables produced by this process remain in Gaussian form, a post-processing step is necessary to transform these variables back into their physical units. The details of this post-processing will be discussed in the following section.

10.2.6 Postprocessing

IMAGE-PIK generates time series of latent Gaussian variables that represent the evolution of the atmospheric state $\tilde{y}_t$. By reversing the transformation introduced in Section 2.2 , these states can be converted back into their physical atmospheric counterparts $y_t \equiv y_{t,v}(s)$. Generally, the inverse of the normal quantile transformation is achieved through direct mapping of the empirical quantiles:

$$y_{t,v}(s) = \boldsymbol{Q}_{v,s}^{-1}(\tilde{y}_{t,v}(s)).$$

For censored variables, values that exceed or fall below specified thresholds must be adjusted accordingly:

$$y_{t,v}(s) = \begin{cases} \underline{t}_v(s), \text{if } \tilde{y}_{t,v}(s) \leq \underline{\tilde{t}}_v(s), \\ \bar{t}_v(s), \text{if } \tilde{y}_{t,v}(s) \geq \bar{\tilde{t}}_v(s), \text{cccc} \\ \boldsymbol{Q}_{v,s}^{-1}\left(\tilde{y}_{t,v}(s)\right), \text{else.} \end{cases}$$

This ensures that the probability of under- or overshooting a threshold in the simulated time series matches that of the input dataset.

However, the special treatment of censored variables can distort correlations and introduce biases. To correct these issues, an additional bias adjustment is applied to the IMAGE-PIK simulations. Specifically, a trend-preserving parametric quantile mapping approach (Lange, 2019) is used to adjust the simulations, aligning them more closely with the input dataset and preserving the original trends.

10.2.7 Validation with E-OBS driven simulations

For an initial evaluation of IMAGE-PIK, we conducted simulations using the E-OBS v27.0e observational dataset as input. E-OBS provides daily gridded observations of temperature (minimum, maximum, and mean), precipitation, relative humidity, shortwave radiation, and sea level pressure from 1950 to 2021, with a spatial resolution of approximately 12.5 km covering the entire European continent. We used IMAGE-PIK to generate a synthetic time series of 1,000 years, using 1950 to 2021 as the input period. Before the simulation, we performed spatio-temporal analogue imputation to fill in missing

values in E-OBS. However, due to the high number of missing values, the northern part of the Scandinavian Peninsula and the southern parts of Greece and Italy were excluded from the simulation. As described earlier, we applied a bias adjustment after generating the time series, using the fulltime span of E-OBS as the reference.

Figure A7 shows the seasonal mean temperature from E-OBS (1950-2021) alongside the bias of both the raw and bias-adjusted IMAGE-PIK simulations (period 0001-1000). As temperature is a non-censored variable, the bias in the raw generated time series is already quite low. Across all regions and seasons, the bias ranges between -0.5 and 0.5 K, indicating that the bias adjustment provided no significant improvement. A slightly higher temperature bias is observed after bias adjustment during the winter season, likely due to natural variability in the E-OBS dataset and the generated time series. Nonetheless, this bias remains within an acceptable range.

For precipitation, however, the special treatment of censored variables resulted in a more pronounced bias, as illustrated in Figure A8. The strongest bias appears in southern Europe during the second half of the year. The raw IMAGE-PIK simulations exhibit a consistent dry bias across Europe, ranging from -0.2 to -0.8 mm/day. The bias adjustment significantly reduced this bias for all seasons except autumn, where a small residual dry bias of around -0.2 mm/day remains over the Alpine regions in the bias-adjusted IMAGE-PIK simulations.

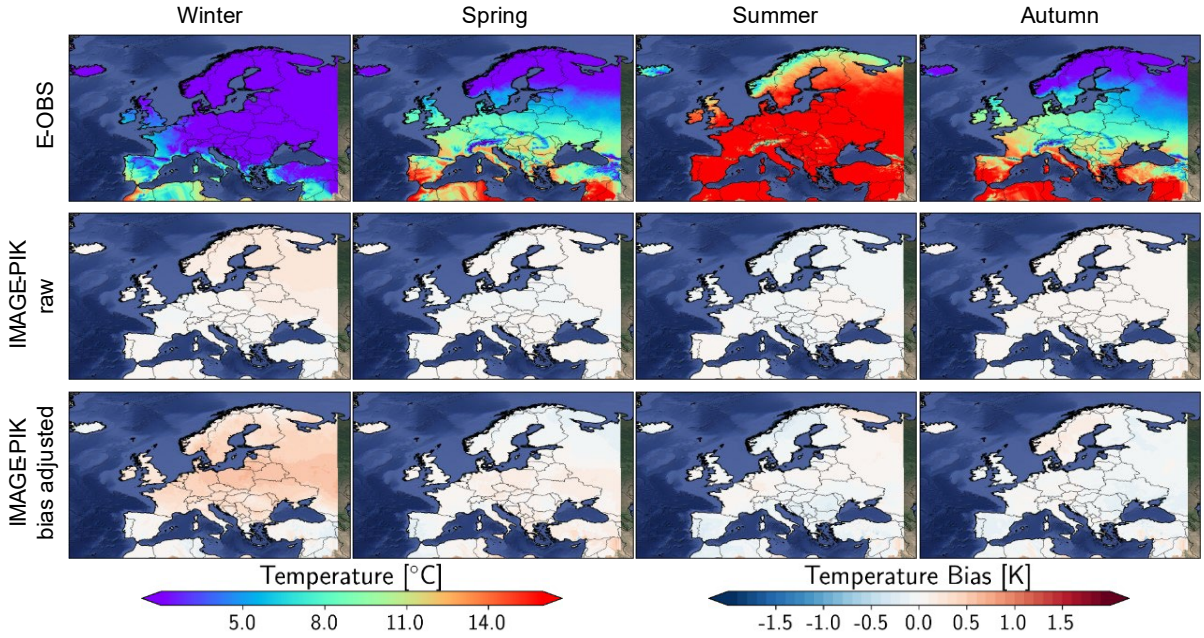

Figure A7: Seasonal average temperature from E-OBS observations (1951-2021) in comparison with the raw and bias-adjusted IMAGE-PIK simulations based on E-OBS (1000-year simulations based on 1951-2021 E-OBS). E-OBS data is shown as absolute temperatures for each season (northern hemisphere winter, spring, summer, and autumn), while the IMAGE-PIK simulations are shown as differences/bias compared to E-OBS.

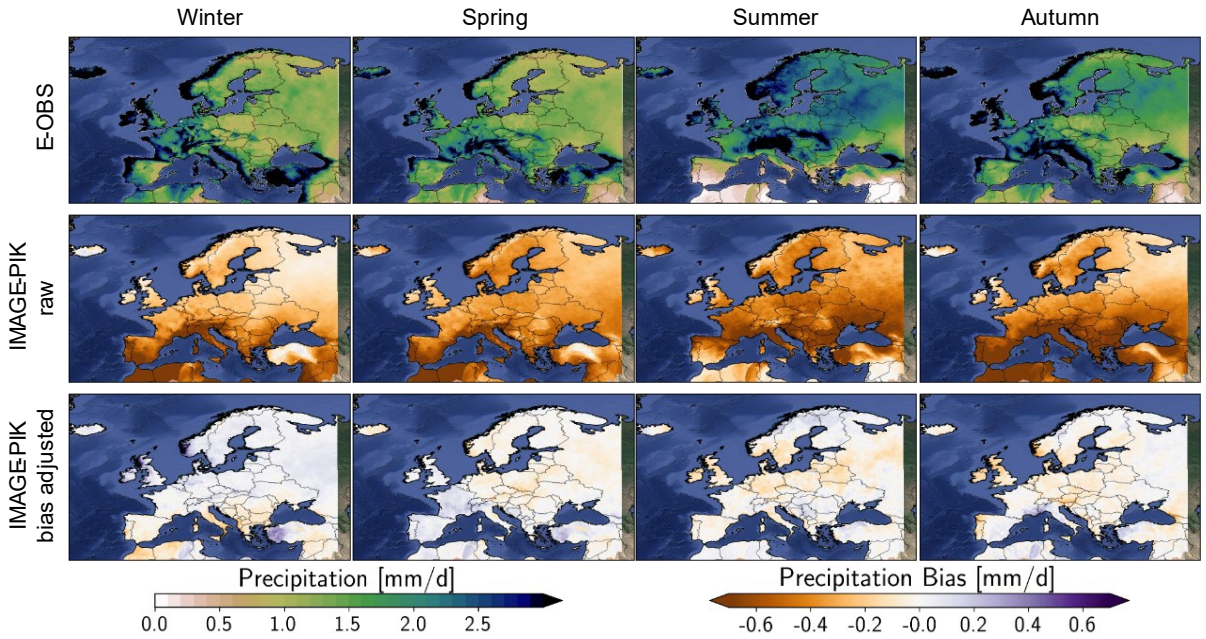

Figure A8: Same as Figure 26 for precipitation.